Data and Methods for the Design of Accelerator Based Transmutation Systems

F. Atchison
Paul Scherrer Institute
CH-5232 Villigen PSI
Switzerland

Abstract

From a calculational standpoint, at least, accelerator based transmutation systems for nuclide burning are tailored versions of a general class of facility that can be used as spallation neutron sources, for nuclear breeding, etc. The nuclear design can be considered in two parts: (i) the conceptual design for (in this case) the target/burning system and (ii) the full characterisation of the operational parameters for the complete system. Roughly, part (i) decides the nuclear physics of the burning facility while part (ii) produces the numbers required to make an engineering design.

The main part of the paper will concentrate on methods for the full characterisation of the system by giving a description of the calculations made for SINQ, the PSI spallation neutron source project: the methods are less dependent on the specific application of the transmutation system but the applicability of the work to a nuclide burning facility is discussed.

The data and calculational methods for the conceptual design have to allow detailed study of the nuclide production by a wide range of particle types and energies interacting with a variety of target nuclides. A short discussion of calculational possibilities is given.

Contents

1 Introduction

From a modelling standpoint at least, an accelerator based transmutation system for nuclide burning is a specific application of systems which have been built or proposed for use as:-

. Neutron Sources (Note: the unreferenced sources are described in the proceeding of the ICANS meetings [1 to 9]

- **pulsed (KENS, IPNS,(WNR), LANSE, ISIS, SNQ [10])**
- **continuous (ING [11], TNF, SINQ**
- **for damage studies (RTNS [12], FMIT [13], JRC/ISPRA [14])**

• Breeding - Furukawa [15], Takahashi [16]

They consist of an accelerator with beam handling system plus a plant complex which can be split into:

the Target	**the block of material struck by the accelerated beam**
the 'next' Layer(s) -	**which 'customerizes' the facility to do the job in hand**
the Shield	**the section of the facility that handles unused particles**

The nuclear design consists of two (overlapping) parts:

(1) The conceptual design for the target and 'next' layers: this covers the choice of the type and energy of the particles and the geometry and materials arrangement that best do the job in hand. This will lead to the choice of type and energy for the accelerated particles,.

(2) the full characterisation of the operational parameters of the system: power densities, radiation damage, activation, prompt radiation doses etc.

The aim of this paper is to discuss the tools required to carry out such a job for a nuclide burning facility. This may be trivially stated as the need to be able to calculate most aspects of the interaction of all particles which "may be produced with all materials used in the system. The selection of calculational methods has to be based on (i) what is to be calculated (ii) how accurate the results have to be and (iii) what calculational methods are available.

In the first part of this report a description of the calculations carried out for the SIN Q project will be given on the premise that, a large part of the nuclear design for a nuclide burning facility will be aimed at solving similar problems, hence calculational methods may be discussed in relationship to specific tasks which are

part of a similarly large single project.

The second part of the paper will look at the problem of calculational methods for nuclide burning specifically. Comments on the relevance of the SINQ results to a nuclide burning facility will be given at the beginning of this second part of the report.

Part I

Calculations for SINQ

2 A Brief Description of the Project

The SINQ project has as design goal the production of the highest possible thermal and cold neutron fluxes for neutron scattering experiments, from the proton beam left over after use for nuclear particle production. The system is to be designed to handle up to 1.5 mA of 590 MeV protons (about 0.9 MW).

The PSI accelerator complex (Fig. 1) is a multidiscipline, multiuser system based around two 72 MeV injector-cyclotrons and a 590 MeV ring cyclotron. This is in the process of being upgraded to produce D.C. beam currents in excess of 1 mA and is operating presently at about 500 μA. The 590 MeV beam is used for meson and muon physics at targets M and E. Other facilities (muon beams for solid state physics, bio-medical applications, radiation damage facilities, isotope production, etc) are also supported.

The source is being built on an extension of the proton channel beyond Target-E into the *Neutronenhalle*. The building will house the source itself and the experimental area for neutron scattering instruments mounted at beam-tubes.

The non-interacting part of the proton beam is collected beyond target-E, deflected downwards to pass under the hall foundations and finally pitched vertically upwards to the spallation target. A vertical section is shown in Fig. 2.

A diagram of the layout of the complete SINQ facility is shown in Fig. 3 and details of the source in Fig. 4 and 5.

Evaporation (fast) neutrons are produced at the rate of about 10/proton by high-energy interactions in the target. About 70% of the beam power is deposited in the first 30 cm. The target is located in the middle of a 2 m diameter and height tank of D_2O to thermalise the neutrons. The thermal neutrons are extracted with beam-tubes: neutrons entering through the window drift along the tube to a monochromator system and hence to the scattering instruments.

Particular emphasis is being placed on the provision of cold neutrons. A container with 20 litres of liquid deuterium will further moderate the thermal neutrons (from an approximately Maxwellian spectrum with characteristic wavelength about 1 $\AA$ to one with about 5 $\AA$). The cold neutrons will be ext ratted via a beam-tube and a neutron guide system. The guide system provides a multi-user facility and will be mounted in a separate experimental hall (*Leiterhalle see* Fig. 3).

The neutron production spectrum extends into the high energy region. The moderator tank is followed by a roughly 5 m thick iron and concrete shield and the monochromators and first section of the guide system also require a thick shield to handle high-energy neutrons.

The project was funded in 1987 and construction of the buildings (which also included the proton channel tunnel and source foundation) was completed at the end of 1991. The safety report was completed in December 1991 and construction work on the source itself is planned to begin in Autumn 1992.

3 Calculational Tools

The part of the SINQ system that requires consideration in the neutronics calculations consists of about 3'500 m^3 of material. The basic information required comes from (i) detailed calculations of the innermost 30 to 50 m^3 (this is a region centred about the target and extending about 1 m into the shield) - neutronic performance, heating rates, activation etc (ii) study of the shielding (which makes up most of the rest of the material) - external dose-rates, induced activation etc and (iii) the consequence of activation carried outside the source-block - shielding requirements for the target transport flask, shielding for plant handling activated coolants (gases and water), etc.

The calculations are made using the HETC package [17] as the basic tool: this is illustrated in Fig. 6. It consists of the nucleon-meson transport code HETC, the neutron transport code O5R_PSI and several analysis codes. The centrepiece is the HETC code itself; this is described in section 4 and a brief critique given in section 5.

Neutronic calculations below 20 MeV are carried out using 05 R_PSI, a locally produced version of the 05R code [18]. This is a a continuous-energy cross-section based Monte-Carlo code. O5R_PSI uses data from ENDF/B-IV [19] and a suite of routines for resonance unfolding, doppler broadening and making other manipulations of the cross-section data have been collected (or developed). The code is used also for thermal neutron transport and presently employs a 'perfect-gas' scattering model. 05 R_PSI also includes a more complete description of fission (not required for SINQ).

Both HETC and O5R_PSI produce nuclear physics histories for large multi-media systems. This is a file containing the position, type and parameters for the

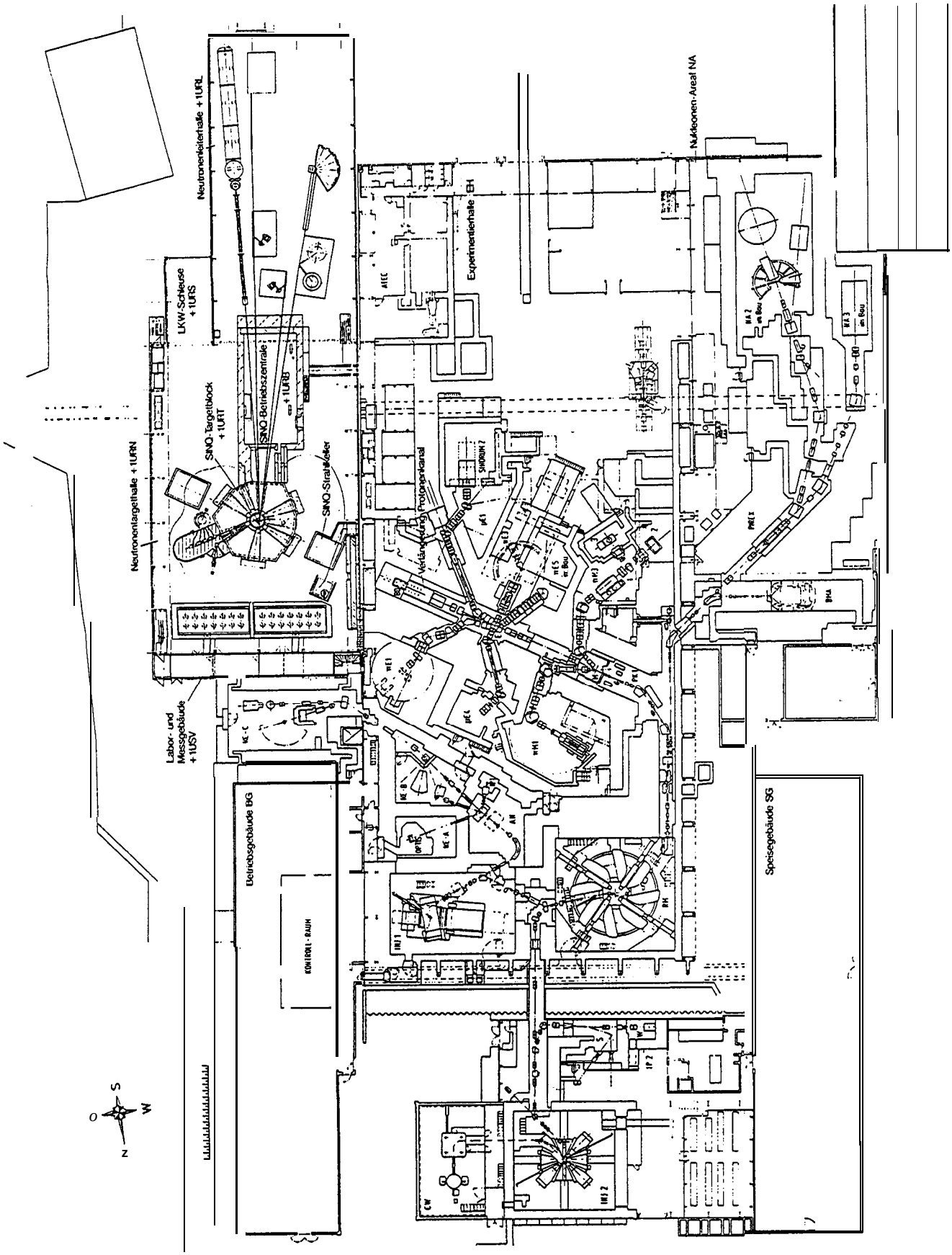

Figure 1: Layout of the PSI accelerator facility

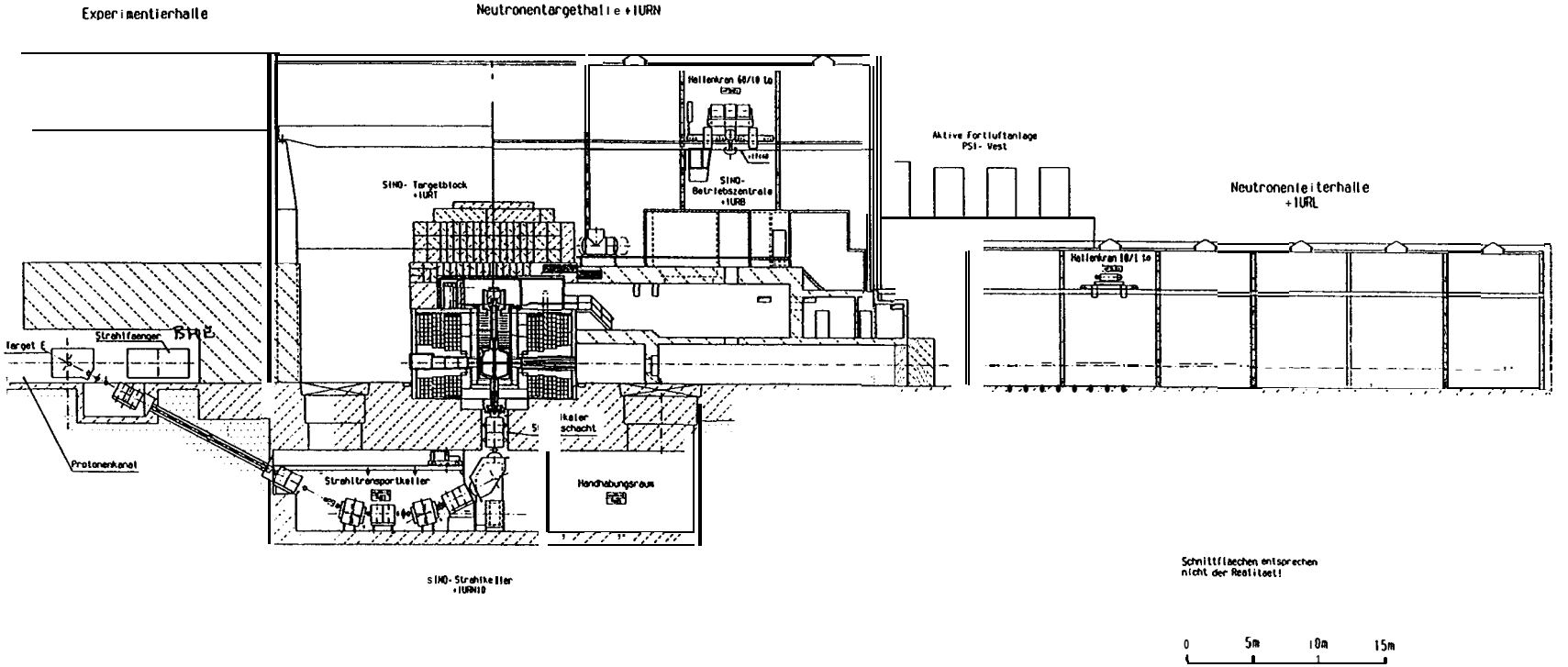

Figure 2: A vertical section along the axis of the proton beam for SINQ.

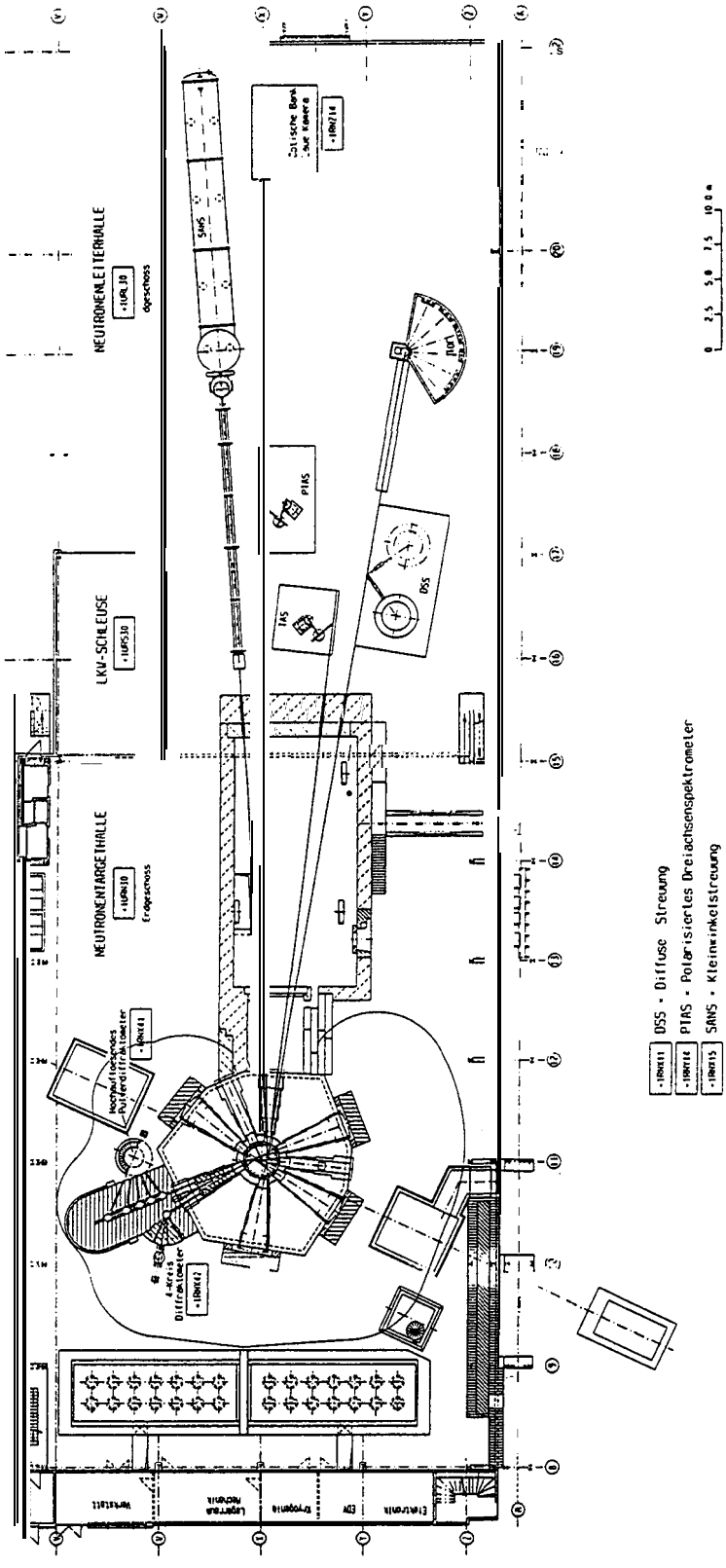

Figure 3: A layout of the complete SINQ neutron scattering facility

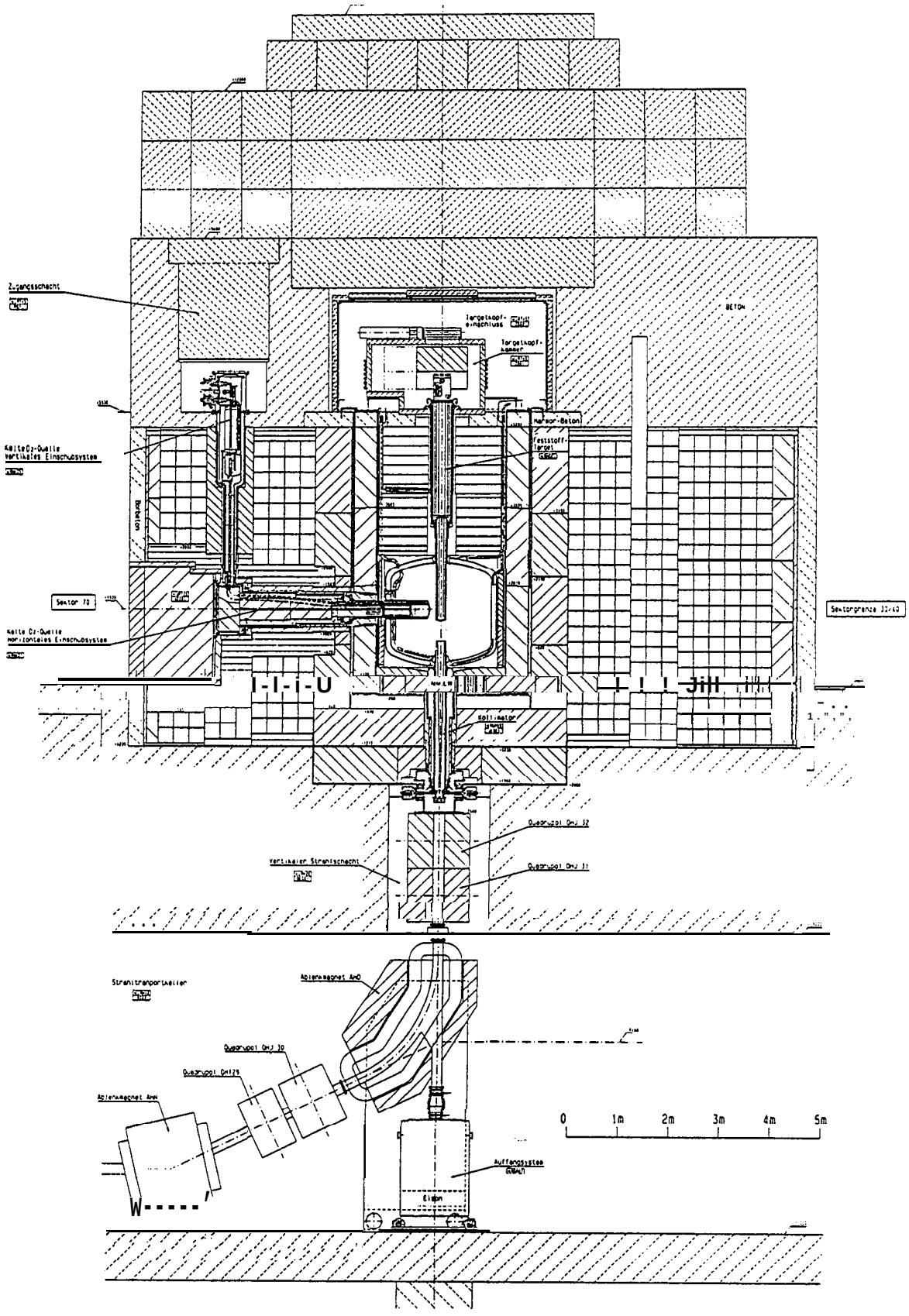

Figure 4: A vertical section through the centre of the SINQ source block

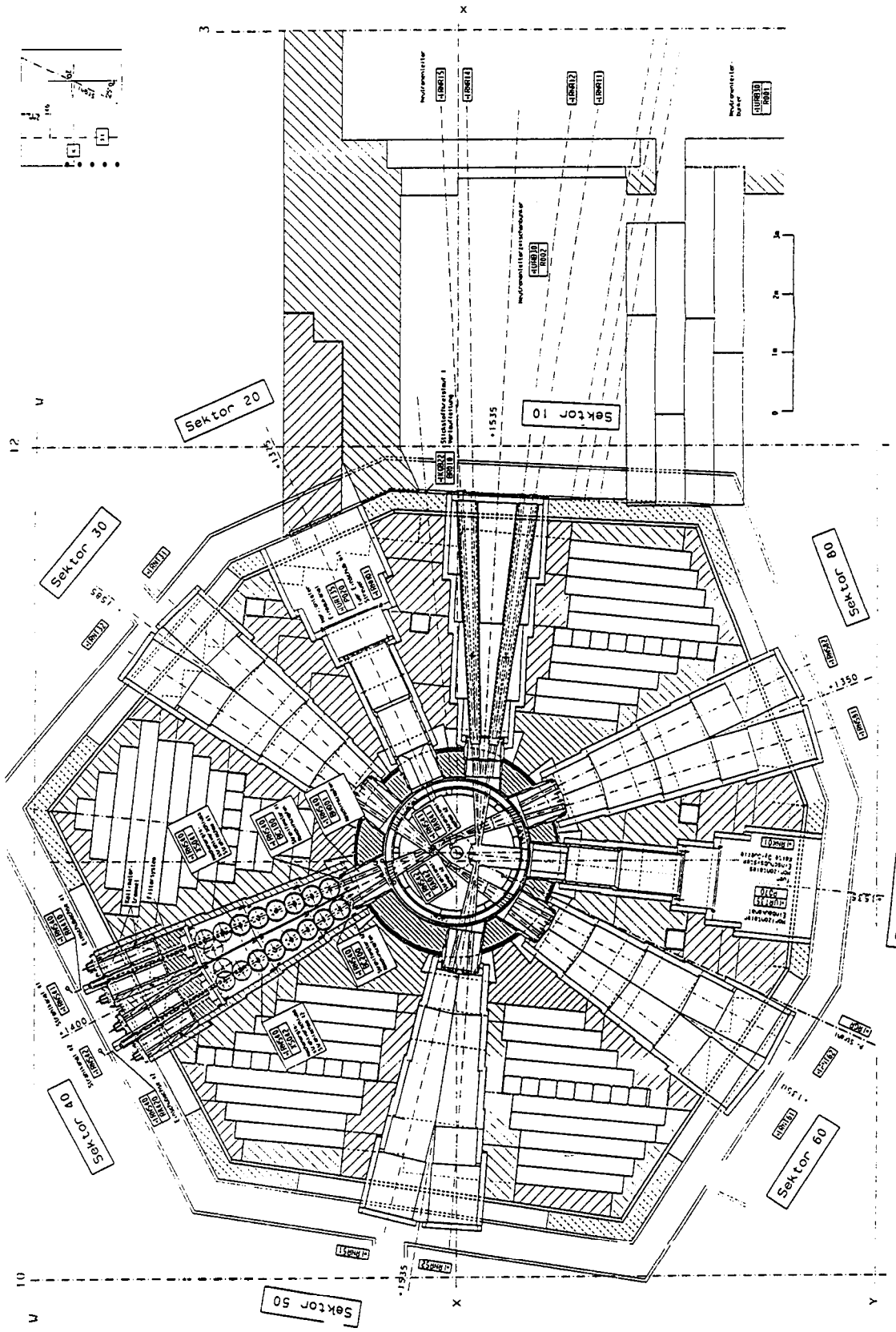

Figure 5: A horizontal section through the SINQ source block. Note: The beam-tubes are on two levels (1350 mm and 1535 mm).

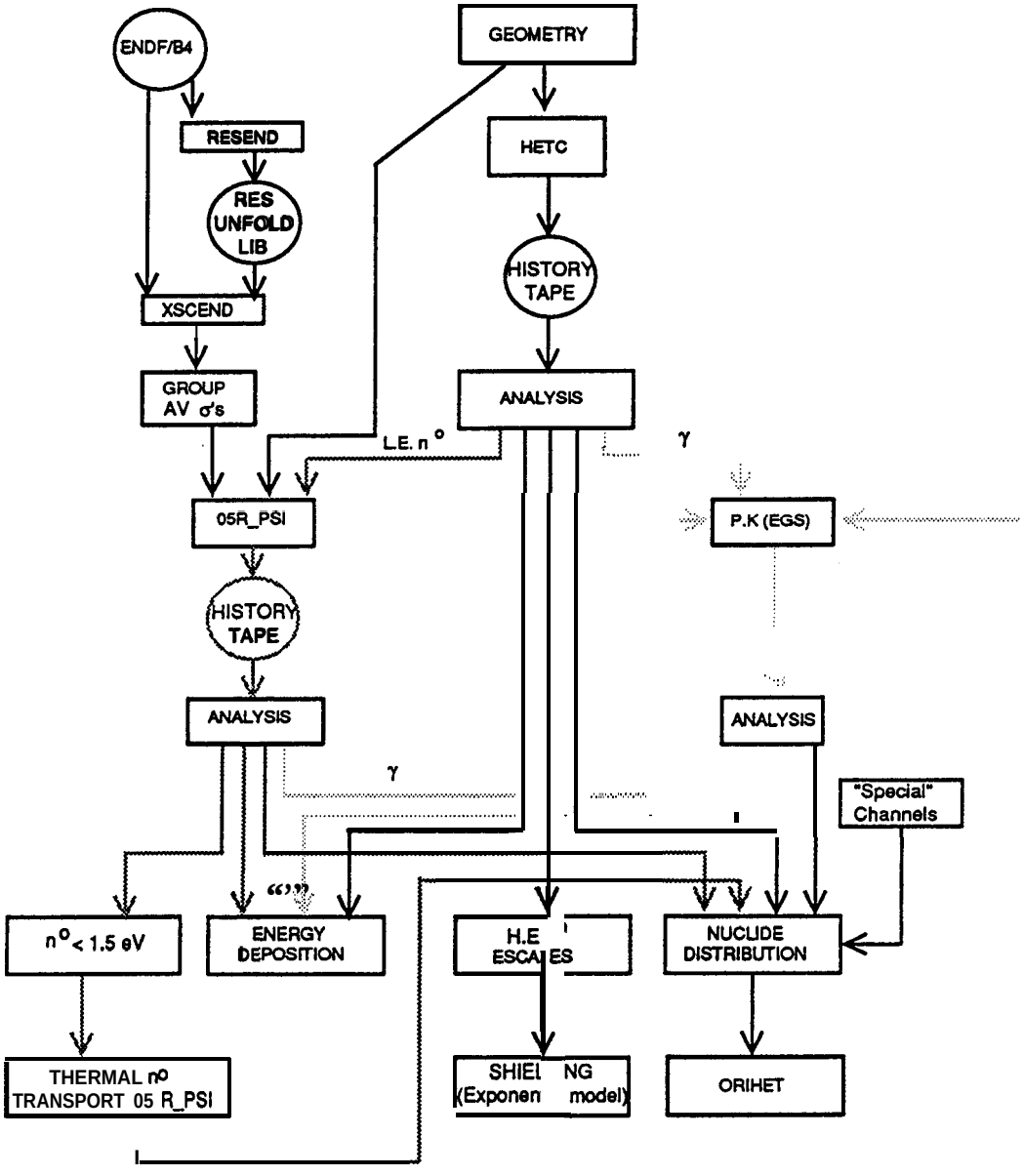

Figure 6: The code package used for SINQ calculations.

interactions induced by the primary particles through all generations of product particles in the valid transport range (type and energy). They are equipped with a geometry routine (GENJOM - the Oak Ridge General Geometry Package developed for 05R [18] in the PSI version) which allows description of multimedia systems having media separated by 3-D geometric surfaces describable via second degree equations in the coordinates.

The history files require analysis to yield specific answers (or contributions) to a variety of processes and to provide source terms for further calculations. The main analysis codes used are ORIHET and ENDEN: several special analysis routines had to be written to look at specific problems.

ORIHET is an adaptation of the ORIGEN code [20] to solve the Bateman equation for nuclide production rates from both HETC and O5 R_PSI. The fixed data has been extended to cover all nuclides up to mass 245 in the 7^{th} Edition of "Table of Nuclides" [21] and gamma information comes from the Daamstadt library [22]. Special versions to treat burnup and corrosion have been created.

ENDEN analyses the history tapes for estimation of the contributions from both HETC and 05R to energy density distributions. It is the task that requires the most complete analysis of the history tape as most 'events' make contributions and through mutliple aspects. Also some re-analysis is required: e.g. ionisation loss (this is the main contributor to heating of the target) requires apportionment of the slowing-down contributions through the bin 'geometry'. Energy deposition analysis may be extended in a simple manner to estimate displacement damage.

The contribution of gamma-rays to energy deposition has mainly been made using explicit (point kernal integration) methods. The electromagnetic shower code EGS [23] has been used for specific aspects of the gamma transport calculations.

Quite a few problems have been solved by special approximations - the contribution of gammas to heating rates, shielding performance, activation at the peripheries of the system, etc. The methods used will be included in the appropriate sections.

4 HETC Program - A brief review

The HETC code combines models so that the majority of the nuclear physics from the passage through bulk matter of nucleons of energy greater than 15 MeV and charged Pions (above 2.2 MeV) is treated. The calculational scheme is illustrated in Fig. 7. HETC is an analogue Monte-Carlo code which generates particle cascades. These cascades are analysed (usually with off-line codes) to obtain results of practical interest (e.g. energy deposition). The cascades are also analysed to produce source terms for separate treatment of aspects not handled directly (fast neutron transport, gamma-transport, activation build-up etc). The heart of the code is a theoretical treatment of particle-nucleus interactions based on the Serber model [24], in which the overall particle-nucleus interaction is broken up into two steps:

The first step is an intra-nuclear cascade of individual particle-nucleon interactions governed by the normal high-energy physics kinematic and conservation laws and with free-nucleon cross-sections. The 'nucleus' enters the picture via being a spatially localised region of very high nucleon density, the struck nucleons are in a dynamic equilibrium inside a potential well (Fermi momentum) and the dynamic equilibrium is a ground state requiring restriction of the kinematic phase-space to allow satisfaction of the exclusion principle. HETC uses the Bertini code [25] to calculate this part which also includes the Isobar Model [26, 27] for treatment of Pion production. The lower energy limit of the model is indistinct but somewhat below 50 MeV (traditionally 15 MeV is selected for neutrons as being somewhat below the upper energy limit of neutron cross-section data sets, thereby easing the transition to fast neutron transport codes): as the energy of the incident particle is reduced, collective interactions with the nucleus as a whole become significant, eventually dominating and leading to the compound-nucleus region.

The second stage describes the de-excitation of the final nucleus left after the intra-nuclear cascade. This is treated with the Statistical model [28] as incorporated into the code of Dresner [29]. The Dresner code has been modified to allow treatment of fission [30].

The Bertini and Dresner codes, together with code to treat (i) particle-nucleon interactions, (ii) ionisation loss, (iii) particle-nucleus elastic-scattering (based on user-supplied cross-section data), (iv) the geometry of the system and (v) particle book-keeping, was initially put together by Coleman and Armstrong [31] to form the NMTC code allowing treatment of nucleons up to 3.5 GeV and Pions to 2.5 GeV. Improved versions of both the Bertini and Dresner codes together with a treatment for very-high (200 GeV) incident energy particles and multiple coulomb scattering resulted in the HETC..code [32].

Some results used for comparison purposes were made using the earlier NMTC version: in the 600 MeV energy region, the differences between the NMTC and HETC codes is not large.

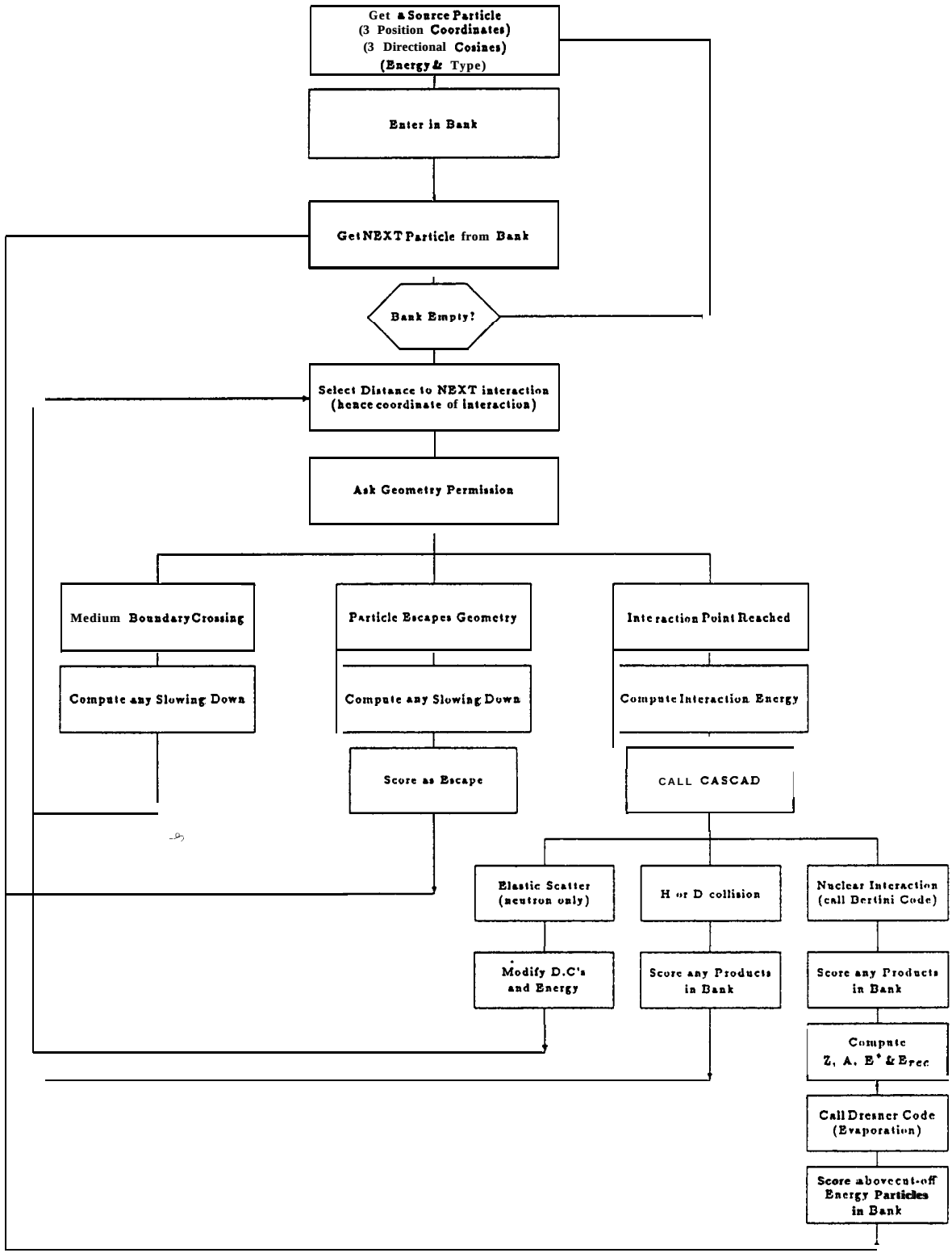

Figure 7: The main parts of the HETC calculation scheme.

5 Assessment of HETC Performance

The accuracy of the HETC code is extremely difficult to quantify. The code gives the basic information which allow estimations for a wide range of radiation effects caused by the passage of particles through bulk matter (secondary particle fields, residual nucleus distributions, energy deposition, gamma source terms, fast-neutron source terms, etc). It is an analogue Monte-Carlo code so errors come both from statistics and also from propagation of theoretical model inadequacies. Statistical errors may be controlled by standard methods and can usually be reduced to levels well within the intrinsic accuracy of the models.

Fullwood et al. [33] concluded that the 'global' accuracy (that is over a large fraction of all results capable of being produced!) was about 20%. Specific results can have very much larger (or smaller) errors.

In the target, ionisation loss accounts for about 80% of the energy deposition. The Bethe-Bloch equation, which is used by HETC to calculate $\frac{dE}{dX}$ values, is accurate at the percent level. Coulomb scattering (which will have some affect on energy density) is treated using the Fermi joint distribution function. Quite good agreement with the results by Barkas and von Friesen [34] for coulomb scattering of 750 MeV protons by copper has been obtained.

An important quantity (with influence on energy density and shielding estimates) is the double-differential spectrum for the high-energy neutrons (intensity versus energy and angle). Experiment and HETC prediction are generally in disagreement at small production angles [35, 36, 37, 38, 39], with HETC values lower by factors of 3 to 5 or more, although recent measurements at Los Alamos [40] for 256 MeV protons and [41] show generally better agreement over a wide range of angles. It should be noted that neutron spectrum measurements at high energies are difficult.

The evidence indicates that the HETC programme is failing to calculate correctly the details of the double-differential cross-section: the total inelastic cross-section and the gross apportionment of the energy in the particle nucleus interactions seem to be within the 20% global error. The consequence of this is only relevant for specific SINQ calculations and is considered in the appropriate section.

In the particle-nucleus interaction, the energy of the incident particle is distributed between:

- outgoing high-energy particles,
- evaporated nucleon clusters,
- . binding energy,
- . nuclear gamma rays,
- . recoil of the struck nucleus.

A major fault in this energy distribution would show up in predictions of energy-deposition, nu elide production, thermal-fluxes, etc. In general such predictions are in good agreement but it should be noted that the HETC results are normally only part of the calculational story and so its actual relevance is not easy to assess (e.g. error compensation):-

. Neutronic performance, power levels, induced activation and shield operation for the neutron sources ISIS [42, 43, 44, 45] and LANSCE [46]. To date, agreement of prediction and observation is good (maybe at the 10% level) but these are both very complicated systems with many possibilities for error compensation and the agreement should be treated with caution.

. Theoretical predictions [47] of the expected results from an experiment to measure heating rates close to the target of a spallation neutron source [48] are not good: the calculation did not include all contributions, hence this difference is not yet evidence of a fundamental disagreement.

. Fast neutron production by high-energy particles [37, 38, 39, 40, 49, 50] and the neutronic performance of ISIS and LANSCE. In terms of the workings of HETC these give a strong indication that the residual excitation after the intra-nuclear cascade and the evaporation parameters yield the right number of neutrons.
Work in progress on fission models has used the evaporation code of HETC in conjunction with the compound nucleus model to obtain good agreement with fission and (n,xn) cross-sections for high-Z nuclei, giving a direct check on the evaporation part for this Z region (see part-II, section 11.3).

- Nuclide production: this should be a rather sensitive test of the whole intra-nuclear cascade and evaporation model. The majority of experiments are in the high-Z region where the fission process also plays a considerable role: comparatively recent (and reasonably direct) comparison of HETC and experiment may be found in, for example, references 16, 51 & 52.

- Shielding performance: ISIS (see above), LANCE (see above) and references 53 and 54.

- Dose equivalents for neutrons in the energy range 60 to 3000 MeV and for protons from 400 to 3000 MeV come from NMTC calculations [55].

6 Conceptual Design and Aspects of Optimisation

In terms of the first part of the calculations as generalised in the introduction, the choice of type and energy of the accelerated particles is given (as also is that SINQ will be a continuous source). The particles to be used are fast (evaporation) neutrons from the interaction of the primary protons and high-energy cascade products. The 'next' layer is a tank of D_2O equipped with an array of beam-tubes. The design aim is to produce the highest intensity of thermal and cold neutrons at the experiments which are located outside the limits of the biological shield (see Fig. 3). This comes down to fixing

- the material and dimensions of the target
- the diameter and height of the moderator tank
- the position and dimensions of the beam tubes.

7 Neutronics Generalities

The major problem specific to the design of continuous neutron sources is neutron economy: heat removal is a common problem for all such facilities. Neutrons are produced with energy in the MeV region and slowed down in a moderating material to provide the (useful) thermal neutrons. Associated with the production is energy deposition (about 40 MeV in the target per fast neutron). To obtain high intensity, the neutron production should be concentrated in as small a volume as tolerable: in the direction of the incident beam this is governed by the interaction cross-section (plus $\frac{dE}{dX}$); in the transverse direction the target size, and hence beam size, should be kept as small as possible (see Fig. 8). This means that power density (and hence the associated radiation damage, specific activation, etc) should be as high as practicable.

As many of the fast neutrons as possible need to be brought to thermal energies in accessible regions of the moderator. All the neutrons will be lost eventually; at best through the outer wall of the moderator, as in this way the long random-walk involved leads to the highest density of neutrons in the moderator (and hence neutrons available to the users). The major cause for concern is loss of neutrons in the target region, either in the slowing-down process or as thermals, by absorption: such neutrons will make only short random walks and hence give reduced contribution to the useful neutron intensity. Absorption in the region of the target cannot be avoided but can be kept to a minimum by the careful choice of materials. This can conflict with engineering requirements.

A further important consideration is to maximise the fast-neutron production in the target. The number of neutrons produced per interaction increases with the mass of the struck nucleus. Interactions with lighter-mass 'materials of construction' which encroach into the 'target region' degrade performance because of their inferior neutron production.

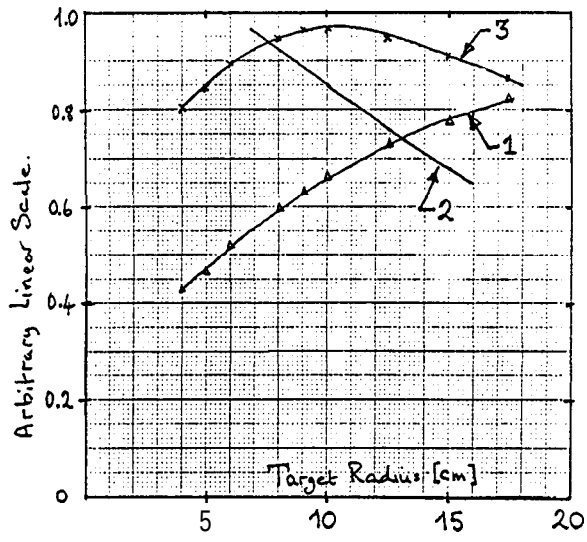

Figure 8: **Normalised curves giving representative data for the choice of target radius:**
Line 1: fast neutrons per proton as a function of target radius.
Line 2: neutron flux at the maximum as a function of target radius for fixed fast neutron production, as calculated using diffusion theory by B. Sigg [56].
Line 3: The resulting variation of flux with target radius.

The neutronic considerations of SINQ are pursued further in section 12 in the Appendix.

8 System Performance Estimates

The major considerations are of power deposition, activation and shield performance. These will be considered in the following subsections with more details of calculations and results in section 15 of the Appendix.

8.1 Power Deposition (with Radiation Damage)

Power deposition estimates are the most important results required for the engineering design. The case of the target has been discussed above and the other important aspect is to establish how much of the system requires forced cooling and at what level. The calculations are straightforward (although long and lead to the generation of lots of numbers): they require systematically following the full nuclear cascade.

The principal contributions are as follows:-

. High Energy Transport

1. Charged particle tracks between interactions via $\frac{dE}{dX}$.
2. $\frac{dE}{dX}$ for muons resulting from pion decay.
3. Recoil kinetic energy of light ion (charged evaporation products) and residual nuclei (including fission products) from inelastic reactions.
4. Decay energy from the residual nuclei (via solution of the **Bateman** equation for the system) followed by electromagnetic cascade calculation of the gammas (and possibly betas).
5. Prompt nuclear gamma rays (residual nuclear excitation) and π^o decay gammas as source terms for gamma transport. Note: the π^o has a lifetime of 8.28.10-17 seconds and decays into 2 high-energy (about 70 MeV) gamma rays.
6. Fast (evaporation) neutrons from interactions as source terms for further transport.

- Fast Neutron Transport (Source term from **high**-energy transport)

1. Recoil kinetic energy of light ions produced as inelastic scattering products (also, where appropriate, fission products).
2. Nuclear recoil kinetic energy from elastic and non-elastic scattering.
3. Gammas from capture (and non-elastic scatters) - implies the need for thermal neutron transport.
4. Decay particles from activation products.

- Gamma transport with source terms from **high**-energy and fast-to-thermal neutron transport and decay power.

Radiation damage is intimately linked with energy deposition. Both damage energy and displacement **cross**-section estimates [57,58] are based on calculation of the fraction of ion recoil-energy transferred to the material lattice (for example by the Lindhard [59] efficiency factor). The required information on charged particle energy loss and ion recoil energies (residual nuclei and evaporation fragments) is available from the HETC and **O5R_PSI** history files. The rates for the other main aspects of radiation damage (gas production and transmutation products) also come from analysis of the history tapes for stopped protons, evaporation ions and residual nuclei.

The calculated results of energy deposition through SINQ (with the old **Pb-Bi** target) are summarised in Fig. 9 which gives a plot of the power density along a radial line outwards from the target through the inner region of **SINQ**.

8.2 Shielding Estimates

The calculations have to demonstrate that the bulk shield design **fulfils** the three major functions:

(i) to reduce the dose rates at normally accessible positions to below 2.0 μ Sv/h.

(ii) to reduce particle fluxes irradiating the ground outside the limits of SINQ such that activation is below 1 **Bq/g.**

(iii) to limit the dose rate from induced activation in caverns to be accessed a short time after beam switch-off to less than 1 **mSv/h.**

The essential task is to estimate particle fields at relevant locations in and around a very large **inhomogeneous** structure and then to fold these particle fields with suitable response functions to estimate dose rates and/or induced activation levels.

The calculations are based on the exponential shielding model mainly used in the 'straight-ahead' point **kernal** mode and, where appropriate, with smearing. It has been linked with the 3-dimensional geometry package of HETC, which is capable of representing quite detailed models of the shield.

In the case of **SINQ,** the thickness of the shield reduces the thermal neutron flux to users at the beam-tubes and the aim is to produce as thin a shield as possible.

The point-kernel method, with varying degrees of approximation, has been in use for shield design at **high**-energy physics laboratories for many years and reproduces the essential physical processes.

The major advantage of the method is that it is **calculationally** transparent: the effect of parameter errors are straightforward to see and at the design stage defects may be identified for correction.

'Discrete ordinates'-style calculations of highly idealised models for the shielding have been made [60, 61] and results from these calculations incorporated into the conceptual design. These results are also used for model parameter selection and to obtain estimators for other quantities of interest.

8.2.1 The Exponential Shielding Model

The dose rates outside the bulk-shield are generated by high-energy neutrons produced in inelastic primary proton interactions in the target. For deep penetration (greater than about 5 shielding lengths), the dose rate caused by high-energy neutrons external to a shield may be calculated using the rather straightforward **formula:-**

$$D(6) = \Omega \int dE \left\{ \Phi(E,\theta) \,.\, \mathcal{F}(E) \,.\, B(E) \,.\, \exp^{-\sum_i \frac{s_i}{\lambda_i}} \right\}$$

where D(6) is the dose at some angular position subtending a solid angle Ω to the source, $\Phi(E,\theta)$ is the

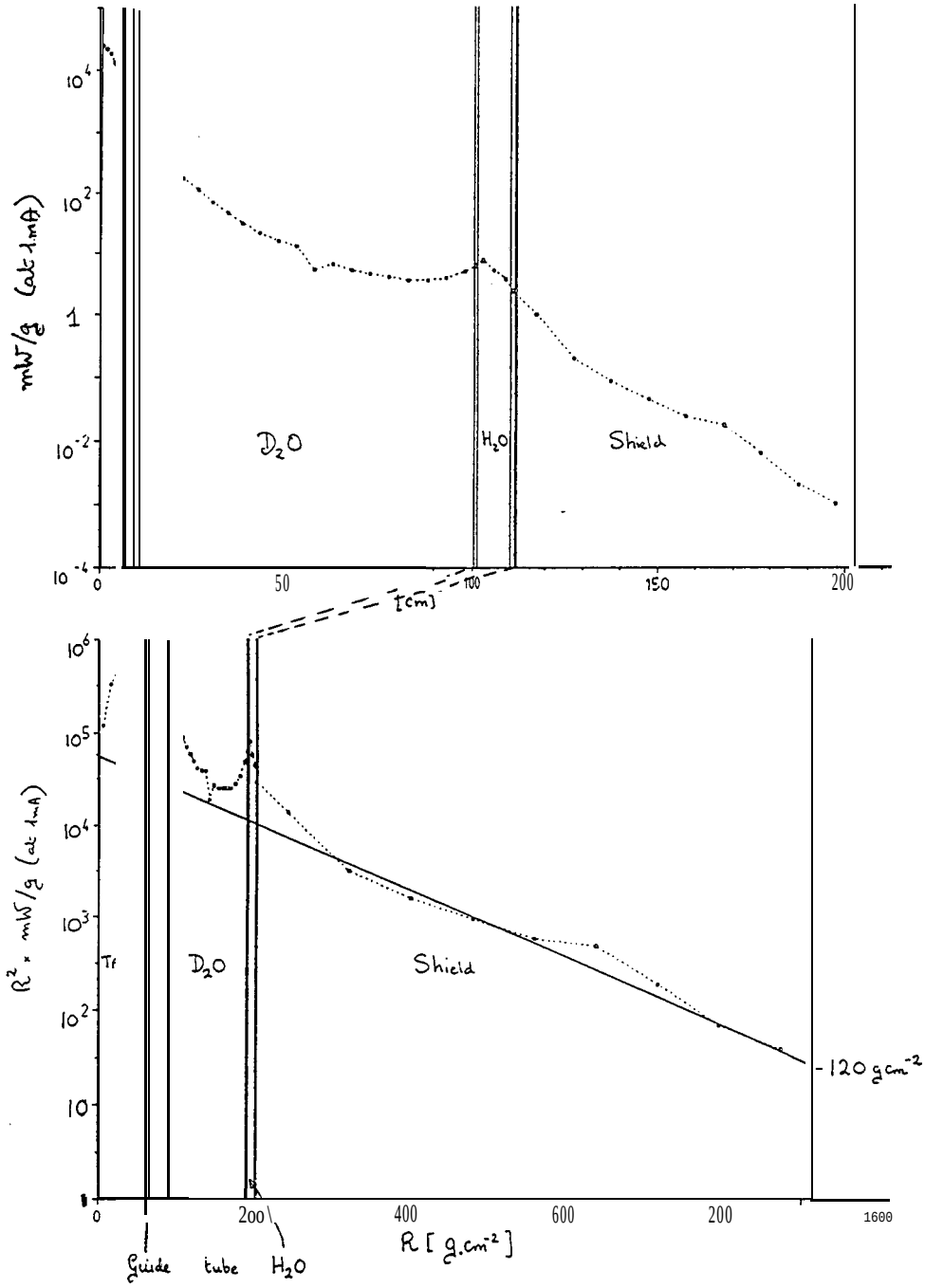

Figure 9: Distribution **of Power Densities in the inner region of SINQ.**
(a) **A plot of Log_{10} power density in mW/g at 1 mA proton current as a function of radial distance from the target and for a height about 10 cm above the level of the beam window.**
(b) The same information as in (a) but displayed as Log_{10} power density times solid angle vs radial distance in g/cm^2 (the solid angle factor is taken as for a line source of length 15 cm).

source particle spectrum in this direction, 3(E) the conversion factor from flux to dose (in the form of the equation as written, these are for the source particles), *B(E)* the dose build-up factor and the exponential term is the dose absorption by the components of the shield. The shielding lengths (λ_i) are also a function of energy.

The formula describes the shielding process as observed with more sophisticated **calculational** methods (see for example, references 62, 63, 64, 53), but to obtain 'correct' answers, values for the parameters must be chosen with care and the limitations of the method kept well in mind: *to a* certain ***extent,*** *the parameters tend to be somewhat* ***specific*** *to the* shielding *situation being considered.*

The formula is used in the point-source straight-ahead approximation, that is the source is considered to be a point and the external dose calculated on the basis of the material composition of the straight-line path from the source to the detector position. In some cases, dose rate distributions are calculated outside regions where large material inhomogeneity are present. Such distributions require smearing. The selection of parameter values will be discussed in section 17 of the Appendix.

8.2.2 High-energy Neutron Shielding Process

In this subsection the characteristics of neutron interactions are given in terms of extended captions for figures presenting results for iron and these results used to describe the high-energy neutron shielding process.

Cross-section information for iron is shown in Fig. 10. Only inelastic interactions are effective and these tend to disperse the incident particles energy via multiplicity (see Fig. 11), with the net result that initially more neutrons are present in the system than were incident. The secondary neutrons may be split between **high**-energy and fast. The 'high-energy' secondary particles go on to make further interactions, giving a particle cascade through the material (see Fig. **12).** The fast neutrons are slowed down (see Fig. 13) and eventually lost by absorption (mainly in the slowing down region). As the fast neutron source is distributed (due to the spreading of the high-energy neutron cascade) and the percolation distance quite large, the resultant spectrum is an average over a substantial spatial volume (see Fig. 14).

The complete spectrum deep inside a shield ranges from thermal energies up to several hundred MeV. The shape is stable mainly due to the fairly constant **high**-energy cross-sections and the large volume average. It is maintaining the equilibrium between the production by high-energy interactions and absorption in the intermediate energy region.

The approximate representation of the secondary **high**-energy cascade in Fig. 12 may be convoluted with the

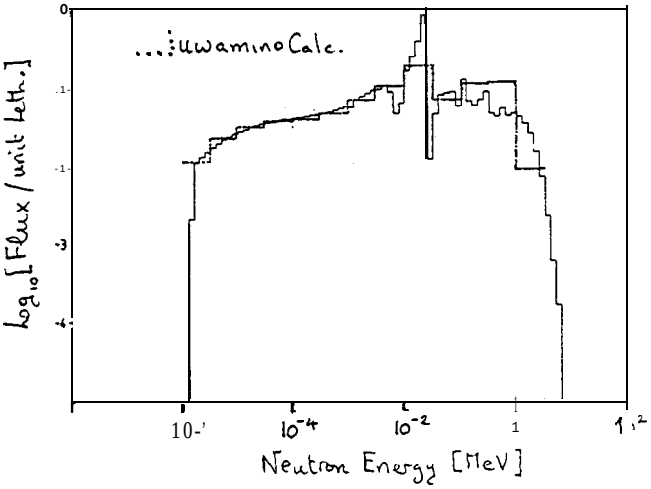

Figure 14: **The energy spectrum for lower energy neutrons in a shield. This is a weighted average of the spectra shown in Fig. 13 with weighting according to a 120 $g.cm^{-2}$ exponential. Also shown is the spectra as calculated by Uwamino [60].**

interaction probability to give estimates for the contribution of secondary particle escapes. For a 500 cm thick shield, about 90'% of the escape dose due to high-energy particles comes from secondary particles. About 60% of these secondaries are the result of collisions in the first 1 m and 20% from the next metre.

These results are in general agreement with those from **modelling** of the SINQ shield by Uwamino [60] using the 1-D **ANISN** [68] code and by Hernberger & Stiller [61] using the 2-D DOT [69] code. The fractional dose and **flux** as a function of energy are shown in Fig. 15. About **94%** of the dose comes from neutrons in the energy range 0.3 to 300 **MeV** and about 74% up to 100 MeV.

8.3 Activation Estimates

Under this heading comes a set of tasks as follows:-

1. Estimating the required radiological safety for the plant.
2. Design of the target transport flask.
3. Prediction of the active material inventory at end of plant lifetime.
4. Radiation dose rate estimates in plant rooms from circulating fluids.
5. Radiation dose estimates for caverns accessible after beam switch-off.

These all require calculation of the **nuclide** production followed by analysis of the decay chains by ORIHET and finally consideration of the decay radiation. For

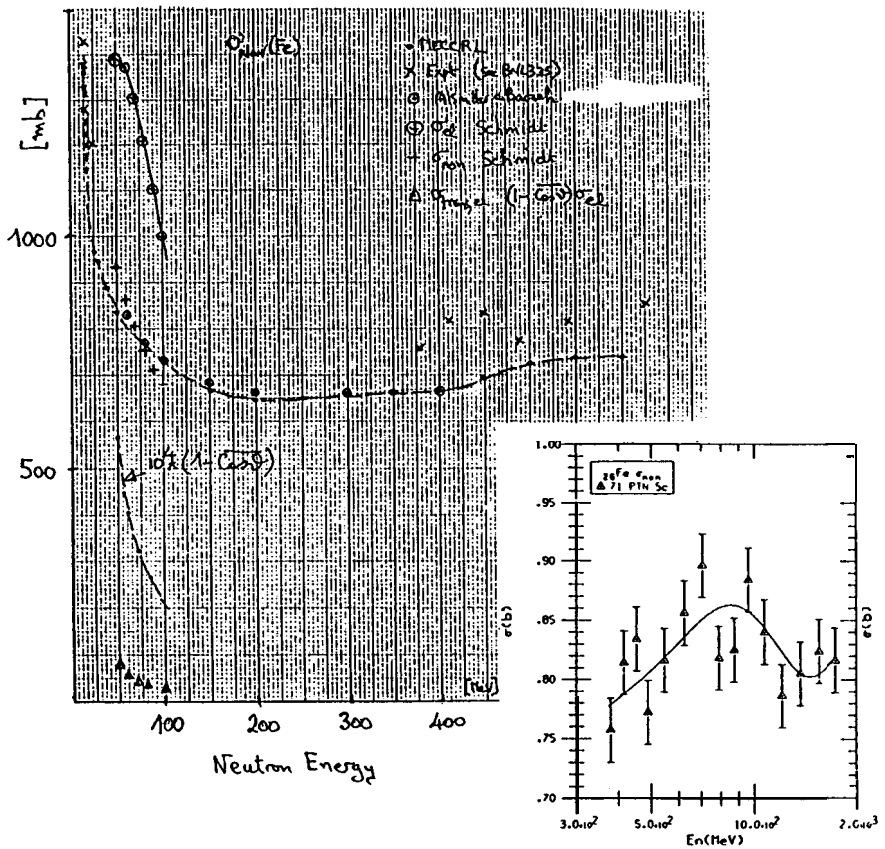

Figure 10: Cross-sections for Iron in the region 50 to 600 MeV. Results from experimental measurements are taken from BNL-325 [65] and Schmidt [66] and the calculated results come from Alsmiller and Barish [67] and a calculation made using the code MECCRL.

The characteristics are (i) an inelastic cross-section that falls to a roughly constant value in the energy region above about 200 MeV and (ii) a dying out of elastic scattering in this energy region mainly due to the anisotropy (for example, with Iron at 100 MeV the elastic cross-section is about 1 b but the mean cosine of the scattering angle is 0.979 giving, in the transport limit, an effective mean free path for elastic scattering of about 6 m).

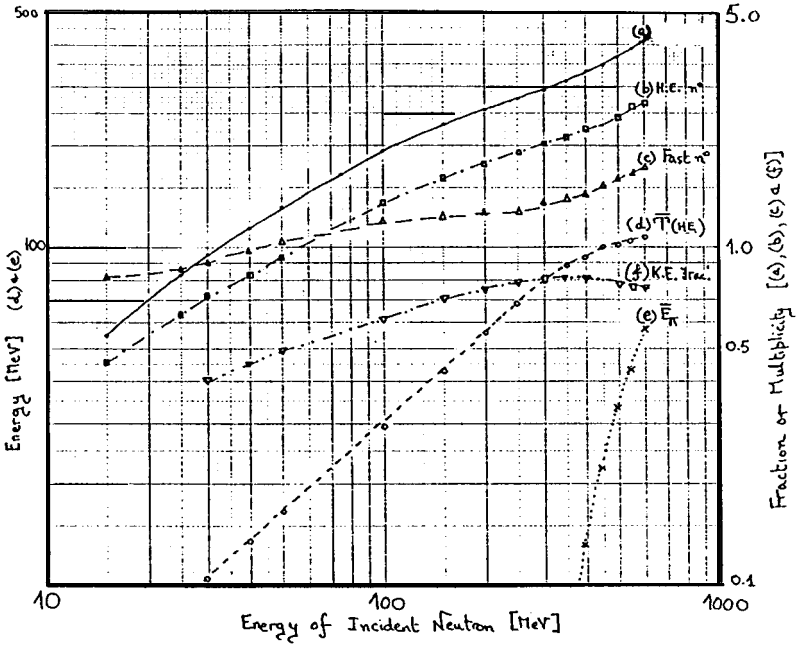

Figure 11: The general characteristics of high-energy neutron induced interactions with iron as calculated by the HETC programme.

(a) high energy nucleon multiplicity

(b) high energy neutron multiplicity: these neutrons can go on to make further interactions. The protons will make their interaction at a lower energy as they will be slowed by ionisation loss.

(c) average kinetic energy of the high energy nucleons.

(d) fast neutron multiplicity

(e) total energy taken by pions

(f) fraction of the incident particles' energy taken by secondary particles.

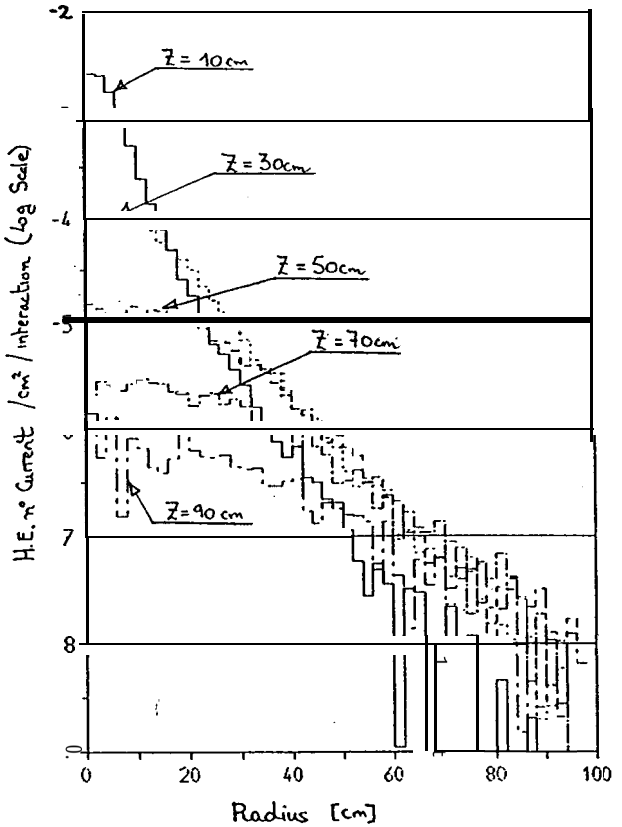

Figure 12: The spatial distribution of the forward high-energy neutron current. The figure shows the high-energy neutron current as a function of radius for 5 distances beyond the interaction point. The cascades are induced by a neutron spectrum corresponding to that at 90° to the SINQ target.
The results fit approximately (1.8 S.D on average) to the expression:

$$N(Z,r) = 0.79 \exp^{\frac{-s}{17.2}} \frac{1}{2\pi\sigma^2} \exp^{\frac{-r^2}{2\sigma^2}}$$

with $\sigma = 1 + 0.48Z^{0.94}$.
The effective absorption length for the cascade (17.2 cm) is slightly longer than the inelastic mean free path (average about 16 cm) hence the secondary intensity escaping the shield will be higher at the surface of the shield.

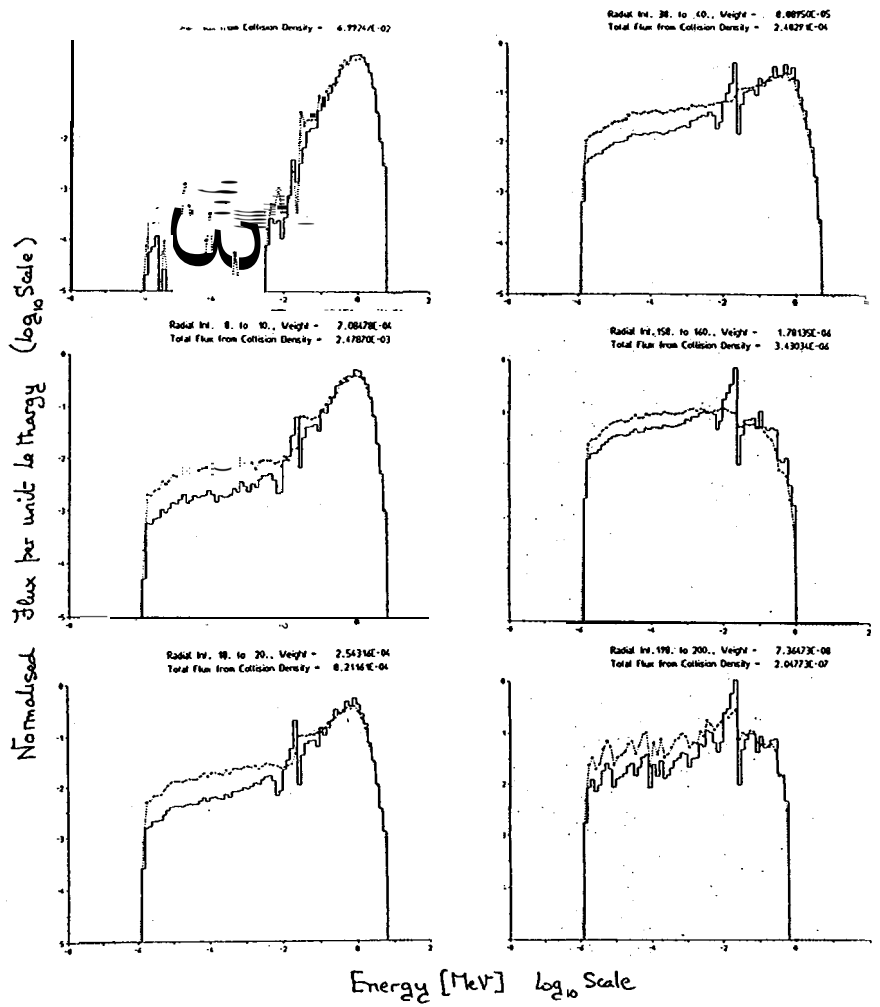

Figure 13: The evolution of the low energy neutron spectrum in iron. The spectra at various distances from a 1 MeV neutron source at the centre of a 2 m radius iron sphere are shown. Because of the characteristics of the iron cross-section the neutrons percolate quite large distances. About 82% of the neutrons are lost by absorption during slowing down and 12% in the thermal group. The remaining 6% escape the sphere.

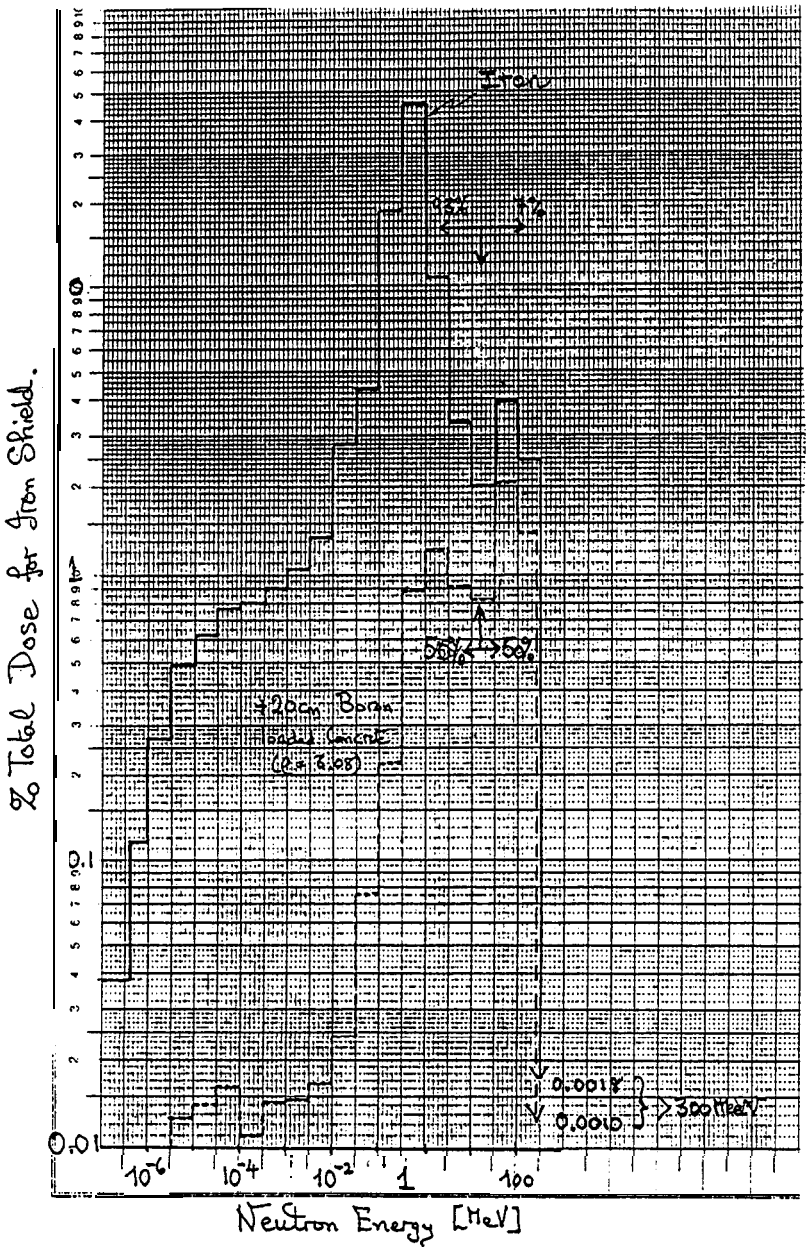

Figure 15: **The fractional contribution from the various parts of the shield neutron spectrum to the dose.**
(a) An iron shield: 93% of **the dose comes from neutrons below 15** MeV
(b) The spectrum from the same shield after adding a 20 **cm layer of boron-loaded concrete. This curve is normalised to the same scale as (a) - the dose is a factor of 13 lower.**

the target and moderator system nuclide production rates are calculated by the HETC package to give the contributions of the primary protons, the cascade particles and fast neutrons slowing to thermal energies. For the outer regions of the system the techniques employed so far exploit various approximation methods dependent on what is being looked at and the 'neutronic' position. These are described in section 18 of the Appendix.

Part II
Considerations of Nuclide Burning Facilities

9 The Relevance of the SINQ results

In the following subsections, some comments on the relevance of the SINQ calculations described in part 1 to an accelerator based nuclide burning facility will be given: the subsections will be headed by that of the relevant section of part 1.

A first general comment is that an accelerator can support several facilities simultaneously so that the end result of a nuclide-burning study need not consist of a single arrangement capable of doing everything but could consist of separate facilities optimised for given classes of nuclide.

9.1 Conceptual Design and Aspects of Optimisation

The major difference in the case of a nuclide burning facility is that the energy (and type of accelerated particle) is free. From the standpoint of a neutron source of the highest intensity 590 MeV is too low. The question of proton energy choice for a neutron source will be considered in section 10.

9.2 Neutronic Generalities

A nuclide burning facility which is to use thermal neutrons will have to take note of neutron economy with similar rigour. The advantage of the spallation-neutron approach is the lower heat of production (about 40 MeV per neutron compared to typically 100 MeV for a fission source). This advantage will be lost if fission channels are to augment spallation.

Dimensional considerations for the moderator will be different. Burning would be through a (large) fission cross-section and capture density would be the appropriate optimisation parameter.

The albedo effect is relevant as some moderator outside the burning region will bring advantages (use of the neutrons from fission). Limitation of power density in the inner shield layers will be necessary.

The spallation neutron source spectrum in the moderator tank will still include the high-energy tail. One would need to demonstrate that these neutrons do not cause the production of other undesirable species.

9.3 Target Systems

The design of the target system (i.e. the block of material to be directly struck by the accelerated beam) will be the major headache (technological challenge). The problems of heating, radiation damage, etc. will be common to a burning system - possibly rather worse if fissionable/ fissile material is to be burnt in this region.

If a liquid Pb target is considered, bringing the beam in from above would ease the major technical difficulty of window design.

For a thermal neutron based burning system, the need to keep the target small should be less stringent: larger target size would allow larger beam size and hence reduction of power densities. Selection of higher proton energy would also reduce power densities for equal incident beam power.

9.4 Alternative Targets

For the case of 'direct burning', the pebble bed concept might provide a useable geometry. More details of this system, including preliminary estimates of the hydraulics and mechanics of such a system may be found in reference 70.

9.5 Power Deposition

The HETC package seems to make a good job for the nuclear part of the estimate. As it is likely that a burning facility will involve more gamma energy (higher primary beam energy, strong fission sources) the treatment of this contribution would have to be improved (eg EGS or MORSE [71]).

9.6 Shielding Estimates

The point kernel approach should be more than adequate for the design of the shielding for a burning facility. The need to minimise the thickness should not be present and it will become more a question of finding a cost optimum. The shielding will not be dramatically thicker with the probably higher energy and current of such a facility as (up to several GeV) the high energy neutrons dictate the size and the shielding effectiveness of concrete and iron is not significantly worse (see

reference 72 and references therein). The picture will change somewhat at the high 10's of GeVs when muons start to dominate the situation.

9.7 Activation Estimates

A large volume of the shielding and all the materials of construction in the inner regions will end up as activated materials. This will need quantification and considered in the over efficacy of an accelerator based nuclide burning system.

One would imagine that remote handling will be a normal feature of such a plant system and hence considerations of activation dose rates will be different.

10 Choice of Proton Energy for a Burning System Based on Neutrons

The choice of optimum proton energy depends on what criterion is adopted: the highest useable thermal neutron flux with a given proton beam power or at a given power level in the target. For contiuous neutron sources, the results of Fraser [73] and of Coleman and Alsmiller [74] show that undisturbed thermal flux in terms of beam power has passed the maximum by 1500 MeV but is still rising in terms of beam power deposited in the target. Recent calculations by the author comparing neutron intensities produced by 3490 MeV and 570 MeV protons agree with these results but disagree on potential win.

A summary of the results of the calculation are given together with those obtained at 570 MeV in Table-I, which gives some statistics on energy deposition and neutron production and loss, and in Fig. 16, which shows maps of the 'thermal neutron' source in the moderator tank (this is taken to be the positions of the scatters that resulted in the neutron energy dropping below 1.4 eV) and maps of undisturbed thermal neutron flux in the tank at 1 MW beam power.

Comparison of the 3490 MeV and 570 MeV results for equal beam power shows that the higher energy brings advantages and also potential disadvantages:-

- The neutron flux at 25 cm from the target axis is about 6% higher with 3490 MeV protons (2.5 . 10^{14} /cm^2/sec/MW compared to 2.3. 10^{14}).
- The maximum power density in the target is about a factor of 2 lower and the total power to be removed from the target a factor of 1.4 lower with 3490 MeV protons. The detailed calculation results show that in terms of MeV/cc/proton, the contribution from ionisation loss by primary protons and secondary high-energy charged particles (79% of the total power density at 570 MeV and 38% at 3490 MeV) increases by a factor of about 2 and the contribution from ion recoils (15?70 and 46% at 570 and 3490 MeV) and also of gammas - E* and π^o - (5% and 15%) increase by a factor of about 10. This explains somewhat, why the power density reduction is not higher.
- The power deposited in the moderator system and radiated as escape high-energy neutrons are both higher (by factors of 1.8 and 3.0 respectively). This might be a serious drawback for materials mounted in the moderator tank.

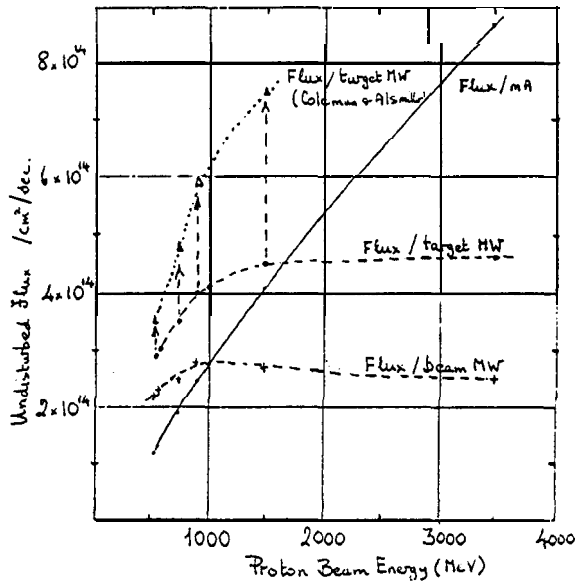

Figure 17: Undisturbed thermal neutron flux for 1 mA beam current, 1 MW beam power and 1 MW power deposition in the target as a function of energy of the incident protons.

The results of Fraser [73] (1000 MeV), Coleman and Alsmiller [74] (540, 750, 900 and 1500 MeV) are for 5 cm radius Pb targets with 2 cm standard deviation proton beam and those at 57o and 3490 MeV for a 9 cm radius target and approximately 4.4 cm standard deviation proton beam.

The results show a reasonably smooth trend in terms of equal beam current and equal beam power (see Fig. 17). The flux/M W for 3490 MeV confirms the downward trend and that the most efficient use of accelerator power is to select a proton beam energy somewhere in the region of 1000 MeV.

The calculated values for power deposited in the target are inconsistent but do agree that there is a downward trend as the proton beam energy is increased. The results of Coleman and Alsmiller give lower power depositions (about 12% less at 540 MeV rising to about 25% at 1500 MeV). This can be partly explained from the different target/beam-size combinations used and differences in approximations. Consequently, two sets of results have been constructed, the first using the calculated target powers and the second resealing the Coleman and Alsmiller results to values interpolated

Table-I

Neutronic Parameters from the Calculation of SINQ with 3490 MeV and 570 MeV protons.

	Energy Deposition		
Component	3490 MeV MeV/p	570 MeV MeV/p	570 MeV MeV/6.12 p
Target	1870	426	2610
Central Column	9.6	1.1	6.6
D_2O	**454**	**43.1**	**266**
D_2O Tank wall	4.8	0.26	1.6
H_2O	20	1.1	6.8
H_2O Tank wall	1.1	0.09	0.55
Totals	2360	472	2890

	Neutron Absorption		
Component	3490 MeV /P	570 MeV /P	570 MeV /6.12 ps
Target	16.9	2.0	12.2
Central Column	3.7	0.53	3.3
D_2O	7.41	1.05	6.43
D_2O Tank wall	5.84	0.79	4.82
H_2O	45.62	6.08	37.25
H_2O Tank wall			
Totals	79.46	10.45	63.98

	Other Parameters		
Component	3490 MeV	570 MeV	570 MeV (6.12 p)
Maximum Thermal Flux (1 mA)	1.3.1015	2.0.1014	1.2.1015
Thermal Flux at 25 cm radius (1 mA)	$8.7 \cdot 10^{14}$	1.3.1014	$8.2 \cdot 10^{14}$
Neutrons /Int. in Target	6.81	6.53	
Int./proton in Target	9.12	1.37	(8.39)
Neuts/p in Target	62.12	8.93	54.7
Neuts/p outside Target	14.06	1.36	8.33
Neuts/p from fast neutrons	6.58	0.582	3.56
Fast & Epi Escapes	o.51-	0.06	0.37
Thermal Escapes	1.37	0.304	1.86
Escape H.E. neuts K.E. (MeV)	285	16.1	98.6
Peak Energy Density MeV/cc	1.0	0.36	2.2

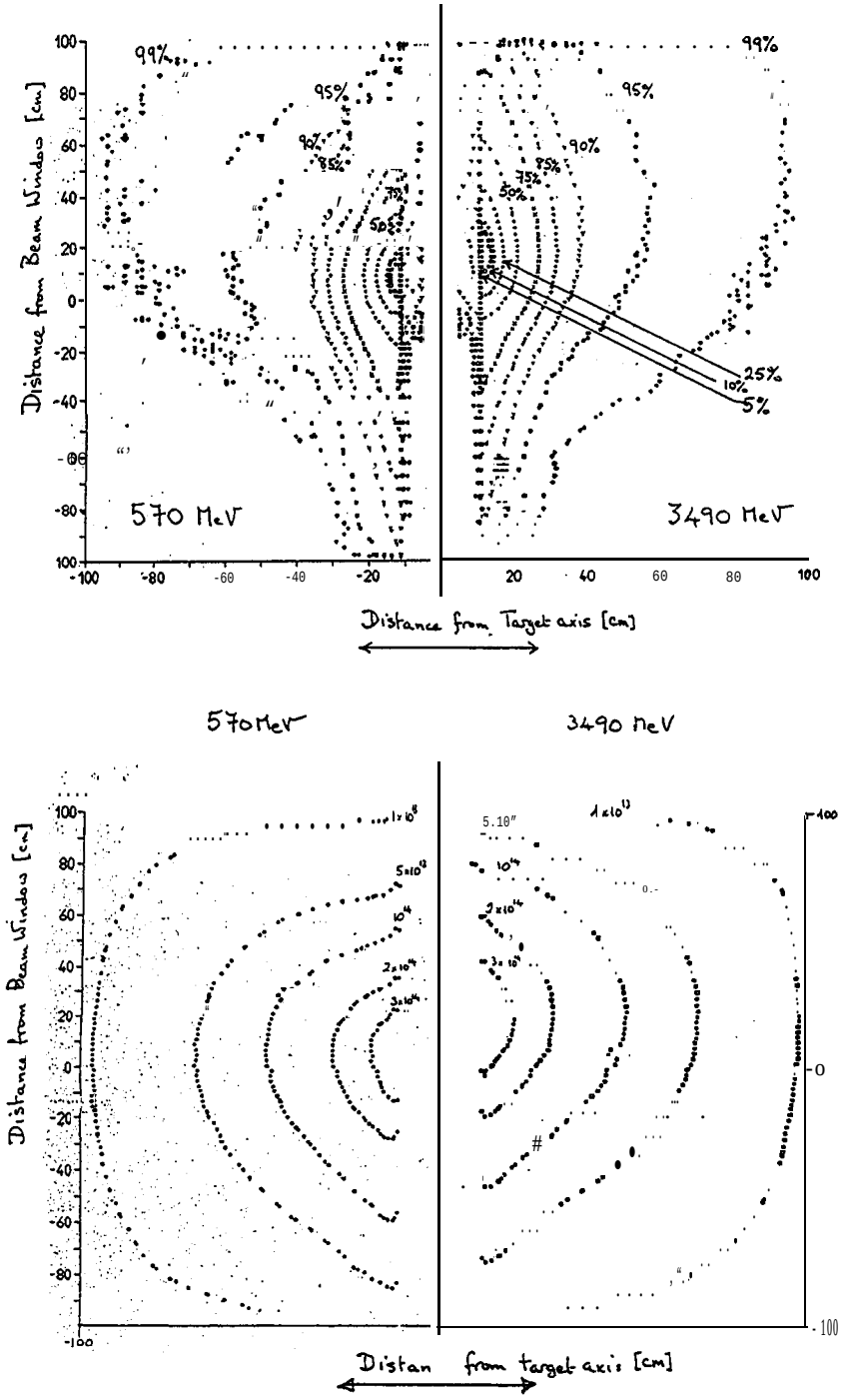

Figure 16:

(a) **Contours enclosing given fractions of the thermal neutron source. On the right for 349o MeV protons and on the left for 570 MeV.**

(b) Contour lines for equal undisturbed thermal neutron fluxes at 1 MW beam power. On the right for 3490 MeV protons and on the left for 570 MeV.

from the other target power deposition values.

Both sets of results show that if power in the target is the major problem in the fight for highest possible neutron fluxes, then increasing the beam energy is a good thing to do. The Coleman and Alsmiller results indicate a far better win. For the 'other' results, there may be a flatish maximum somewhere between 2 and 3 GeV: a couple more points would be needed to establish this.

11 Calculational Requirements Specific to Nuclide Burning

The fundamental job is to decide on the transmutation channel(s) to be expoited. Once this is decided then will follow the choice of accelerator system (type and energy of particle).

The calculational needs are obvious: a means of calculating the nuclide production by all contributing channels for the 'spectrum' of plausible candidate burning particles; a Bateman equation solver and (most important) a figure of merit that allows judgement of how well (or badly) a particular system is performing.

Plausible candidate burning particles are electrons (and/or synchrotron-radiation, these will not be considered in this paper), medium to high-energy nucleons, fast and thermal neutrons, negative pions, light ions and heavy ions.

The calculations for fast-to-thermal neutrons should present no problems as extensive codes systems and data bases of cross-section information exist.

11.1 Medium Energy Nucleon and Meson Cross-sections

The main features of high-energy particle interactions are (i) the trend for the mass of the residual nucleus to be increasingly lower than that of the parent as the energy is raised, (ii) the increasingly large (with higher incident energy) spread of the masses of the products and (iii) the possibility of fissioning comparatively light nuclei. The available cross-section information is sparse particularly in relation to the size of the energy range and target mass range available. The need for calculation is almost self evident. The major question is whether available codes are adequate for the main task which is, to predict the production rates for nuclides with similarly unpleasant characteristics to those being burnt (i.e. properly assessing the gain of carrying out the procedure).

The two part Intranuclear Cascade Evaporation model based on the Serber model [24] is available in at least three basic forms (Bertini [25], Chen et al. [75, 76, 77], Barashenkov [78]). The results from these basic forms were compared [78] and apart from some noticable discrepancies arising from detailed difference in the implementation of the Serber model, were generally in good agreement.

Here at PSI, the Bertini version is available for the calculation of the partial cross-sections for the interaction of nucleons in the energy range 15 to 3495 MeV and charged pions from 2 to 2200 MeV. Target nuclei in the mass range 5 to 260 (Note: in the original version the upper limit is 239) can be calculated but results for nuclei of mass below about 20 are to be treated with caution (Note: hydrogen and deuterium interactions are t rested separately).

The second stage is treated with the EVAP code of Dresner [29] based on the statistical model, but extended to treat fission for all nuclei of Z greater than 70. It should be noted that the EVAP code and also the fission treatment are somewhat a balance between (i) the need to treat a very wide range of nuclear states, (ii) accuracy and (iii) speed (a spin independent level density formulation with global parameterisation, rather simple parameterisation of the inverse cross-sections, etc). The Bertini code allows calculations over the full range of nuclides and the intranuclear cascade results in products that are spread over a range of charge, mass, and excitation states: EVAP has to treat all possibilities in a reasonable fashion.

More accurate prescriptions for treating evaporation are available [79, 80, 81, 82, 83] but are more suited to the calculation of limited numbers of specific cross-sections. They are too complicated for a 'workhorse' nuclear physics code such as HETC.

It should be noted that the region from 15 to 50 MeV (where the interaction can be considered to be changing from 'full' compound nucleus to 'full' Serber) is not well treated. Calculated cross-sections using the optical model for neutrons up to 40 MeV have been produced [e.g. 86].

11.2 Ion Cross-sections

A locally written code for calculating light ion cross-sections using the Thomas method [87] in combination with the EVAP code has been used for fission work (fission probabilities information at high excited states have been studied with ions [89, 90, 88, 91, 92, 93, 94, 95, 96, 97]). Potential function parameters are taken from Igo [98] for a-particles and are available from the work of Sikkeland [91] for ^{12}C, ^{14}N, ^{16}O and ^{22}Ne.

For heavy ions, the recent survey of Schmidt and Morawek [99] in the context of the synthesis of heavy nuclei gives much relevant information.

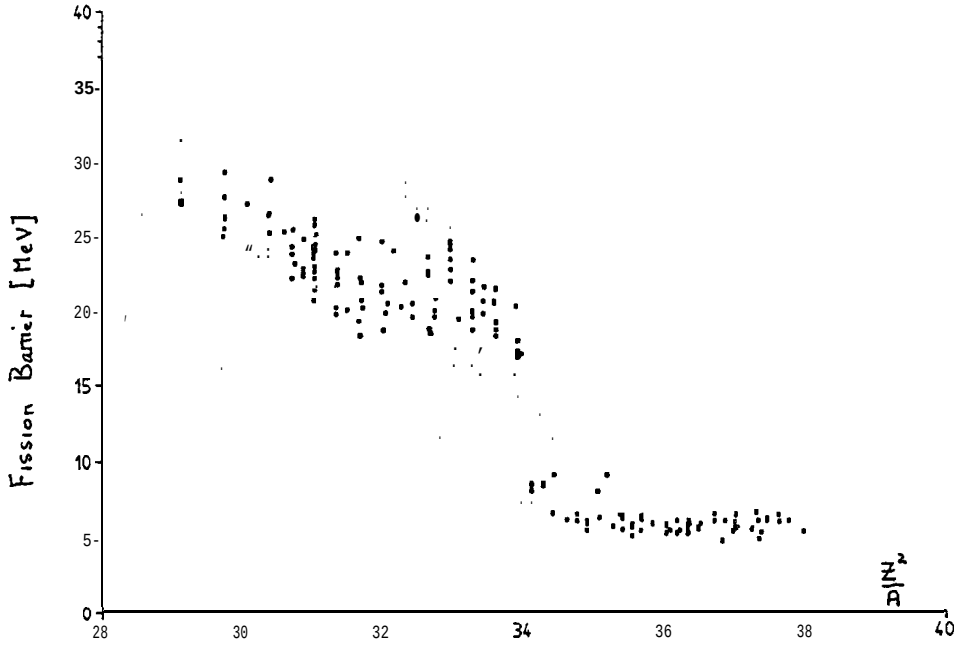

Figure 18: **Measured fission barrier heights as a function of the fissility parameter. The data comes from Dahlinger** et al. [101].

11.3 Fission Cross-sections

The fission treatment [30] used in the PSI version of the HETC package can be considered as a three step process: (i) the **intranuclear** cascade, (ii) evaporation with fission competition and (iii) when fission occurs, the choice of the parameters (Z, A, E') for the **scis**sion fragments. The main emphasis for waste transmutation is **on** the residual mass distribution. In the 'spa.llation' region this is considerably influenced (or dominated) by fission competition.

The fission cross-section is determined at the evaporation stage using fission probabilities based on (low excitation energy) systematic [100] for nuclei of charge number 89 and above. Below this Z value (and down to a programmed minimum of Z = 70) statistical model extrapolation of measured data is used. This is necessary while little or no experimental information on fission in the region Z = 85 to Z = **88** has been found. The change in the character of fission across this region is clearly seen from a plot of fission barrier values (Fig. 18). The need to have a wide range treatment comes from the spread of the possible nuclei. These will be both directly produced in the high-energy part of the interaction and also arise from multiple chances during the evaporation process.

The choice of scission product parameters (Z, A, E*) is based on 'complete' splitting and the nuclear state at the moment of fission. Parameterisation of mass and recoil energy spread is based on available experimental data and the final fission fragments reached after any evaporation has taken place. That is, the sum of the production cross-sections for the fission fragments is constrained but their (Z,A) distribution is somewhat decoupled.

A selection of results from cross-section calculations over a range of heavy-mass systems made using the **Bertini** code, the Thomas Model, compound nucleus and EVAP code (as modified to treat fission) are given as **follows:-**

- a-particle induced fission cross-sections (Fig. 19). The experimental data was used as the basis for the parameterization of the statistical model used up to $z = 88$.
- Some a-particle cross-sections for heavy elements: fission and **spallation** for ^{238}U **and** ^{238}Pu (Fig. 20) and (α, 4n) cross-sections for ^{226}Ra, ^{230}Th, ^{232}Th and ^{244}Cm (Fig. 21).
- Some fast neutron induced cross-sections - mainly fission cross-sections and calculated using the compound nucleus model with total cross-sections taken from **ENDF/B-IV** (Fig. 22 to 25). These **basicly** show the quality of the Vandenbosch and Huizenga correlation [100] but also indicate that there is a problem in the energy region where the transition from full compound-nucleus to full **Ser**ber models takes place (see results for ^{238}U in Fig. 23).
- High energy proton fission cross-sections (Fig. 26).

In general the agreement is reasonable.

Measurements of both fission and spallation products for the same particle-nucleus system have been found for ^{238}U bombarded by 340 MeV protons: some of the fission products were measured by Stevenson et al. [104] and some spallation products by Lindner and Osborn [105]. The calculated and measured results are shown in Fig. 27. The two experiments disagree on the total fission cross-section (1590 mb compared to 1370 mb [105]).

The width for the fission products mass distribution is a little higher than the measured values (the calculated cross-sections at the peak are about 40% lower) and comparisons for spot nuclides are up to a factor of 10 lower.

Quite good agreement for the high-mass end of the spallation products is obtained and spot-nuclide cross-section values are within a factor of 2 to 4. For the total production rate of the heavy elements the agreement is also quite good (Np, 0.4 for measured over calculated; U, 1.1; Pa, 1.3; Th, 2.1; Ac, 1.2). The sum production cross-section for the mass 210 nuclides At, Po, and Bi was measured to be 4.5 mb (calculation gave 5.1 mb but shifts the peak production to At). This gives a tentative indication that a rise in cross-section toward the region mass 200 may be real. It occurs in the calculation by needing to restrict fission competition to neutron emission (we only have indications of fission to neutron widths ratios and putting all evaporation in competition disadvantages charged particle emission too severely) and hence as this low mass region is only reached via charged particle emission it is relatively little affected by fission as may be seen in Fig. 27 from the fictional spallation yield curve as calculated by disabling fission.

11.4 Final Comment

The comparisons between calculation and experiment are for thin target systems. In any realistic waste burning system, the production will be in 'thick' targets and hence an average over a wide spectrum - the slowing down of the primary particle and also the accompanying cascade/evaporation neutron spectrum. The coupling of the errors in calculating single events to the error in the prediction of a thick target system is not known. This will need checking by experimental measurement.

Acknowledgement

I gratefully acknowledge the direct and indirect help of many people that has made it possible to write this paper:

Walter Fischer for bringing me into the SINQ project and for many years of good councel.

Peter Wydler and Hans-Ulrich Wenger for many discussions on accelerator waste transmutation.

All colleagues in the SINQ project.

Tim Broome and other former colleagues of the Rutherford Appleton Laboratory's SNS project (now ISIS).

My wife for patiently proof-reading and correcting the whole document.

Renate Bercher for her help in production of figures.

The work on including fission into HETC was done in collaboration with Prof. Dr. J. Ranft of Leipzig University and while the author was a member of the Rutherford-Appleton Laboratory.

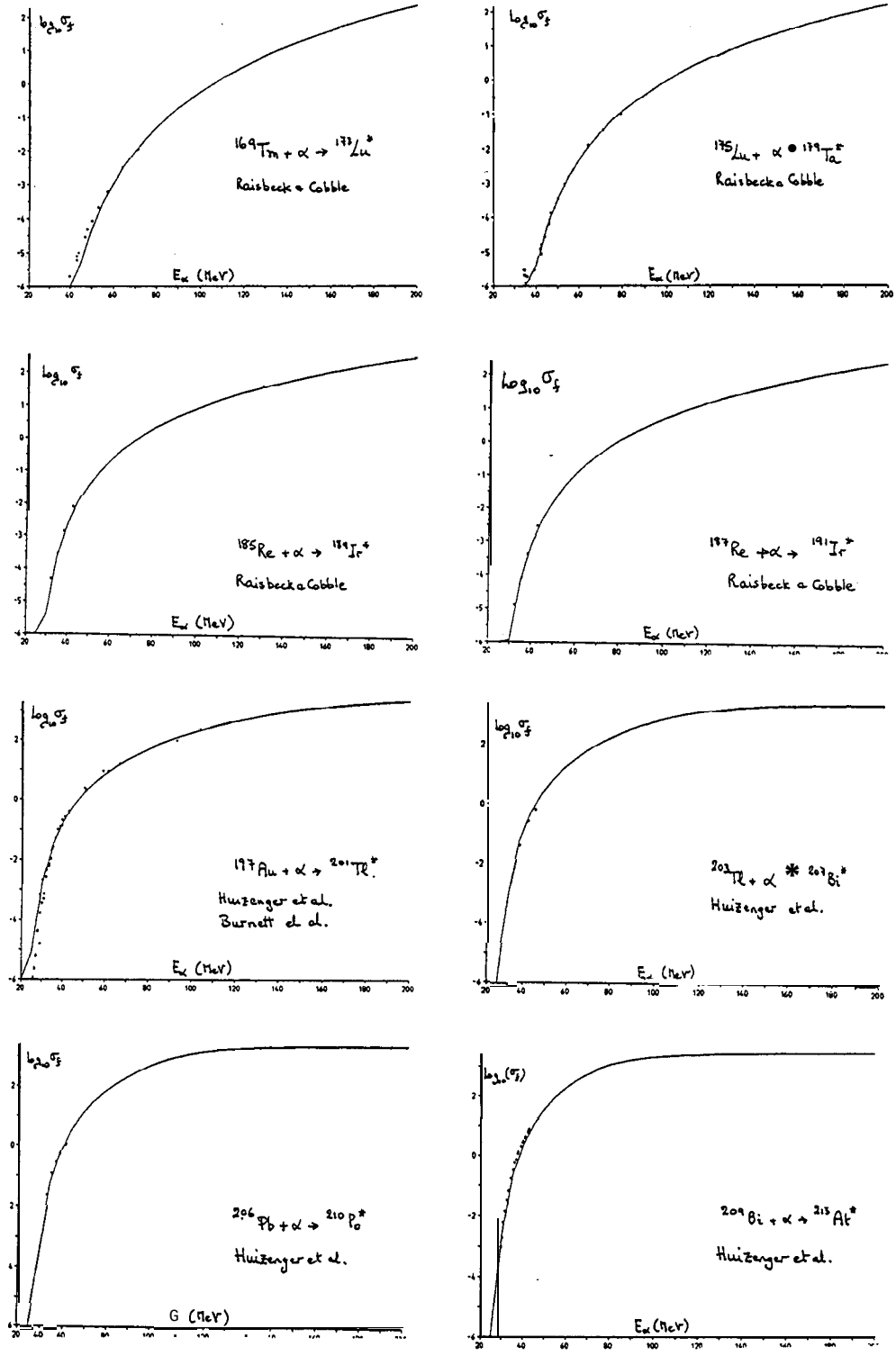

Figure 19: A selection of a-particle induced fission cross-sections for elements up to Bi. The dots are experimental data and come from Raisbeck & Cobble [88], Huizenger et al. [89] and Burnett ● t al. [90]. The lines are the results of calculation.

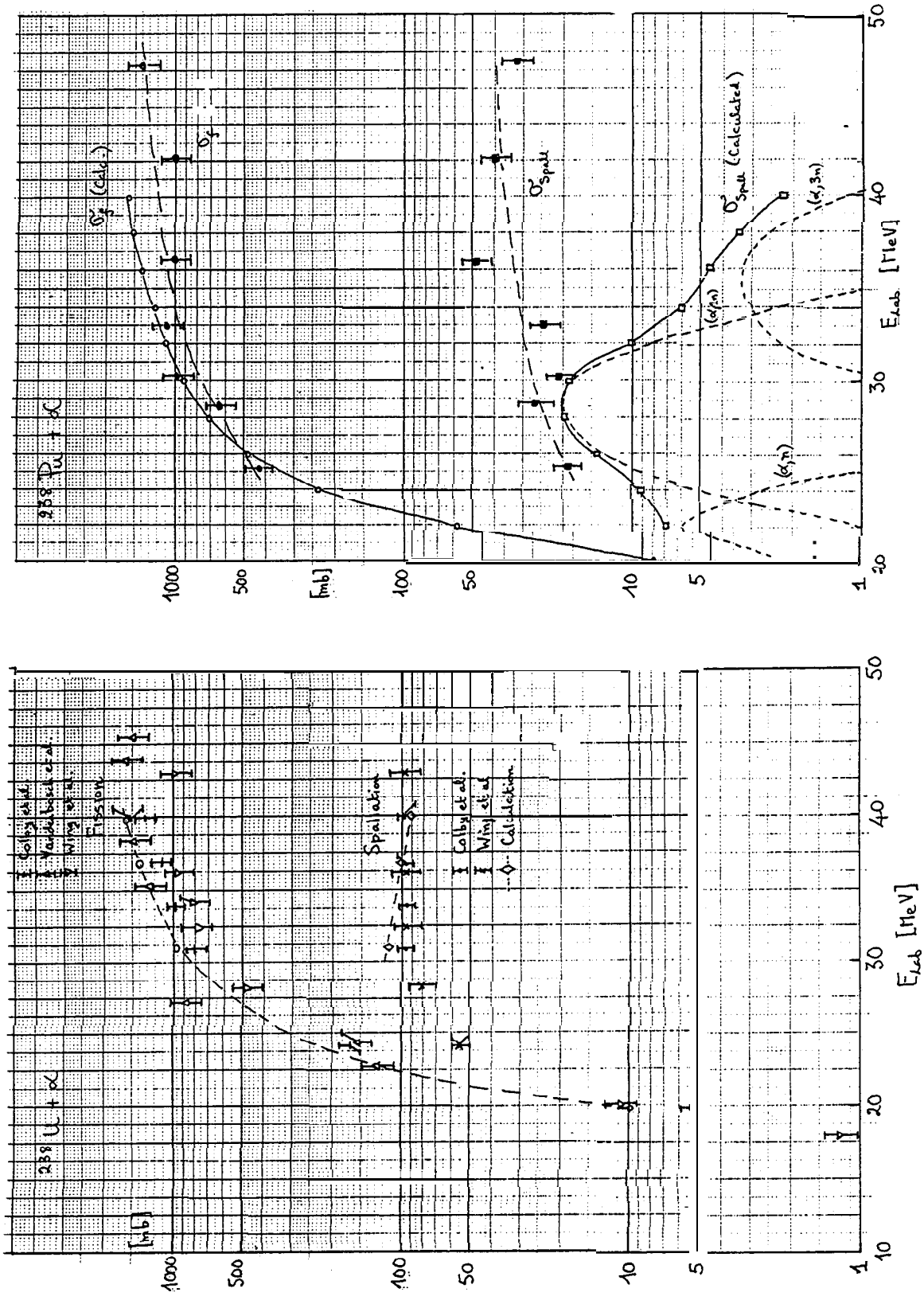

Figure 20: Calculated and measured α-particle induced cross-sections for fission and spallation of ^{236}U (results from references 93, 95, 94) and ^{238}Pu (results from reference 97).

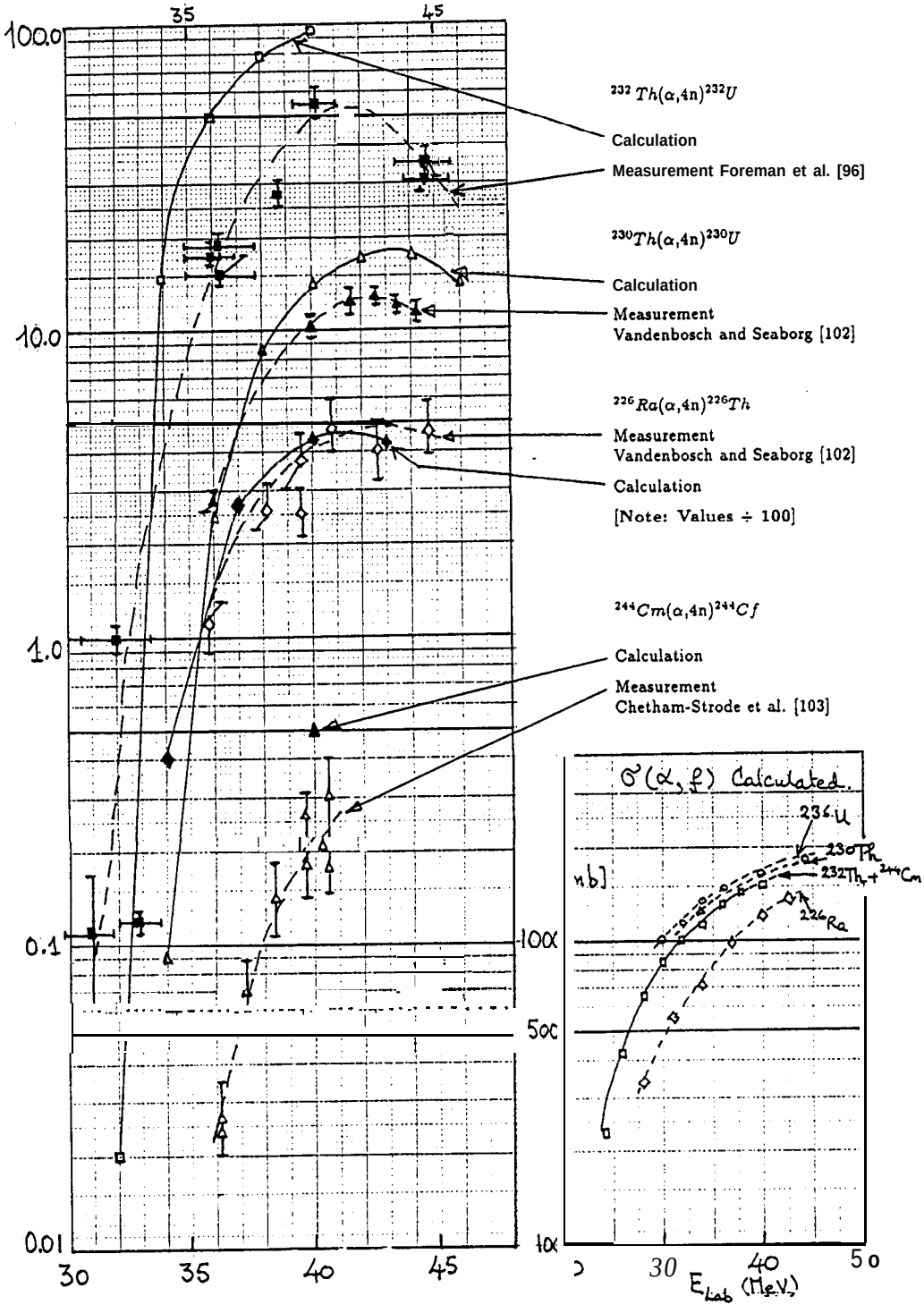

Figure 21: Calculated and measured $(\alpha,4n)$ cross-sections for ^{226}Ra [102], ^{230}Th [102], ^{232}Th [96] and ^{244}Cm [103]. For reference, the calculated fission cross-sections are included as an insert.

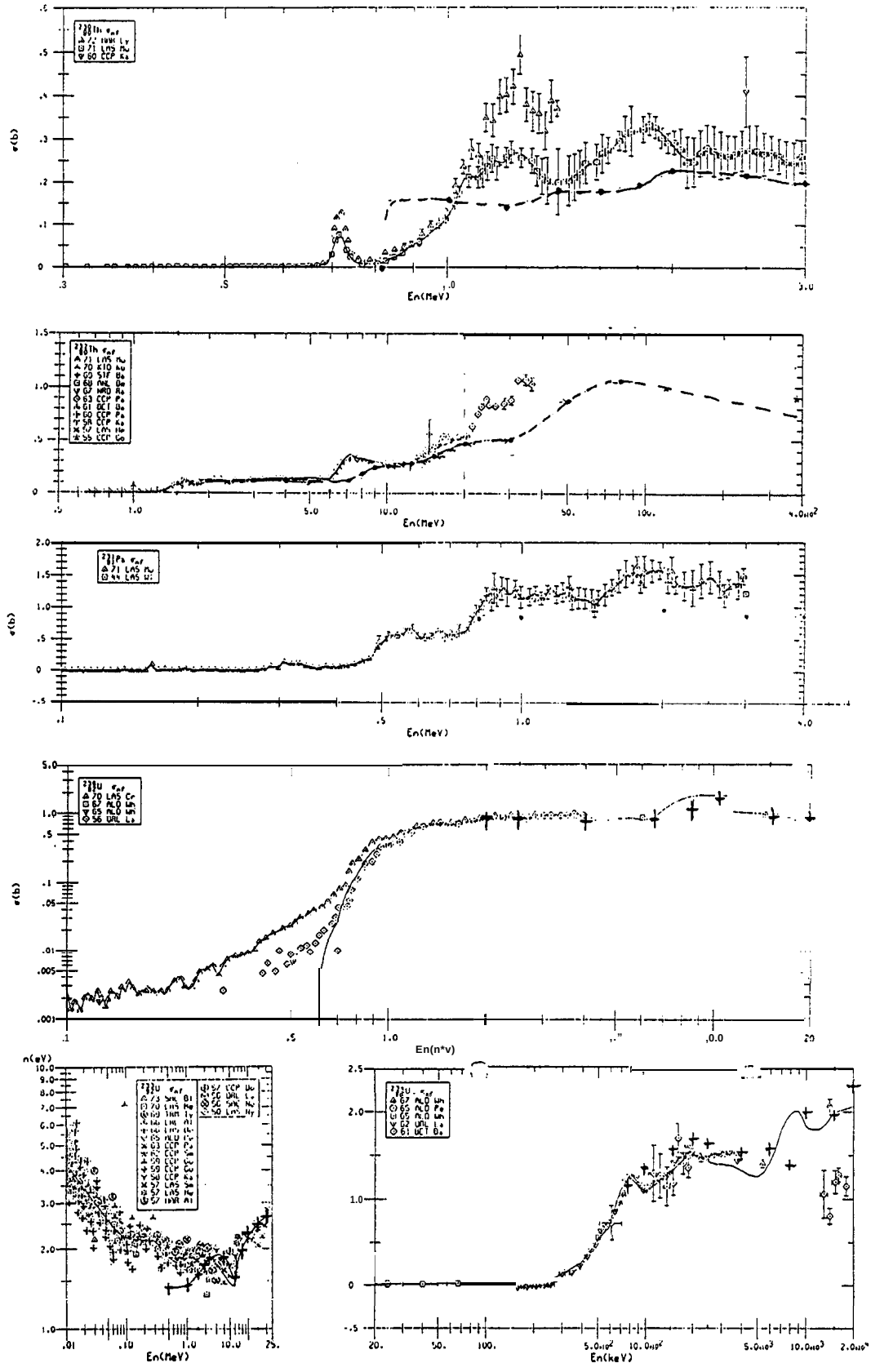

Figure 22: Fast neutron induced fission cross-sections.

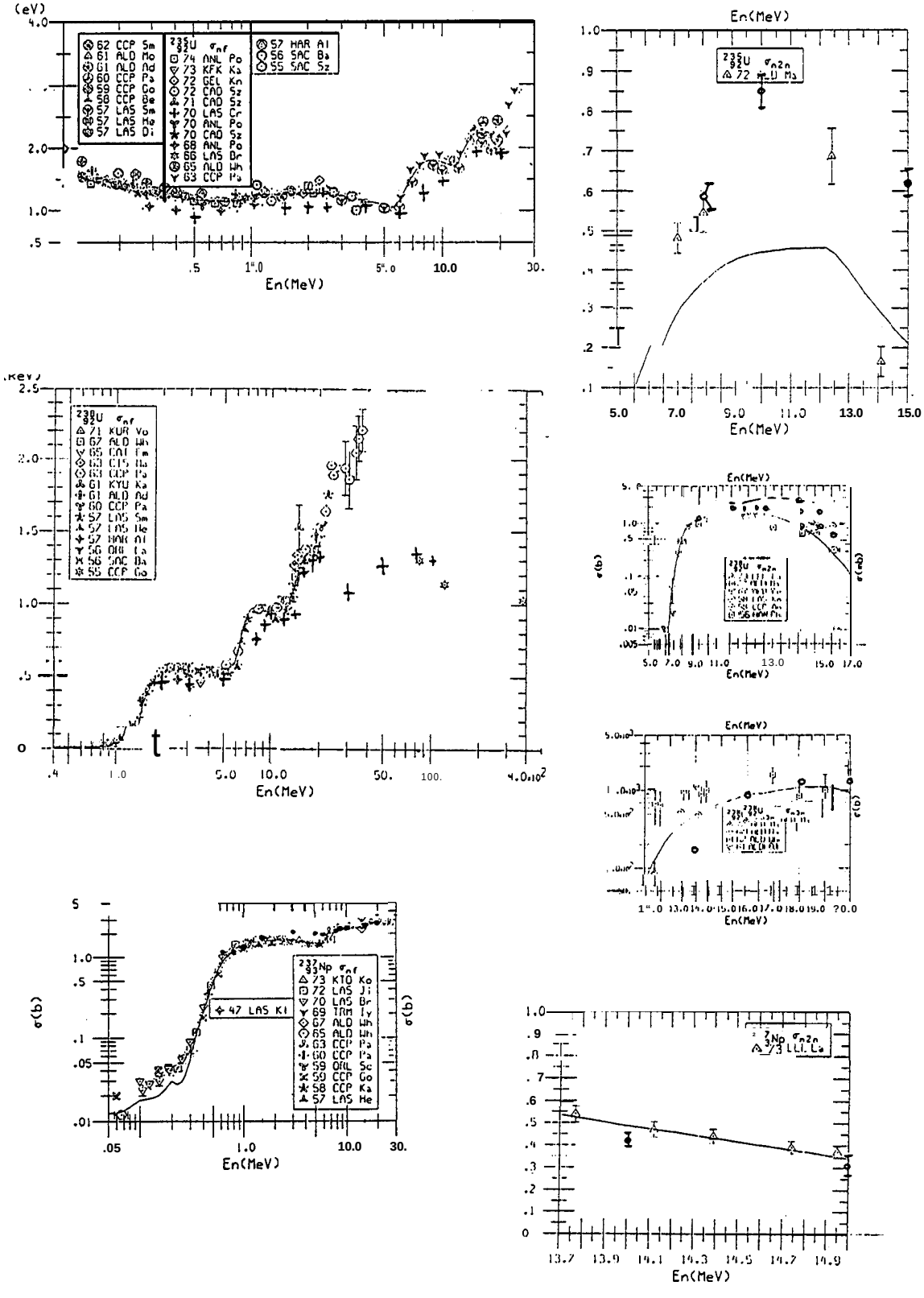

Figure 23: Fast neutron induced fission cross-sections.

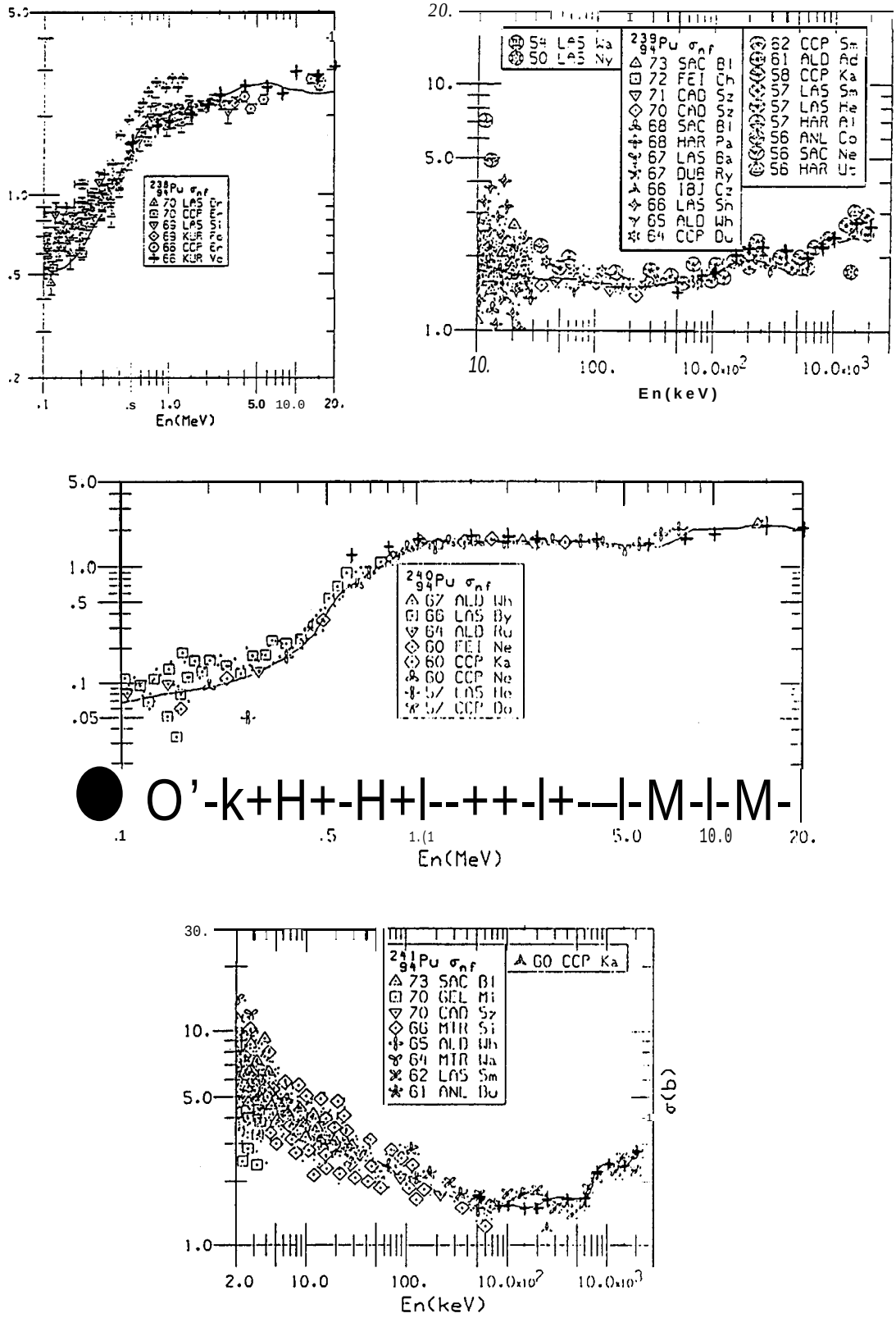

Figure 24: Fast neutron induced fission cross-sections

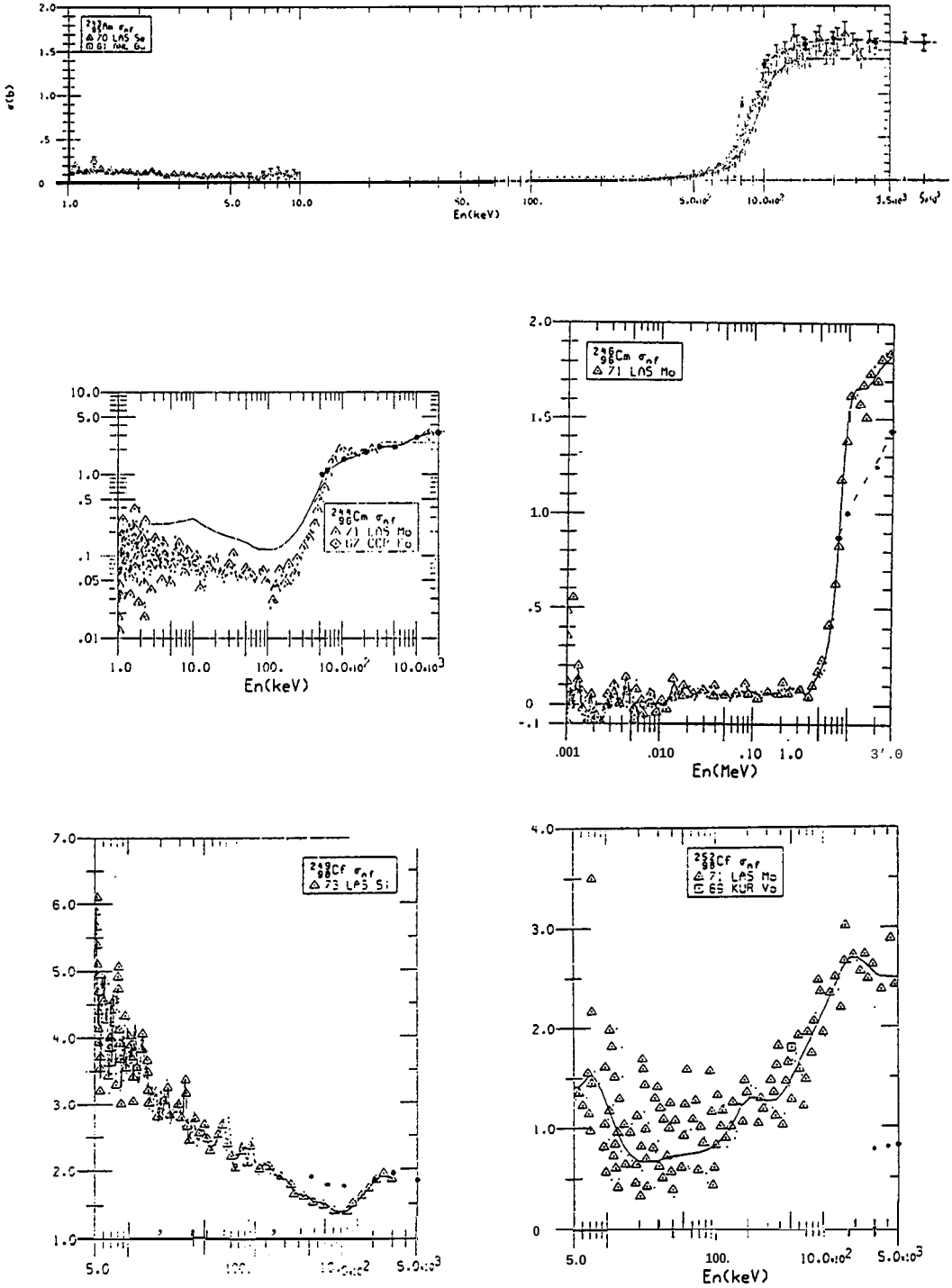

Figure 25: **Fast** neutron **induced fission cross-sections.**

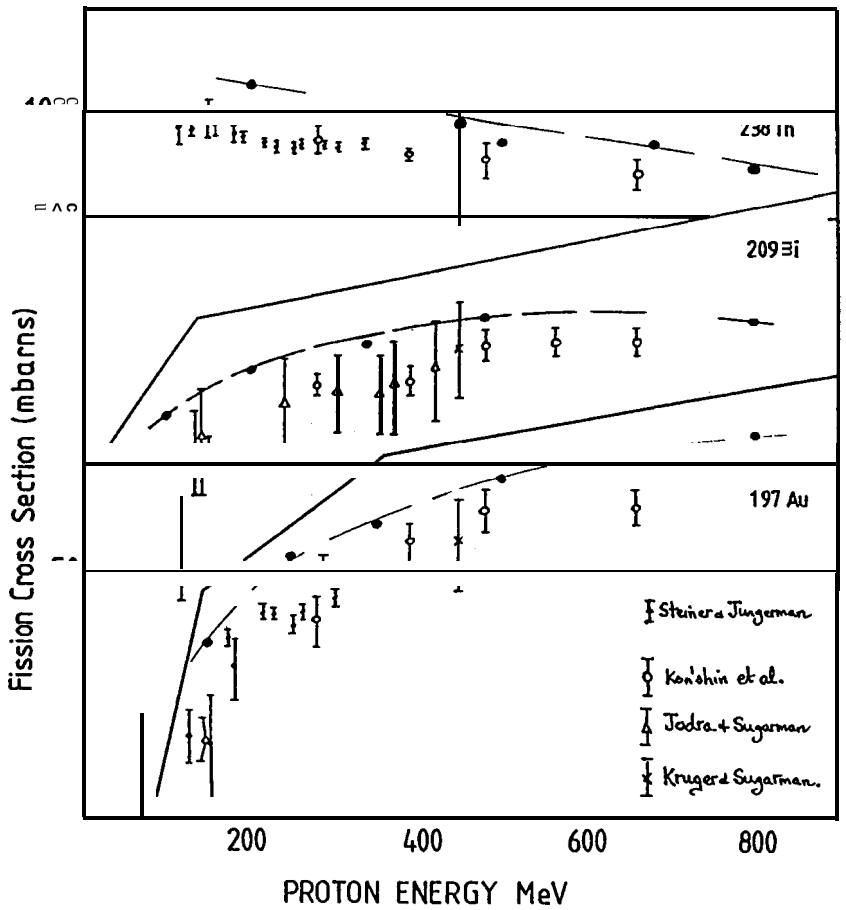

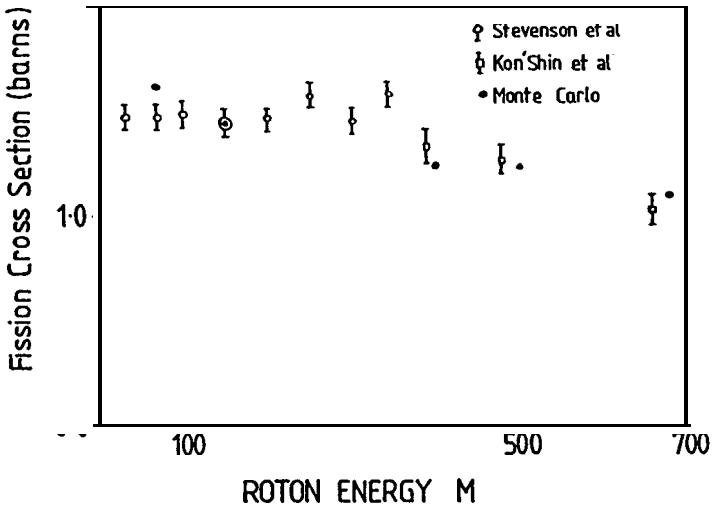

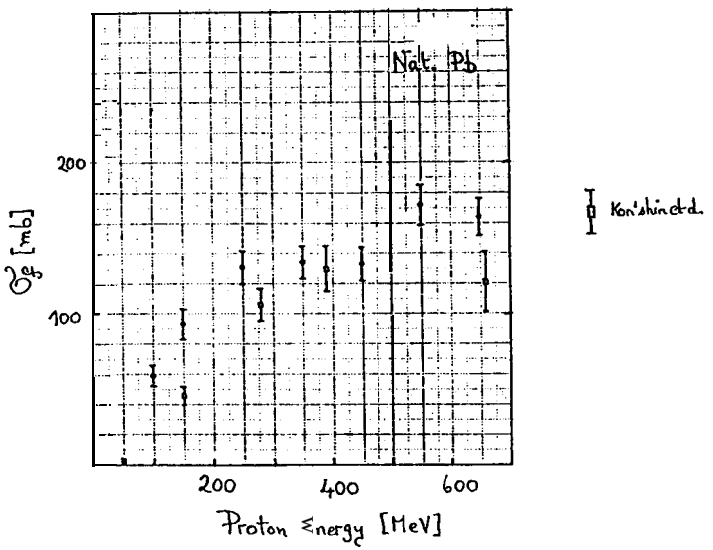

Figure 26: High-energy induced fission

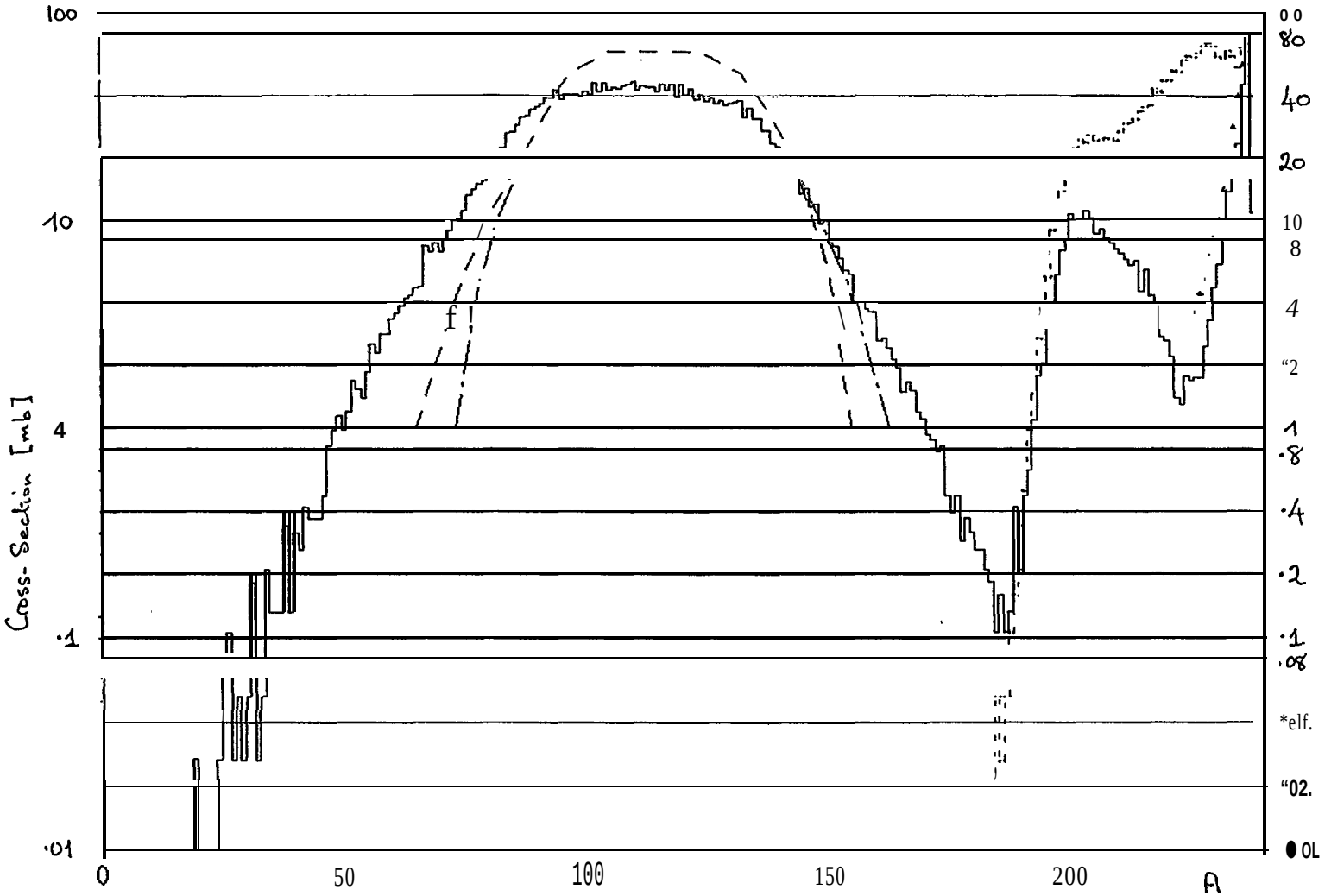

Figure 27: The calculated maas distribution from bombardment of ^{238}U with 340 MeV protons. Measured values come from reference 104 for the fission products (dashed lines) and from [105] for the spallation products (triangles). For reference purposes the spallation product mass distribution with fission disabled is also ahown.

Appendix: Some Further Considerations of SINQ Calculations

Further detailed considerations of SINQ and some calculational results have been collected into this appendix. In the original concept for the paper they were included into the main body of the text but interrupted the main purpose too much.

12 Moderator Considerations

In this and the following two sections, the "Neutronic Generalities" of section 7 are pursued further with more detailed considerations of the moderator and target design.

D_2O is clearly the best moderating material for a continuous neutron source. The fast neutron spectrum from spallation reactions is not significantly different from that from the fission reaction so the dimensional requirements from the slowing down process are similar to those for a research reactor. The main differences in optimizing the dimensions come from:

- The neutron production process is decoupled from the thermal flux in the moderator - essentially this allows greater freedom in the choice of beam-tube dimensions and in particular the window cross-section may be larger.
  This also means that the target/moderator neutronics can be studied without the need to consider the beam tubes (by exploitation of symmetry, the undisturbed thermal neutron flux distribution can be estimated comparatively quickly and accurately by a variety of methods, diffusion theory, S_n methods, Monte-Carlo, etc).
- The presence of high-energy neutrons.
- The biological shield is significantly thicker as it is to handle 'high-energy neutrons.

The choice of tank radius is a balance between the gain in thermal flux in the inner region against transmission loss. This does mean there haa to be some compromise as the transmission loss is different for beam-tubes and guides: for beam-tubes up to the monochromator it is a straightforward solid angle effect, for the guides the transmission is almost independent of tank radius and maximizing the thermal flux in the region of the cold source is best.

A further consideration is the thermal neutron albedo of the material outside the D_2O . The thermal neutron reflection coefficient for water is considerably better than for iron (80% compared to 30%). The flux gains at a H_2O/D_2O compared to a Fe/D_2O interface are shown as a function of H_2O layer thickness in Fig. 28. The thermal flux increase at the position of the maximum is about 8%. In addition, the reduced thermal flux at the innermost iron of the shielding bring great advantages in terms of cooling.

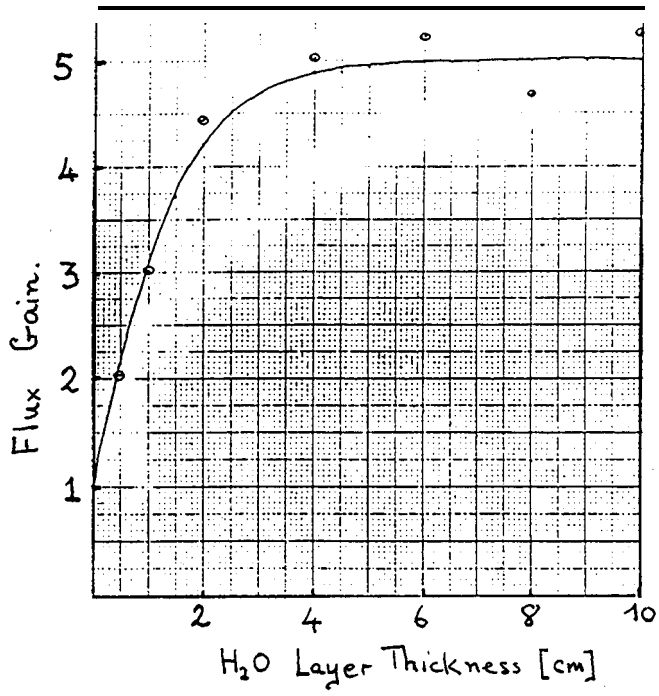

Figure 28: Calculated flux gain at the D_2O/H_2O interface compared to a D_2O /Fe, as a function of thickness of the H_2O layer.

The beam tube tips should be positioned as close to the undisturbed thermal flux maximum *as* possible but subject to:

- Flux perturbation by the beam tubes
  SINQ is to use 'trouser-leg" beam tubes - two monochromator plus instrument systems to a beam tube. The flux perturbation constrains the choice of tube size and the radii for the beam tube tips. Two effects need consideration: (i) the coupling between beam tubes and (ii) the effect of dimensions on thermal neutron intensity at the monochromator.
- Backgrounds
  The major difference between a spallation-neutron source and a research reactor is that the neutron spectrum extends to higher energies (this leads to the very much larger thickness for the bulk shield). These only make-up a very small part of the overall unwanted neutron intensity but are awkward to shield against, The potential sources of such neutrons are illustrated in Fig. 29 and a representative spectrum for a beam tube is shown in Fig. 30. As far as moderator tank design is concerned, this means that the beam tubes will be mounted tangentially to the target to minimise the high-energy

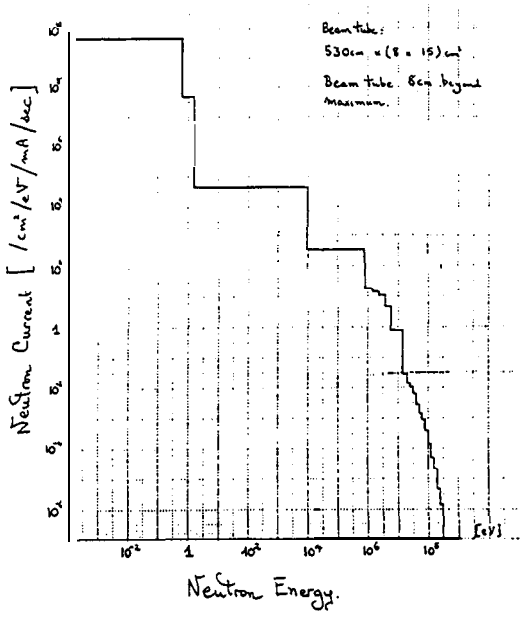

Figure 30: A representative **spectrum in a tangential beam tube.**

neutron component in the beam (see Fig. 31).

- Power deposition in cold sources.

13 Target Considerations

The considerations of the target are particularly relevant for all forms of accelerator based transmutation systems. The SINQ target is a complete system consisting of several parts:

a replaceable unit consisting of (a) the beam window, (b) the neutron producing region and (c) a shielding plug.

an external cooling loop

a system to dismount and transfer used targets to the storage area and to mount new targets.

The layout of SINQ in the region of the target is shown in Fig. 32.

The major constraining influence is activation and/or the consequences of activation:

- of the target material itself and its accompanying after-heat - the consequences of escape of target material from the target.
- of the coolant and hence the imposition of constraints for the layout and handling of the external plant.
- radiation damage to the target container (mainly the proton beam window) and its consequences on the mechanical integrity of the containment.

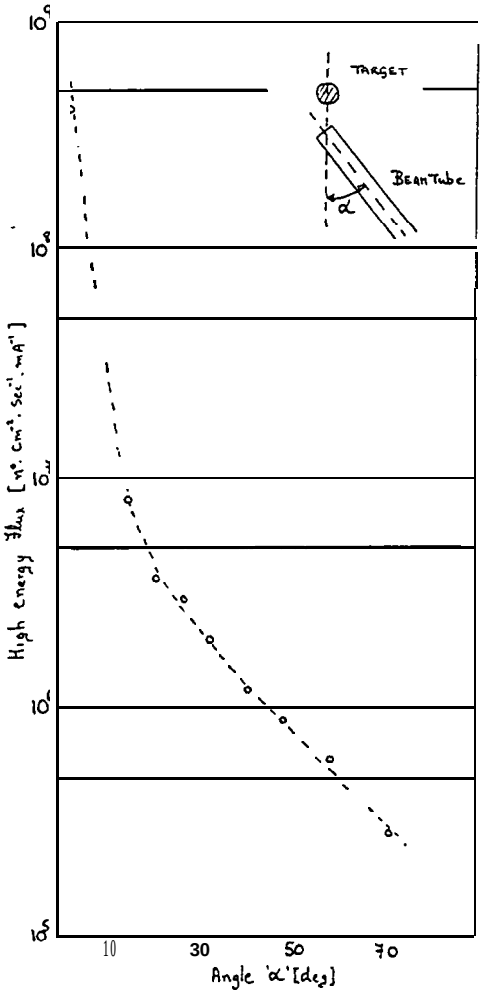

Figure 31: **The variation of the intensity of high-energy neutrons in a beam tube as a function of angle (see inset) to the target.**

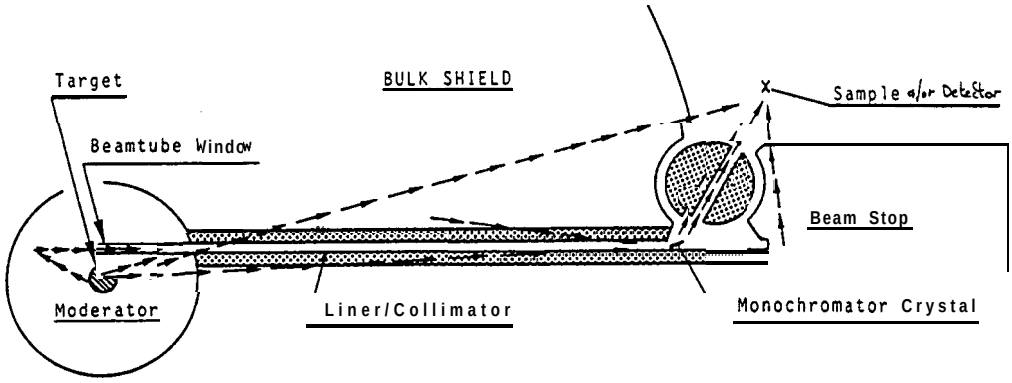

Figure 29: **The Potential sources of Background at SINQ**

The **difficult** part is the neutron-producing region, the design of which has to solve the problems of (i) how to do the cooling and (ii) how to contain the activation with a high enough safety margin and with the **minimum** degradation of **neutronic** performance. Coolant activation and the effect of activation on target handling depend somewhat on the design of the neutron production region and will be discussed below.

The best target material from a neutron production standpoint is **Pb** and this together with a D_2O moderator system will produce the highest useful neutron intensity for the users. The target material will need containment and other technical details that make the whole thing practicable. An essential part of target design is to minimise their degradation of performance, with the major concern being loss by absorption.

14 Target Neutronics

Over the past few years several target options have been examined. The **neutronic** calculation results are summarised in the following subsection.

14.1 Neutronic Performance of Various Target Systems

Calculations of the performance of six representative target systems have been made using HETC and 05 **R_PSI.O5R_PSI** uses cross-sections from **ENDF/B-**IV (Doppler broadened resonance unfolding was used for W and Ta) and the 'perfect-gas' approximation for treating the thermal region. The same model for the moderator system (without beam tubes) and proton beam parameters were used for all targets. A sketch of the moderator tank complex is shown in Fig. 33. The proton energy was 570 **MeV** and the transverse current density distribution came from beam transport calculations. An angular bias of 30 mrad is added to simulate the diverging away from the focus in the collimator below the target. The peak current density for 1 **mA** on target is 16.8 $\mu A/cm^2$.

The **neutronic** calculations are made in three parts:-

1. *High Energy Calculations* These start with the 570 **MeV** primary proton beam and follow all products till the cut-off energy (15 **MeV** for neutrons) is reached or the particle escapes the system. The fast neutrons produced are written to a file for use by **O5R_PSI.** Information for calculating energy deposition distributions is collected. Typically 20'000 protons were started.

2. Slowing *Down* In this part, the fast neutrons **are** followed to the iridium point (1.4 eV). This allows 'high-statistics' estimation of the energy deposition by the fast neutrons, the production of further neutrons and of the fast, intermediate and **epithermal** neutron escapes.

3. Thermal Fluxes: This part of the calculation uses a reduced number of batches from the fast neutron production of part 1 but follows them to the death (the calculation time per neutron is about a factor 40 higher than terminating at the iridium point). A 'perfect-gas' thermal scattering model is used for D_2O and H_2O and Russian roulette is played. Thermal fluxes are calculated using both path-length and collision-density estimators. Separate runs are made using 'randomly' selected fast neutron batches and the results merged.

The target systems which have been calculated are:-

(i) The original liquid **Pb-Bi** eutectic target [110].

(ii) A Tungsten plate target roughly following the design of G. **Heidenreich** [111]. As a refractory metal, this has engineering safety advantages.

(iii) A Tantalum plate target with an alternative water-cooling manifold. This is included as being the next 'normal' metal below Pb (Tungsten would most likely have to be in the form of a sintered material; its ability to withstand the radiation damage may be questioned).

(iv) A 'pebble-bed' target of Pb-buckshot as suggested by G. Heidenreich [70].

(v) A plate target built from zircalloy. Such a target system could provide a safe option for use on 'day 1'.

(vi) A liquid Pb target with zircalloy beam window and container. This would represent about the best we can do (it is not known if liquid Pb and Zircalloy are compatible so is treated as the best possible option).

The calculation results are summarised in Table-II which gives the gross energy partitioning through the inner layer components and other relevant information and Table-III which gives neutronic data. A map of the thermal neutron source and undisturbed thermal flux for the Pb target with a zircalloy container may be *seen* in Fig. 16 (left-hand curves). Comments on the results will be made below.

The calculated undisturbed thermal neutron flux for the Pb systems are consistent with an experimental measurement [112] of the neutron current in a beam tube for a model spallation source closely resembling SINQ. The measured value translates backwards to an undisturbed flux of 1.3. 10^{14} $n^o/cm^2/sec/mA$ which compares well with the value of 1.4. 10^{14} for the zircalloy container Pb target and with the value for the Pb-Bi target when the 37% loss due to the steel of the container and guide tube is removed (1.3 . 10^{14}).

14.2 A Best Target

Subject to the solution of various auxiliary problems, liquid Pb is the best target material:

- Pb is the highest mass element with a low thermal neutron absorption cross-section (Bi has a lower thermal neutron absorption cross-section but as absorption by Pb corresponds to about 4% of the neutron production, the problems of handling ^{210}Po and material compatabilit y outweigh the potential flux gain).

- The target material filling factor in the beam region can be close to 100Yo.

- It may be flowed and so used to transfer the heat away from the high particle flux region (i.e. there is no need to have a secondary cooling fluid in the beam region degrading the performance and becoming highly activated).

- As it is a liquid, mechanical property changes due to radiation damage are not particular y relevant.

The major difficulty is the selection of material(s) for the container, etc: not only must it satisfy 'mechanical' criteria but it also has to be neutronically acceptable (at least for the bottom 100 cm). There are comparatively few elements which have a low thermal neutron absorption cross-section:-

$\lesssim$ 10 mb	Be, C, O, F
$\lesssim$ 100 mb	He, Ne, Mg, (Bi)
$\lesssim$ 200 mb	Si, P, Zr, Pb
$\lesssim$ 500 mb	H, Al, Ca, Rb
$\lesssim$ 700 mb	Na, S, Ar, Ce, Sn
$\lesssim$ 1000 mb	
$\lesssim$ 2000 mb	N, Zn, Sr, Y, Nb, Ba
$\lesssim$ *3000* mb	K, Fe, Ga, Ge, Mo, Ru

Approximating the container wall as a 50 cm long and 20 cm diameter tube in an average thermal flux of 5.1013 /cm^2/see, the thermal neutron loss is roughly 0.2 /proton (some 2% of the production) for a 5 mm Al wall and 1.6 /proton (some 16% of the production) for 3 mm of Fe.

14.3 Alternative Targets

The first choice alternative design concept is the *Kugelbett* target. This has Pb-shot cooled by D_2O, with Al (or zircalloy) for the material of construction. It gives a neutron intensity a factor of 1.3 lower than for a 'good' liquid Pb target but as it has good heat transfer properties it can maintain the Pb in the solid state. There are several potential-problems/ undesirable-features:

(a) Corrosion/erosion of the Pb (corrosion enhancement by radiation)

(b) the rather low melting point of Pb (327.5^{o}C)

(c) high induced activation in the D_2O coolant

The high induced activation in the D_20 is mainly a shielding problem as short lived products are involved. The long half-life nuclides (mainly tritium) make it necessary to contain the circuit properly and to impose appropriate handling procedures during maintenance work.

The first two effectively lead to the need to consider how to handle rather large quantities of active Pb released into the external part of the cooling circuit (either regularly in the case of (a) or under fault conditions) or the cost of implementing a cooling system designed to handle it.

If the handling of such (real or potential) levels of activation is unacceptable then possible actions are:

(i) Clad the material. The choice of cladding material should be restricted to the low thermal neutron absorption cross-section elements. If such a choice

TABLE-II

Energy Distribution (MeV/p) in Inner Regions of SINQ with the various targets.

Component	Target System Pb-Bi	W-plate	Ta-Plate	Pb-shot	Pb	Zircalloy
Target Complex	444.43	458.76	439.50	428.02	440.69	423.03
Central Column	3.45	3.69	2.83	6.03	6.84	4.62
D_2O	54.07	40.18	37.70	57.23	50.07	53.58
D_2O Tank Wall	7.36	4.80	3.99	6.09	8.76	4.88
H_2O Layer	12.83	8.61	7.32	14.21	14.89	9.11
H_2O Tank Wall	0.10	0.07	0.10	0.09	0.09	0.10
TOTALS	522.24	516.11	491.44	513.67	521.35	495.32
Energy taken by H.E escapes (MeV)	15.9	21.4	16.0	23.0	16.1	30.0
Additional Terget Results						
n"/Interaction	6.33	5.64	5.60	5.68	6.53	-
Interactions/p	1.37	1.50	1.51	1.30	1.37	-
Maximum Energy Density (kcV/g)	31	31	34	37	28	43
1 y Activation (Decays/p)	1.8	3.4	-	1.6	-	0.9
Decay Energy (MeV/Decay)	1.1	0.55	-	0.67	-	1.3

Table-III

Neutronic Data and Neutron Balance

Component	Target System Pb-Bi	W-plate	Ta-Plate	Pb-shot	Pb	Zircalloy
Neutron Production						
(i) Target Complex	8.700	8.483	8.760	7.375	8.927	5.376
(ii) Moderator Complex	1.300	1.102	1.140	1.321	1.358	1.713
(iii) Fast Neutrons	0.455	0.453	0.560	0.336	0.582	0.259
TOTAL PRODUCTION	10.455	10.038	10.46	9.032	10.867	5.528
Neutron Loss						
(i) Fast/Epith. Escapes	0.078	0.055	0.053	0.063	0.060	0.037
(ii) Thermal Escapes	0.213	0.131	0.110	0.175	0.273	0.100
(iii) Absorption in:						
(a) Target Material	0.235	4.961	6.086	0.620	1.997	1.014
(b) Target Auxiliaries	2.983	0.472	0.510	0.449	-	
(c) Heavy Water + CC	1.092	0.766	0.609	1.330	1.584	0.769
(d) Light Water + TWS	5.800	3.645	3.105	6.358	6.872	3.593
TOTAL LOSS	10.401	10.030	10.473	8.995	10.786	5.513
Approx. Flux Maximum	9.1013	$8.\ 10^{13}$	$5.5.\ 10^{13}$	1.2.10'4	2.0.10'4	$8.\ 10^{13}$
Radius of flux *Ms.* (cm)	20	15	17.5	small	small	small
Max. Flux at 25cm radius	$8.5 \cdot 10^{13}$	$6.\ 10^{13}$	$4.5.\ 10^{13}$	1.1014	1.3.10'4	5.9.1013
Fluence/proton (Φ)	0.0136	0.00961	0.00721	0.00160	0.00215	0.00945
Φ/H_2O capture	0.00234	0.00264	0.00232	0.00252	0.00312	0.00263

1. The Pb-Bi target had a steel container and guide tube.
2. The W- & -Ta plate and Pb-shot targets had Al as material of construction.
3. The Pb target had a zircalloy container and guide-tube
4. The zircalloy target had only zircalloy!
5. The average fluence per proton per H_2O capture over all six target systems is 0.00261 $\pm$ 0.0003.

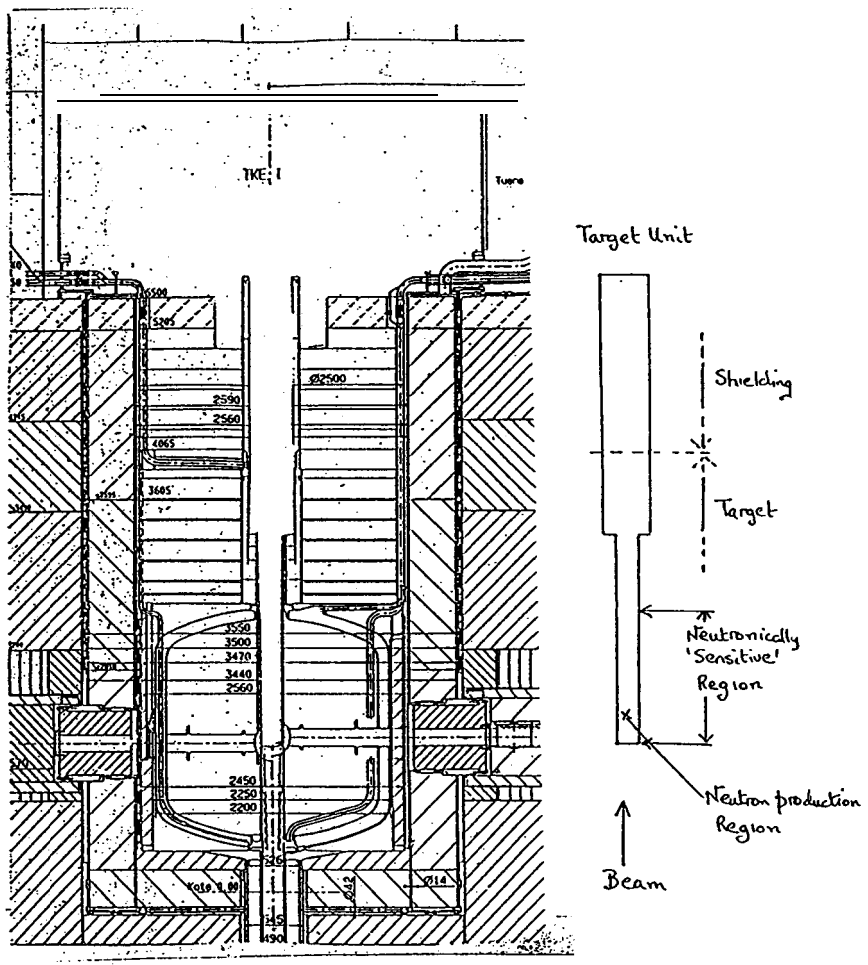

Figure 32: A vertical section through the target block in the region of the target. The target unit fits into the empty vertical shaft and extends to somewhere near the middle of the moderator tank.

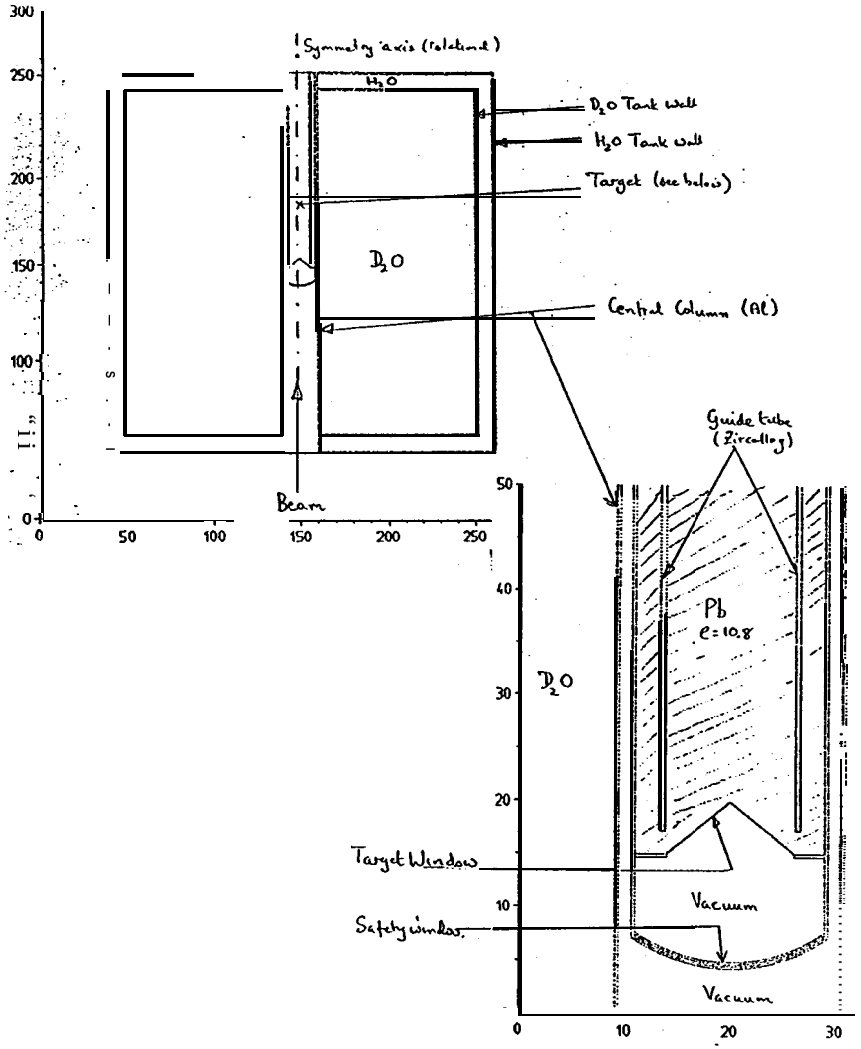

Figure 33: A sketch of the moderator tank system used for the thermal flux estimates.

is not practicable, then thermal neutron absorbtion will just reduce performance.
In general for the geometry of SINQ, the neutron flux $(n^o/cm^2/sec/mA)$ fits

$$\frac{1.04.\ 10^{14}}{1\ +\ 0.242\sigma_{abs}}$$

where σ_{abs} is the thermal neutron absorption cross-section (barns) for the target material.

(ii) Look for a Pb based alloy which has better properties (again, low absorption cross-section alloying elements).

(iii) Select a different material.

The selection of a different material for the *Kugelbett* (i.e. higher melting point, better corrosion properties) is not considered a good idea as, from a neutron production point of view, Pb is so far removed from its nearest rival that any alternative material would be better used in another geometry.

Some relevant physical and neutronic parameters for materials in the high atomic-mass region are given in Table-IV. Estimation of how some of them would perform in a *Kugelbett* geometry is set out in Table-V (Sn and Zr are added as being the next highest mass elements below Pb which have acceptable thermal neutron absorption cross-sections).

The dominance of absorption is clearly seen in the results of Table-V. The relatively poor primary neutron production with Sn and Zr is compensated by their weak absorption to make them better than W. Of the elements calculated in Table-V, Tl and Sn would be eliminated on ground of having a low melting point. This would only leave Pt as a contender from the heavy elements as Zircalloy would out-perform Re, W and Ta neutronically and also has a fairly high melting point.

If plate geometry targets are compared with the same material used in a *Kugelbett* geometry:-

	Flux at 25 cm (calculation)	Loss Factor as plate	Loss Factor as *Kugelbett*
W	*6.1013*	2.2	2.6
Ta	4.5.1013	2.9	4.3
Zr	5.9.1013	2.2	2.2
Pt	-	1.8 ?	2.0

We see that a rather better performance is obtained for the absorbing materials in a plate system (we ought to expect this if only on fill-factor grounds). The difference between the two forms for Zircalloy is very small giving the trend that the gain in moving from a *Kugelbett* to a plate system is larger the higher the absorption. From this trend, it is estimated that a Pt plate target would give useful thermal neutron intensities just under a factor of two lower than for an ideal Pb target.

15 System Performance Estimate Calculations

The following sections of this appendix give more details of system performance estimates (section 8) and includes some results.

16 Power Deposition

The calculated results of energy deposition through SINQ (with the old Pb-Bi target) are summarised in Table-VI which shows the distribution of energy in given components and by type of mechanism together with source strengths.

The power density as a function of radial distance from the target has been shown in Fig. 9: when given in terms of distance in $g \cdot cm^{-2}$ and with the solid angle factor removed, rather clearly shows the cutting in of contributions from the separate mechanisms and the propagation of the energy at large distances by the high-energy neutrons (the 120 g/cm^2 trend line will be met again in the section on shielding).

The nuclear heating contribution comes from analysis of the cascades from HETC calculations of the target and of a system consisting of a model of all components inside a 2 m radius, 4 m high cylinder centered on the target (roughly containing all the important source components plus the first metre of shielding). This part accounts for 86% of the power. In the target ionisation loss by the primary proton beam accounts for roughly 80% of the deposited energy.

16.1 Contribution from Gammas

The contribution of gammas has been made mainly using point kernel integrations: they only make significant contributions in regions where power densities are quite small (see Fig. 9). The main sources are target material activation, nuclear gammas (residual excitation), (high energy) gammas from π^o decay (mainly produced in the target) and capture gammas.

For the target, an EGS [23] calculation was used to estimate the energy remaining in the target and also to define a surface source for use in point-kernal integrations for the rest of the system. In the point-kernel integration the target is represented as an absorbing cylinder and the integration carried out over the generated surface source (varying in both position and energy). Parameter values (energy attenuation lengths and build-up factors) were taken from reference 72.

The treatment of capture gamma-rays in the D_20 , Al of the tank walls and H_20 layer was made by dividing the distributed source, as estimated from the captures calculated with 05 R-PSI, into a series of overlapping (gamma absorbing) cylinders, cylindrical annuli and disks with uniform volume source strengths and then superposing the results.

Table-IV

Some Physical and Neutronic Parameters for Various Elements.

Element	Pb	Tl	Hg	Au	Pt	Re	W	Ta	Sn	Zr
Z, A	82, 207.2	81,204.4	80,200.6	79, 197	78, 195	75, 186	74, 183.9	73,181	50, 119	40, 91
Density ρ (g.cm^{-3})	11.35	11.85	13.55	18.88	21.45	21.02	19.3	16.654	5.75	6.5
Thermal Absorption CX (b)	0.17	3.4	375	98.8	10.0	88	18.5	21.0	0.63	0.22
Thermal Scattering CX (b)	11.4	9.7	20	7.3	11.2	11.3	2.9	6.3		6.4
Resonate Integral (b)	0.16	12	73	1560	140	830	352	710	8.5	1.1
Nuclear Density (/Å^3)	0.033	0.035	0.041	0.058	0.066	0.068	0.063	0.055	0.029	0.043
Thermal Scattering Length (cm)	2.66	3.04	1.23	2.37	1.35	1.3	5.46	2.91		3.63
Thermal Absorption Length (cm)	178.3	8.42	0.066	0.175	1.51	0.017	0.86	0.86	55	122
590 MeV Range (cm)	25.6	24.4	21.0	15.0	13.4	13.4	14.6	17.0		
$\frac{dE}{dX}$ (MeV.cm^2/g)	1.37	1.37	1.39	1.40	1.39	1.41	1.40	1.40	1.4	1.4
T_{melt} "C	327.5	303.5	-38.87	1064.4	1772	3180	3410	2996	232	1840
T_{boil} "C	1740	1457	356.6	3080	3827	5627	5660	5425	2270	
Conductivity K (w/cm^2/K)	0.344	0.17 (?)	0.095	3.13	0.717	0.466	1.63	0.577	0.64	0.138
Expansion α x 10^6	29	?		14.2	9	?	4.5	6.5	20	5.2

Table-V

Neutronic Performance Estimate for Several Materials.

Element	$n^o/p^{(1)}$	$n^o/p^{(2)}$	SDL/p(3)	Abs/p(4)	$n^o/p^{(5)}$	Flux(6)	LF(7)
Pb	**9.23**	*9.04*	0.001	0.625	**8.414**	9.8.1013	1.3
Tl	**9.12**	*8.96*	0.084	2.310	**6.57**	7.6.1013	1.7
Pt	**8.78**	*8.68*	0.944	2.170	**5.57**	$6.5 \cdot 10^{13}$	2.0
Re	**8.44**	*8.41*	5.37	0.97	**2.07**	2.401013	5.5
w	**8.36**	*8.35*	2.26	1.77	**4.32**	5.0.1013	2.6
Ta	**8.26**	*8.27*	4.50	1.11	**2.66**	3.1.1013	4.3
Sn	**5.69**	*6.21*	0.027	1.02	**5.16**	$6.0 \cdot 10^{13}$	2.2
Zr	**4.69**	*5.41*	0.004	0.46	**4.95**	5.8.1013	2.2

Notes:

1) Neutron Production per proton from Fraser et al.

$$\approx \frac{1}{12610}(A + 40.5)(E - 120)\ n^o/p,\ E\ in\ MeV$$

(2) From Pb *Kugelbett* calculation, 80% of production under (1) plus 1.66 n^o/p from production external to target.

(3) Loss during slowing down. Calculation with W and Ta targets suggest a factor 0.0007. I_∞ . **0.8.** $n^o/p^{(1)}$.

(4) **Absorption** by target = $[n^o/p^{(2)}$ - SDL] . $f(\sigma_{th})$. $f(\sigma_{th})$ comes from absorption study.

(5) no/p effective for useful flux generation
= $n^o/p^{(2)}$ - SDL - Abs

(6) $n^o/p^{(5)}$ x 0.76 x 1.5301013 to give flux at 25 cm (from target study).

(7) Loss factor = 13.1013 / (Calculated Flux).

Table-VI

The gross distribution of energy in the inner regions of SINQ.
System of Moderator with Pb-Bi Target with steel container and 570 MeV Protons.
All values in units of MeV/Proton

Component	Gamma Sources		Deposited Energy			
	$E^* + \pi^o$	Capture	Gamma	High Energy	Fast Neutron	Total
Pb-Bi	11	1.6	24	370	11	406
Guide Tube	0.6	8.0	0.44	15	1.3	16
Vessel Wall	01.	10	0.92	1.4	0.63	3.0
Cooling Jacket	0.02	1.7		0.29	0.11	0.4
Window Complex	0.8	0.4		9.1	0.16	9.3
Central Column	0.03	2.4	0.42	0.33	0.57	1.3
D_2O	2,0	5.2	23	24	23	69
D_2O Tank Wall	0.04	6.2	1.8	0.21	0.03	2.1
H_2O Shield	0.1	11	5.5	1.0	0.16	6.7
H_2O Tank Wall	0.01		0.79	0.09		0.88
Shielding	3,2	9.4	18	9.3	3.5	31
Totals	18	57	75	430	40	550

Table-VII

The Dispersion of Gamma Energy in the Inner Regions of SINQ.
All values are given in MeV per 570 MeV proton incident on the target,

Source	Strength	Target System	Target Wall	Central Column	D_2O	D_2O Tank wall	H_2O	H_2O Tank wall	Shield
Pb-Bi + Guide-tube	21.4	16.85	0.7	0.15	3.56	0.03	0.09	0.02	
Target Wall + C.C.	15.6	7.42	0.21	0.25	6.04	0.06	0.18	0.04	1.4
D_2O	7.24	0.36	0.01	0.01	5.95	0.15	0.42	0.08	0.26
H_2O + Tank Walls	17.86	0.11		0.01	6.84	1.49	4.46	0.60	4.35
Shielding	12.6				0.11	0.11	0.36	0.05	11.97
Totals	74.7	24.74	0.92	0.42	22.5	1.84	5.51	0.79	17.98

The contribution of thermal neutrons to heating in the inner shield layer comes from the (approximately 7 MeV) capture gammas. This was treated using the results for the H_20 layer estimates (see section 12) and using a broad beam attenuation of the capture gamma spectrum [114]. The H_20 layer was included into the design of the moderator tank to bring about a large reduction of thermal flux; without this layer power densities would be dominated by the thermal neutron cap tures.

The results for the distribution of the gamma ray energy are summarised in Table-VII.

17 Parameter Values for Shielding Estimates

The source to be shielded is the neutron production target. The high-energy neutron production is limited to about a 25 cm length, 10 cm radius cylinder and for general bulk shield performance considerations it is adequate to consider this to be a point.

The formula requires values for the source spectrum, build-up factors, flux-to-dose conversion factors and for the shielding lengths.

17.1 The Particle Source Term

The source spectrum affects the estimation of shield performance, directly by providing the strength term, and indirectly through the energy dependence of flux-to-dose factors, build-up factors and shielding lengths. The estimates have to rely on theoretically predicted neutron spectra: in the first instance, these have been calculated with the HETC [17] programme but to allow for possible underestimates of spectral distributions by HETC (see Fig. 34 and section 5) they have been adjusted based on the work of Pearlstein [115]. This also gives a convenient mathematical representation of the spectra for use in the computer code.

Except for forward angles, where shadowing by the thick target and hence multiple interactions will have a significant effect, neutron escape spectra do not vary too much between 'thin" and 'thick" targets (see 90° thick target data compared to the "thin" of Pearlstein's correlation in Fig. 34): there will be about a 30% contribution from multiple scatters at 90°, The measured double-differential spectra for thin target (p,xn) reactions for Al, Fe and Pb have been fitted [115] to a four-component evaporation spectrum with a 'global' set of parameters:

$$\frac{d^2\sigma}{dE\,d\omega} = \sum_{n=1}^{4} a_n(\mu) E \exp^{-\frac{E}{T_n(\mu)}}$$

where $a_n(\mu)$ and T'(p) are second order Legendre polynomial expansions in the cosine of the scattering angle (μ) and the coefficients vary systematically with mass of the struck nucleus and energy of the incident proton.

The predicated [1] total neutron production in the region 15 to 590 MeV and 40° to 180° has been scaled to match the HETC prediction in the same energy and angular ranges (it is safer to normalise on the particle intensity rather than energy). The resulting normalised angular distributions for intensity, energy-flux, average energy and unshielded dose are shown in Fig. 35. The large discrepancies at forward angles come from the difference between thin and thick targets: when using this modified spectrum, the target material needs to be included but only as part of the shielding. The neutron angular intensity distribution for several systems that have been used in shielding estimates are shown in Fig. 36. In general, the difference between them is small.

17.2 Build-up factor

The build-up factor relates the dose calculated using an exponential thickness dependence to the 'true' external dose, It takes into account three, somewhat related, effects: (i) the multiplicity of high-energy interactions, (ii) these created particles are produced inside the shielding (and hence 'see' less shielding material) and (iii) the external dose is an integral over all escaping particles (e.g. thermal and epithermal neutrons, capture gammas, etc). It is convenient to consider it as two separate terms.

The geometric effects, (i) and (ii) above, have been estimated from the results of calculations [64, 122] examining the shielding 'effect' of iron. The results are shown in Fig. 37.

The second term to be incorporated into the build-up factor, corrects for the energy cut-off (15 MeV) employed in the calculations used for the geometric factor estimates (that is, the contribution of the neutrons below 15 MeV and capture gammas are not included). The tabulated spectral contributions to the dose [60] for the case where iron is followed by a 20 cm thick layer of berated concrete shows that 59% of the dose comes from neutrons above 10 MeV and 48% from those above 30 MeV. This shows that the calculations only account for 5070 of the dose and hence a further factor of 2.0 is required.

The value for this factor will depend on the exact shielding situation: in the case of an iron shield without concrete, the results of Uwamino suggest a factor of 27 is required (this comes from the high epithermal fluxes from the poor shielding characteristics of iron in this energy range - see Fig. 13).

Attenuation Fact ors

A selection of values of attenuation factors for iron

[1] The values for 150° scattering by lead quoted in reference 115 were recalculated based on the data of Cierjacks et al. (as quoted in reference 117) to be 8.2 $\mu b/sr.MeV^2$ and 62.5 MeV.

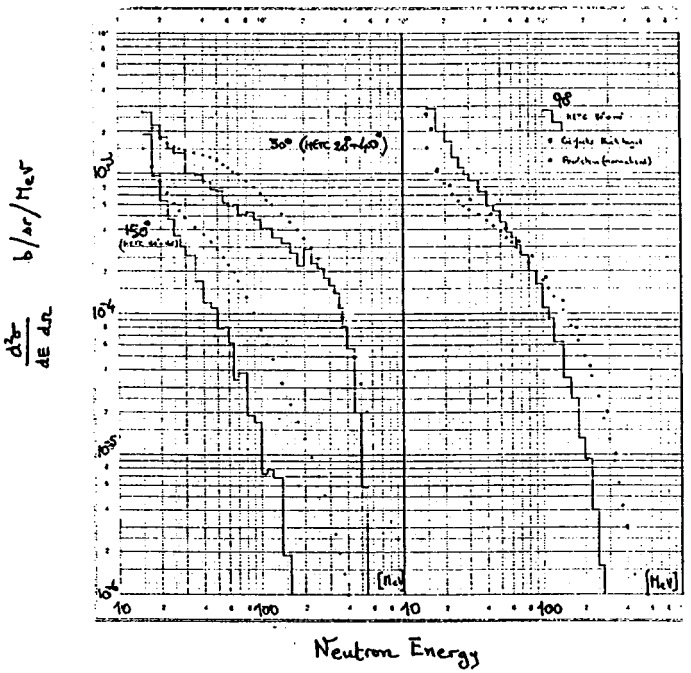

Figure 34: Double differential cross-sections for neutron production by 590 MeV protons on a thick Pb-Bi target (i) as calculated with HETC, (ii) from the measurement of Cierjacks et al. [116] and (iii) from the Pearlstein data [115] fit.

Note: The discrepency between HETC and measurement is rather less with more recent experimental results [41]

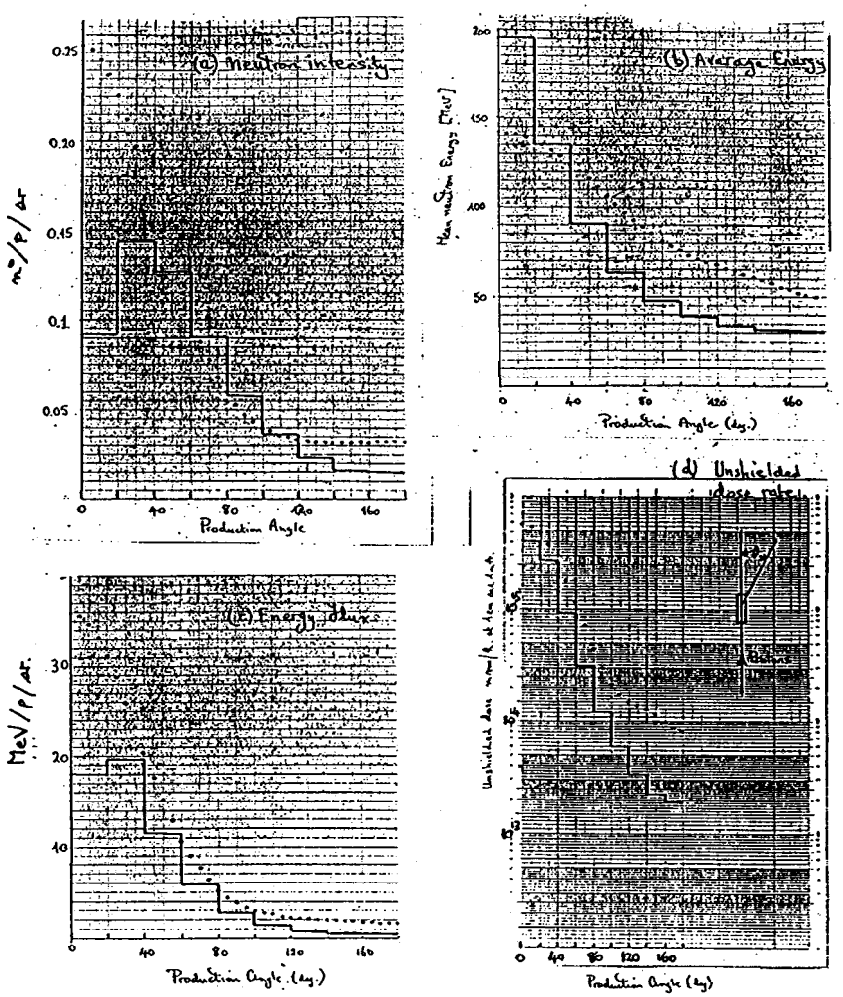

Figure 35: Comparison of HETC results (histograms) for neutron production in the energy range 15 to 590 MeV as a function of angle with those for the adjusted Pearlstein spectra.
(a) integrated neutron intensity (n°/proton/sr)
(b) average neutron energy (MeV)
(c) integrated energy flux (MeV/proton/sr)
(d) unshielded dose (mrem/h/mA at 1 cm distance)

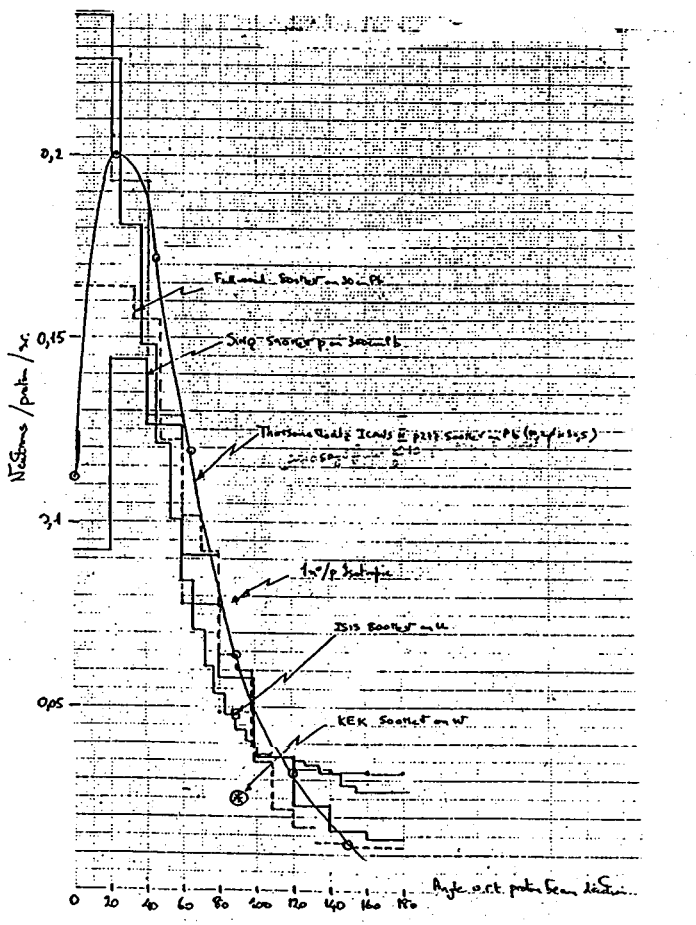

Figure 36: **The intensity distribution for high-energy neutrons around thick targets: (i) HETC for SINQ [118], (ii) Adjusted spectrum used in the calculations for the SINQ shielding, (iii) from the calculation of Fullwood et al. [33], (iv) from the measurements of Thorson and Moritz [119] (v) Spot values at 900 (a) corresponding to 1 π^o/p with an isotropic distribution, (b) 800 MeV protons on a uranium target as used for the ISIS shielding estimates [120] and (c) 500 MeV protons on a tungsten target as used for the KENS estimate [121].**

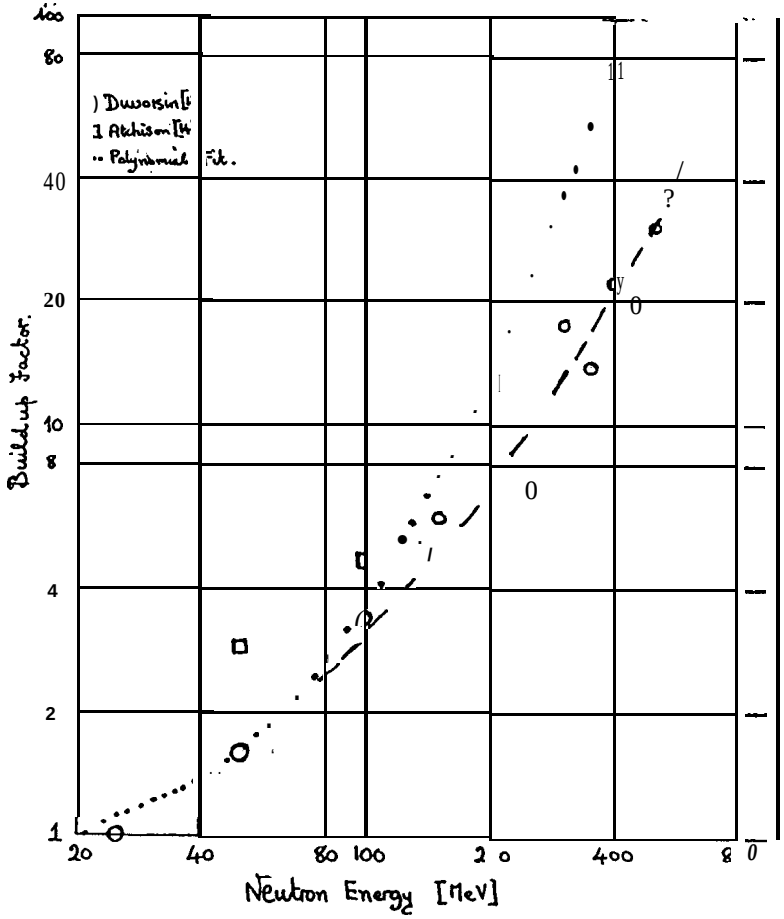

Figure 37: Geometric contribution to build-up for neutrons as a function of incident energy (from Monte-carlo calulations [64,122]) together with results of the approximate polynomial representation.

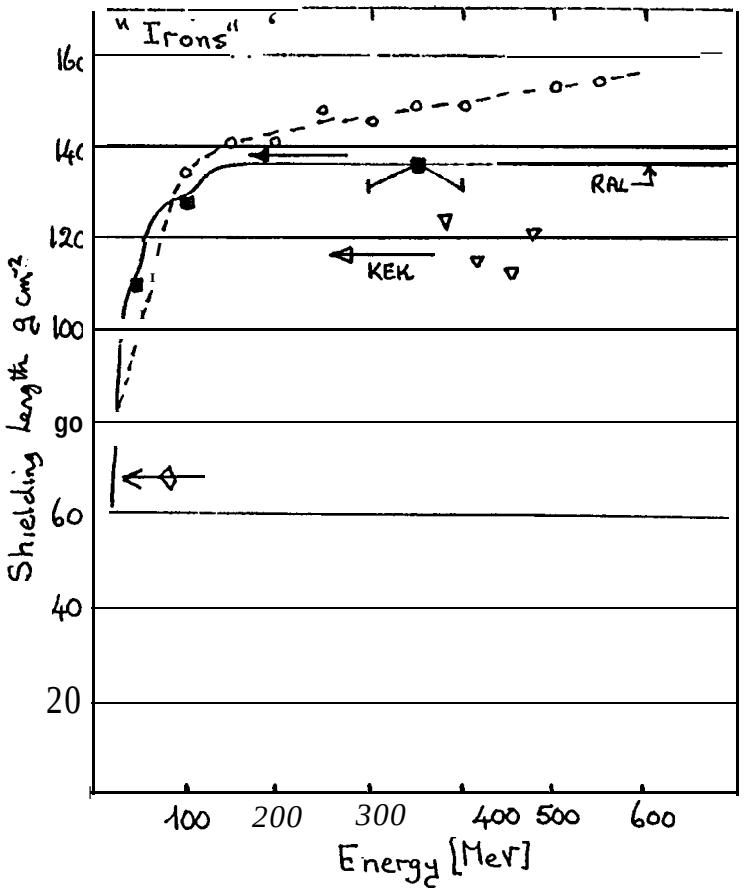

Figure 38: Attenuation Factors (g. cm^{-2}) for iron from various sources as used in calculations or as calculated. The results come from: (——) [124], (··o··) [64], (+) [63], (◁◇) [125], (+) [121], and (■) [122].
For reference purposes, the total inelastic cross-sections for iron [65] are also shown.

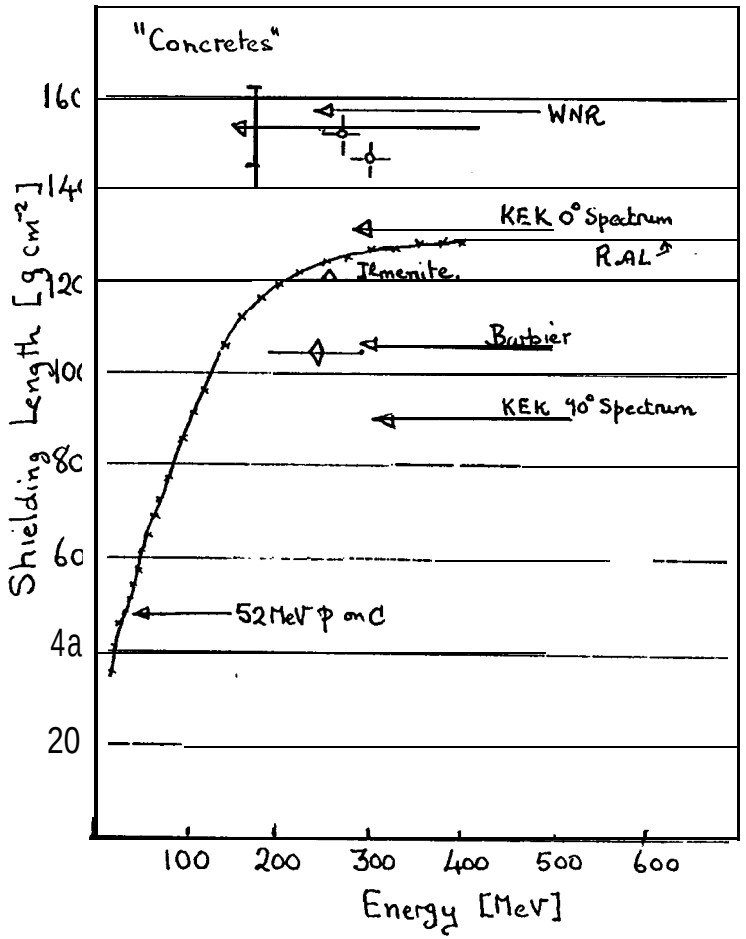

Figure 39: Attenuation Factors ($g.cm^{-2}$) for concrete from various sources as used in calculations or as calculated. The results come from: (×-×-×) [124], (+) [54], (-◇-) [72], (◁◇) [125], and (◁—) [121]

and concrete are shown in Fig. 38 and Fig. 39. The data show a considerable spread in actual value but do agree on a small variation for high-energy neutrons (energy greater than about 100 MeV). The main spread of values comes from the various concretes and is partly due to the composition variation. The basic shielding mechanism is to inelastically scatter the neutrons and hence there should be a $A^{\frac{1}{3}}$ (or $A^{\frac{1}{4}}$ [123]) dependence on the mass of the nuclei.

Iron and concrete have roughly the same mass attenuation lengths for high energy neutrons: the superiority of iron comes from its greater density giving a factor of about 3 less thickness. It is important to note that such values only give the high-energy neutron attenuation and should be used in conjunction with dose build-up factors appropriate to the shielding situation.

The values of Broome [124] for both iron and concrete have been used.

17.3 Smearing Function Estimate

In using the exponential model in a straight-ahead point-kernel mode, localised inhomogeneities will show up numerically rather clearly. The spreading of the high-energy cascade and of the neutrons during slowing down mean that the distribution will be smeared. The smearing is carried out by convolution of appropriate calculated dose distributions with a radially symmetric gaussian function. This is selected on the grounds of simplicity and also having a transparent effect on the results.

Taking the approximation for the forward current distribution in the high-energy cascade as shown in Fig. 12, the radial distribution at some escape plane may be explicitly calculated and then used to estimate standard deviations as a function of thickness:

Thickness (cm)	100	200	300	400	500
$< \sigma >$ (cm)	14	26	41	60	83

The convolution is carried out using a discrete Fourier transform of 'complete' 2-dimensional dose distributions (i.e. these are taken to represent a complete period) and zero framed to avoid pollution.

17.4 Comparison with Results for Shielding at Other Facilities

It is difficult to ascertain a realistic uncertainty in absolute terms for the parameter values (as distinct to the effect of uncertainties on calculated values) so some brief details of the shielding and its performance estimation for other neutron sources are given together with (where appropriate) an estimate of external dose rate as calculated using SINQ parameters:-

1. Shielding lengths for iron and concrete of 134 and 121 $g \cdot cm^{-2}$ at 90°.
2. A source strength (at 90°) corresponding to 3. 10^{14} mrem/h at 1 cm distance and 1 mA proton current. This includes the build-up factor.

In the main, these are all working facilities which implies that the shielding satisfies local dose-rate criteria.

KENS Reference 121

1.5 μA of 500 MeV protons on 12 cm long, 7.8 x 5.7 cm^2 tungsten target (target and proton beam horizontal).
Dose to be less than 1 mrem/h at shield surface.
Top shielding 165 cm Fe + 80 cm heavy (3.35 g/cm^3) concrete.
Side shielding 125 cm Fe + 240 cm heavy (3.35 g/cm^3) concrete.
Design basis of 3 neutrons/(cm^2.see) for 1 mrem/h.
Unshielded dose 8.2.10-10 rem/h m^2 per proton/sec on target.
No build-up factor used.

ISIS Reference 120 and 126.

200 μA of 800 MeV protons onto a 30 cm uranium target (target and proton beam horizontal).
External dose to be less than 0,05 mrem/h at 6.5 m from the target at 90°.
Path from source at 90°: 160 cm void + 330 cm iron + 100 cm concrete (2.3 $g \cdot cm^{-3}$) and the outer 25 cm of concrete 1% boron loaded. (Note: the shielding is strengthened by use of blocks at more forward angles).
Calculated using attenuation lengths of 17.3 and 56 cm for iron and concrete and no build-up factor.
Source strength taken as for 'bare' target hence effect of moderator neglected.
The shielding as built satisfies the dose specification (Note: where iron does not have a concrete skin it does not meet the specification).

1 *Using SINQ parameters, the dose at 6.5 m is predicted to be 0.08 mrem/h (about a factor of 2.0 higher than ISIS calculation).*

WNR Reference 127

20 μA of *800* MeV protons onto tungsten (vertical target with beam from above).
Path from source: 90 cm void + 280 cm iron and 60 cm heavy (magnetite) concrete as a sandwich + 30 cm boron loaded magnetite concrete.
Design aim: an external dose rate of less than 1 mrem/h.
Used attenuation length of 20.2 cm for the sandwich (calculated and measured values [128]) and NMTC-MCN[2] calculations.
Measurement by foil activation through an iron

[2] MCN was an early fast-neutron transport code used at Los Alamos

plug inserted into this shield gave an attenuation of 19.6 cm [54]

2. *Taking a density for the magnetite concrete of 3.4 g·cm^{-3} and using scaled SINQ source strength and shielding parameters gives an external dose rate of 0.25 mrem/h which compares well with 0.2 mrem/h at 20 μA from Fig. 6 of reference 127 (value at beam-line height and depth of 15').*

LANSCE Reference 129

This is an upgrade of the WNR facility (see above).
30 cm iron mounted in the void vessel plus the effect of part of a 30 cm thick Ni reflector around the target to upgrade the WNR shield for operation at 200 μamps.

3. *These dimensions are not inconsistent with a factor 10 improvement of the shielding attenuation when SINQ parameters are used.*

17.5 Skyshine

Skyshine is an important consideration for the dose at large distances from the facility (for instance outside the controlled area and in areas occupied by the public). Neutron doses on the over-source shielding can be higher as the area is not normally occupied. Part of the neutron current escaping (i.e. integrated over the total surface area) will be reflected back from the atmosphere to contribute to the dose-rate at large distances. The shielding has to be thick enough that radiological requirements are satisfied. Estimates for SINQ have been based on work in reference 130.

Measurements summarised in reference 130 (see Fig. 40) lead to an empirical relationship for the variation of dose with distance given by:-

$$\Phi(r) = \frac{Q}{4\pi r^2} exp^{-\frac{r}{\lambda}}$$

where r is the distance from the source of strength Q and λ is the effective absorption length (this is about *650* m for the SINQ escape spectrum - see Fig. 41). The source term is approximated by a 620 cm radius disk with 25 n^o/cm^2 /see and a dose conversion factor of 3. 10^{-}13 rem.m^2 per neutron as suggested in reference 130.

The data displayed in Fig. 40 suggests a variation of the contribution at distances less than R given by:-

$$\Phi'(r) = \frac{R^2\Phi(R)}{r^2} exp^{+\frac{r}{R}}$$

with R of the order of 100 m and Φ(R) as given above. Such a form is not valid for estimation of the contribution within the building where the roof of the building will make a large contribution.

The dose variation at large distances will also contain a contribution from leakage from the side-shielding.

18 Activation Estimates

More details for activation estimates are given in the following subsections.

18.1 Inner Region Activation

For the target and moderator system, activation estimates come from nuclide production rates as calculated by the HETC package. The calculations are straightforward and give the required information for the 'hazard' rating of the target, for the shield design of the transport flask and for nuclide production rates in circulating coolant. The nuclide production by high energy particles is spread over a wide mass range. This led to the need to extensively enlarge the nuclide-data library for ORIHET.

18.2 Induced Activation Dose Rates in Accessible Caverns

The principal caverns are for access to (i) the top of the target (ii) the top of the proton beam channel and (iii) the vertical section of the D_2-cold neutron source. The aim is to allow hands-on maintainance in these regions when beam is switched off. A vertical section showing some of these may be seen in Fig. 4.

The activation dose rates depend on the neutron intensit y and energy spectrum and also on the materials. All of these are only rather poorly known and hence rather simple but clear calculational methods are employed. The basis of the estimate is as follows:

- the energy distribution of the neutrons irradiating the region is the equilibrium spectrum of the shielding material in the vicinity.
- the shape of high-energy neutron part of the spectrum is not dependent on the shielding material.

Induced activation in steel by 'typical' shield spectra have been estimated on the basis of the work of Barbier [131] and the results may be summarised in terms of a dose ratio: that is, the surface dose rate from the activation divided by the direct dose of the incident neutron spectrum.

- Iron + boron loaded concrete (thermal neutron suppressed spectrum): 2.0 .10-4 x the irradiating dose after 1 hour cooldown and 1.0 .10-4 after 50 hours.
- Iron + normal concrete: 1.1 .10-3 of the irradiating dose after 1 hour cool down and 3 .10-4 after 50 hours.

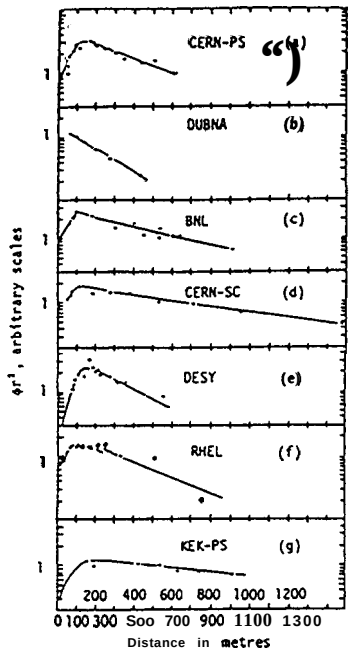

Measurements performed around different accelerators. On the abscissa isthe distance from the accelerator in metres, on the ordinateis the product of the measured neutron-flux density and the square of the distance. In these coordinates, a $1/r^2$ variation is represented by a horizontal line. (a) Measurements of fast neutron-flux density performed at the CERN 28-GeV Proton Synchrotrons (0164). (b) Measurements of fast neutron-flux density performed at the Dubna 10 GV Proton Synchrophasotron (Ko70; Le65). (C) Measurements of dose-equivalent rate performed at the Brookhaven 30-GeV proton *AGS* (Di66). (d) Measurements of the fast neutron-dux density performed at the CERN 600-MeV Proton Synchrocyclotron (Ri63). (.) Fast neutron-flux density measurements pet-formed at the DESY 7.5-GeV Electron Synchrotrons (Ba67). (f) Fart neutron-flux density measurements performed at the Rutherford Laboratory Proton Linear Accelerator. The solid dots indicate the measurements taken for a proton beam of 30 MeV (Th62), and the open dots for a proton beam of 93 MeV (Si62). (g) Measurements made at the12-GeV Proton Synchrotrons • t KEK (Ka78).

Figure 40: [Taken from reference 130]

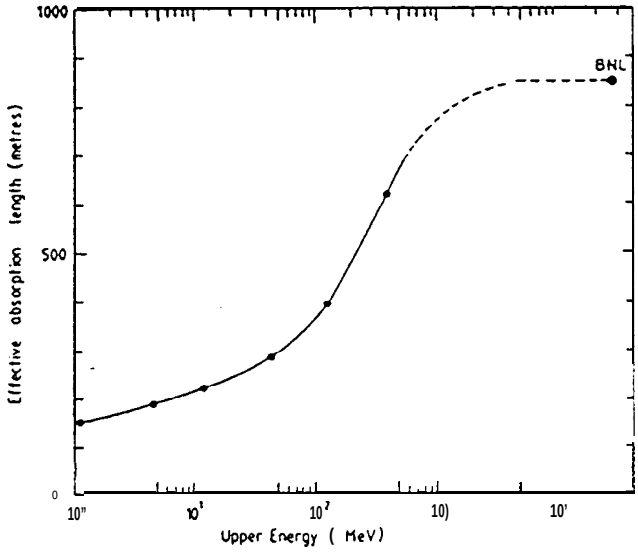

Figure 41: Effective absorption length as a function of upper neutron energy for l/E spectra [Taken from reference 130].

- Iron (without concrete): 4 .10-4 after 1 hour and 2010-4 after 50 hour cooldown.

These estimates may be combined with dose rates as calculated for the shielding to give activation dose-rates.

18.3 Ground Activation

The estimates are based on similar assumptions to those used for induced activation dose-rate estimations. In this case, the calculation of Janett [132] show that a current of 1000 high-energy neutrons/cm^2 /see irradiating soil induces activation of 1 Bq/g.

The Uwamino spectrum [60] for a calculated dose of 1 $\mu Sv/h$ has a high-energy neutron current component of 0.34/cm^2/sec.

Combining these two values gives that a calculated dose rate of 2.9 mSv/h at a concrete/ground interface corresponds to a high-energy neutron intensity of 1000/cm^2/sec and hence leads to induced activation of 1 Bq/g.

18.4 Active Material in the Bulk Shield

The bulk shield is a roughly 5 m thick layer of iron with a 'skin' of concrete outside. This is a very large volume of material and haa been treated by the following technique,

The interactions giving the shielding process (see section 8.2.2) lead to the production of activation, which means that a very broad range of neutron energies (from several hundred MeV down to thermal) cause the actual nuclide production. This energy spectrum is being generated within the medium itself (i) a high-energy 'out-going' current which is a mixture of the uncollided spectrum from the target and of the (mainly forward) secondaries and (ii) a slowing down spectrum from the fast neutrons produced in spallation reactions. The shape of the spectrum will be rather stable (section 8.2.2). This means the integrated intensity will follow the approximately 120 g/cm^2 attenuation length exponential from the shielding calculations and the production rates may be estimated for the 'equilibrium' spectrum.

The specific activation level for a given nuclide due to a neutron flux/current $I(E)$ irradiating the material for a period t_{irr} and after a decay period of t_{dec} is given by

$$N(1-\exp^{-\lambda t_{irr}})\exp^{-\lambda t_{dec}}\int dE\{I(E).\sigma(E)\}$$

where λ is the decay constant for the nuclide, $u(E)$ the production cross-section and N the nuclear density.

Cross-section values vary (with energy and target nu-

cleus) over many orders of magnitude as do the decay modes (radiation type and energy, half-life etc.). This leads to the situation where rather small quantities of particular elements (Co, Eu) significantly contribute or dominate the activation. The activation after specific decay times is normally dominated by one or two nuclides - those that optimally combine cross-section, half-life and a strong decay-mode.

18.4.1 Nuclide Production by High-Energy Neutrons

The interaction cross-section and branching ratios to specific channels vary rather slowly with target mass (e.g. there is none of the dramatic variation typical of the intermediate energy region). The interaction cross-section is also a slowly varying function of incident particle's energy. The relevant factor for activation estimates is the wide charge-mass range of the products and the width increases as the incident particle energy rises as more end states become energetically possible. Also there will be no interference between members of the mixture.

18.4.2 Fast and Intermediate Energy Region

These regions are taken together as the formulism used is the same. For a heavy absorbing moderating medium, the production rate for a specific channel with a (macroscopic) cross-section Σ_c is given by an expression of the form

$$P_c = \sum_m \frac{\Sigma_c(m\xi)}{\Sigma_t(m\xi)} \prod_{n=0}^{m-1} \left[1 - \frac{\Sigma_a(m\xi)}{\Sigma_t(m\xi)}\right] \qquad (1)$$

where the equation is in terms of lethargy units with lethargy zero taken as the incident particle's energy, Σ_a and Σ_t are the total neutron loss and total interaction cross-sections respectively and ξ is the lethargy gain per collision. This expresses that the interaction rate will be the sum over all collisions but with the rate at any particular lethargy reduced by the probability that the neutron reaches it.

The fast neutron region is taken to be from 0.1 to 20 MeV and the intermediate from 0.1 MeV to 0.1 eV. The break between the regions is chosen aa being the point where (i) direct neutron production (via spallation) makes a small contribution, (ii) inelastic producion channels have mainly died out and (iii) absorption is not particularly strong.

The fast neutron part of the spectrum comes mainly from direct production by spallation reactions. The calculated spectrum of Uwamino [60] in the fast region is broken into five energy sub-groups and the production estimated from equation 1 using cross-sections from ENDF/B-IV [19].

For intermediate energy neutrons, infinite dilution resonance integrals are used in the first instance. These arise directly from equation 1 by dropping the absorption term and converting the sum to an integral (133]. The major problem is that components of the mixture can interfere.

As an example absorption in iron containing 420 ppm caesium and 160 ppm cobalt have been estimated from equation 1 using ENDF/B-IV cross-sections, starting with neutrons of energy 0.1 MeV and following down to 0.1 eV. The calculation was checked by simultaneously generating resonance integrals and results are shown in the following table:

Element	Fe	Cs	co
I_∞(calc) [b]	*2.85*	*397*	*97.7*
I_∞(BNL[1]) [b]	2.82	431	98.4
I_{eff} [b]	0.36	80.1	25.2
Absorption /0.1 MeV *no*	*0.902*	*0.0876*	*0.0093*

(1) The $\frac{1}{v}$ contribution from 0.1 to 0.5 eV has been added to the BNL-325 [65] results.

That is, the neutron loss in the iron (and caesium) during slowing down is screening the loss at the low energy end of the band. As more than 50% of the resonance integral for iron comes from the $\frac{1}{v}$ tail, the use of an average flux per unit lethargy in combination with the resonance integral is overestimating the production.

Cross-section information from BNL-325 [65] can be used to estimate production rates rates from thermal neutrons.

18.5 Activation in Water Cooling Circuits

There are four main regions of SINQ that require forced 'water' cooling of components in 'high' radiation fields: target and collimator, D_20 -moderator, H_20 -shield and the inner shield layers. The coolant itself (D_2O or H_20) will be directly activated as will any impurities (e.g. corrosion products from anywhere in the circuit). In addition, any corrosion in the cooled regions will be from activated material and will be accompanied by products recoiling directly from the surface into the coolant. The activation will be carried round the circuit and into the plant room. The calculation of such indirect contributions will not be discussed.

The activation of water coolant comes from spallation, fast, epithermal and thermal neutron interaction products of oxygen and (in the case of heavy-water) from thermal-neutron capture by deuterium. Nuclide production rate estimates come from HETC package calculations for the inner region of SINQ.

The build-up of activation in circulating coolant will depend on the flow parameters of the circuit: for an irradiation volume V in which the coolant is irradiated

for a time t_{irr}, a coolant circulation time of t_{circ} and a total time in operation $T (= N \cdot t_{circ})$, the specific activation at the *end* of the irradiation volume is given by:-

$$\mathcal{I} = \sum_i \mathcal{J}_i = \sum_i \frac{\alpha_i}{V} \cdot \frac{(1 - \exp^{-\tau_i t_{irr}})(1 - \exp^{-\tau_i T})}{(1 - \exp^{-\tau_i t_{circ}})}$$

where α_i is the equilibrium activation and τ_i the decay constant for nuclide i (in the one or two cases where there is a decay chain, this expression needs an obvious modification to treat the daughters). The specific activation at some position with a time-delay from the end of the irradiation volume of t_{dec} is given by:-

$$\mathcal{I}' = \sum_i \mathcal{J}_i \cdot \exp^{-\tau_i t_{dec}}$$

For very short half-life nuclides, equilibrium is reached in one passage through the irradiation volume. For very long half-life products, the equilibrium specific activation is reduced by the obvious factor $\frac{t_{irr}}{t_{circ}}$.

18.5.1 Short Half-life Activation

The pipe runs will approximate to long line sources with strength per unit length given by the cross-section and the specific activation. The specific activation varies with distance from the irradiation zone: the ages of the nuclide mixtures are given by the flow rates. To give a feel for the orders of magnitude involved, 'long-pipe' doses for a 1 m distance from the pipe of the order of 100 to 200 rem/h have been calculated for water irradiated in the Pb-shot target at 1 mA. The activation is quite short lived and decays to negligible levels in a couple of hours. The persistent component is 20.38 m ^{11}C with significant contributions at intermediate times from 9.96 m ^{13}N. Both these are β^+ emitters so that the main contribution to the gamma dose comes from annihilation radiation and the dose rates outside shielding will drop more rapidly.

There will also be some neutron dose caused by 4.17 sec ^{17}N and 0.75 sec ^{16}C.

Shielding Considerations.

The external gamma dose through the concrete walls of the plant room mainly comes from the 6.13 MeV gammas from 7.2 sec ^{16}N and the 2.3 MeV gammas from 7059 sec ^{14}O; the rest of the source dose comes from 0.5 MeV annihilation gammas (these have a factor of about 50 greater attenuation by 1 m of concrete). The dose attenuation coefficients [72] for normal concrete for ^{16}N γ's is 6 m^{-1}, for ^{14}O 8 m^{-1} and 0.5 MeV annihilation radiation 12 m^{-1}.

The dose rate at a perpendicular distance S and distance Z from the start of a line source consisting of a nuclide with decay constant τ and outside a shield wall having D attenuation lengths (perpendicular to the line source) for the gammas is given by:

$$\frac{Q}{S^2} \int_0^{Z_{max}} dw \left\{ \frac{\exp^{-\frac{w}{vT} - D\sqrt{1.0 + \frac{(Z-w)^2}{S^2}}}}{(1 + \frac{(Z-w)^2}{S^2})} \right. \quad \text{I}$$

where v is the flow velocity and Q is the unshielded gamma dose at unit distance from the activation in the pipe at the start (Z = O).

18.5.2 Long Half-life Nuclides

The long half-life nuclides are 12.3 year ^3H, 53.29 day ^7Be, 1.6.106 year ^{10}Be and 5730 year ^{14}C. These will give a base load activation which will mainly concern the extent to which spillage in occupied regions should be controlled through permitted air concentration limits.

The major producer of tritium is the D_2O of the moderator by thermal neutron capture. Production in the target, H_2O shield and shielding coolant is via high energy oxygen spallation reactions (e.g. the oxygen spallation contributes about 70% in the case of the D_2O target coolant).

The other major contributors to long lived activation are ^7Be, ^{10}Be and ^{14}C. These are mainly spallation products. Production in the moderator D_2O dominates because of the large volume.

18.6 Activation in Gas Systems

The major concerns are the air in the proton beam line for considerations of ventilation before entry into the tunnel and the helium and nitrogen in the innermost regions of SINQ.

18.6.1 Proton Beam Line Air Activation

The activation will come from thermal neutrons which are created by fast neutrons entering the tunnel and being thermalised. The fast neutrons come from backscattering by the target down the proton beam vacuum tube and interactions by protons lost on beam-line components.

The elemental compositions, cross-section information and the fraction of thermal neutron captures by each element are shown in the Table-VIII. The composition of air is taken from [135]. This information may then be used to calculate relative weights for the production of specific nuclides. ^{41}Ar and ^{14}C dominate. The activation calculation is completed by making an estimation for the thermal flux using the following approximations:-

1. Fast neutrons backscattered from the target.
2. Fast neutrons from proton loss (multiplicity is $\leq$ 5.5 for 590 MeV protons on iron).

3. The fast-neutron number albedo for concrete is 0.45 [72] giving a reflection factor of 0.82.

4. The thermal neutron albedo for concrete is 0.66 [72] giving a reflection factor of 2.9.

18.6.2 He and N_2 gas systems

These gas systems handle the filling for the 'containments' of the SINQ moderator tank. Activation levels are required for assessing the dose rates in the external plant room and consideration of handling and safety procedures. The activation is caused by a broad band neutron spectrum consisting of high-energy neutrons radiating from the target and fast, intermediate and thermal neutrons resulting from high-energy interactions in the iron of the shielding. The radiation field is quantified using the spectra calculated by Uwamino [60].

Direct activation of the helium will come from tritium produced by high-energy interactions - this has a threshold of about 22 MeV. The tritium production cross-section has been measured for neutron energies in the range 22 to 22.5MeV [136] and rises to about 40 mb. Measurement of tritium production from light nuclei (Li to Al) with 22 MeV protons [137], 450 MeV protons [138] and 2200 MeV protons [138, 139] give cross-sections of the order of 5 to 10% of the totaL The neutron measurement [136] corresponds to about 7% of the total cross-section.

The tritium production cross-section at high energies for ^4He is expected to be consistent with other light elements and is therefore taken to be 5 to 10% of the total inelastic interaction cross-section. For the spectrum in the irradiation region, the average energy is of the order of 100 MeV and the total inelastic cross-section of the order of 100 mb [140, 141]. The tritium production cross-section is therefore estimated to be 8 mb ±25%. The high-energy neutron intensity is 0.93/proton, giving a tritium production rate of 1.5.1010 /see/mA.

For nitrogen, high energy neutron cross-sections are estimated using HETC for an average neutron spectrum in shielding. Values are shown in Table-IX. The calculation gives a total interaction cross-section of 340 mb which is consistent with values measured for neighbouring elements [140] and the triton production is also based on the approximation that it corresponds to 10% of the total inelastic cross-section (see above).

Fast neutron cross-sections are taken from ENDF/B-IV [19] and energy averaged over the range 0.1 to 20 MeV with spectral weighting according to the results of Uwamino [60] and intermediate, epithermal and thermal neutron cross-sections from BNL-325 [141].

Only ^{13}N and ^{11}C give significant contributions to dose rates in the region of the pipework (these are both products of high-energy neutron spallation reactions). The decay along the length of the circuit is small (0.972 and 0.986 respectively) hence the dose at 1 m from a long length will be 0.11 $\mu Sv/h$. After beam switch-off, the dose will decay with 20% having a half-life of 20.38 m and 80% 9.96 m.

There will be production of some long half-life nuclides and also contributions by impurities. Impurities will come from outgassing of the tank walls and residuals in the system after cleaning. The quantities and components are unknown.

Table-VIII

Thermal Neutron Activation Data for Air.
(P = 1.013 bars, T = 288,2 K, density 1.225 kg/m^3)

Element	Nut. Den. /cc	σ_s barns	σ_{cap} barns	Σ_s cm^{-1}	Σ_{cap} cm^{-1}	Fraction of captures
N	3.98. 10^{19}	10.6	1.85	4.22 .10-4	7.36. 10-s	0.998
O	1.07.1019	3.76	0.00027	4.02010-5	2.890 10-e	3.9.10-5
Ar	2.38.1017	0.644	0.678	1.53 .10-7	1.61 · 10^{-7}	2.2 .10-3
C	8.05.1015	4.75	0.0034	3.82 · 10-s	2.74.10-11	3.7.10-7
Xe	2.22.1012	4.3	24.5	9.53,10-12	5.43.10-11	7.4,10-7
Kr	2.90.1013	7.5	25.0	2.18.10-10	7.26.10-10	9.8. 10-s
Ne	4.63.1014	2.42	0.038	1.12 .10-9	1.76 · 10^{-11}	2.4.10-7
He	1.33.1014	0.76	0.05	1.01.10-10	6.67 · 10^{-12}	9.0.10-8
H	2.29.1014	20.43	0.332	4.68 .10-8	7.61.10-11	1.0 .10-$
			Total	4,62010-4	7,37 .10-6	

Table-IX

Cross-sections (rob) for N^{nat} + Shield Neutron spectrum

	Mass 15	14	13	12	11	10	9	8	7	6	5	4	3
7N	0.15	41	22	0.43	0.075								
$_6C$	0.025	3.3	88	55	3.8	0.08							
$_5B$			0.1	5.0	23	76	1.1	0.15	0.18				
$_4Be$				0.43	0.18	0.78	5.6	3.0	0.35		0.15		
$_3Li$						0.025	0.025	0.9	0.15				
$_2He$								0.2	0.05	0.18	1.7	2.4	1.7

References

1 Proceedings of ICANS-III, Los-Alamos Scientific Lab. (1979)

2 Proceedings of ICANS-IV, KEK National Lab. 1980 KENS Report II (1981)

3 Proceedings of ICANS-V, KFA Jülich, 1981 Jül-Conf-45 (1981)

4 Proceedings of ICANS-VI, Argonne National Lab. 1982 ANL-82-80 (1982)

5 Proceedings of ICANS-VII, Chalk River Nuclear Lab. 1983 AECL 8488 (1984)

6 Proceedings of ICANS-VIII, Rutherford-Appleton Lab. 1985 RAL-85-11O (1985)

7 Proceedings of ICANS-IX, Swiss Inst. for Nuclear Research (1986)

8 Proceedings of ICANS-X, Los-Alamos National Laboratory, 1988 Institute of Physics Conference Series No. 97 (1989)

9 Proceedings of ICANS-XI, KEK National Lab. 1990 KEK Report 90-25 (1991)

10 G.S. Bauer (Editor) *Realisieungs Studie zur Spallations-Neutronenquelle* KfA June 1981

11 eg G.A. Bartholomew, J.C.D. Milton, E.W. Vogt AECL-2059 (1964)

12 RTNS facility, Lawrence Livermore National Laboratory No *Reference found.*

13 E.L. Kemp and A.L. Trego Proc. *8th* Symp. Eng. Problems of Fusion Research, Nov. 1979. IEEE Pub. 79CH1441-5NPS (1979)

14 W. Kley and G.R. Bishop EUR 9753 EN (1984)

15 K. Furukawa et al. 4^{th} Int. Conf. on Emerging Nuclear Energy Systems, Madrid (1986)

16 H. Takahashi et al. Invited Paper at 2^{nd} Int. Conf. on Emerging Nuclear Energy Systems, Lausanne (1980)

17 RSIC computer code collection No. CCC-178

18 R.R. Coveyou et al. Oak Ridge Report ORNL-3622 (1965)

19 D. Garber et al. BNL-NCS-50496 (1975)

20 M.J. Bell Oak Ridge Report ORNL-4628 (1973)

21 C.M. Lederer et al. 'Table of Isotopes" 7^{th} Ed. John Wiley & sons Inc. (New York) (1978)

22 U Reuss et al. GSI 72-9 (1972)

23 R.L. Ford and W.R. Nelson SLAC-21O (1978)

24 R. Serber Phys. Rev. 72, 1114 (1947)

25 H.W. Bertini Phys. Rev 188, 174 (1969)

26 S.J. Lindenbaum and R.M. Sternheimer Phys. Rev. 105, 1874 (1957)

27 R.M. Sternheimer and S.J. Lindenbaum Phys. Rev. 123, 333 (1961)

28 V.F. Weisskopf Phys. Rev. 52, 295 (1937)

29 L.W. Dresner Oak Ridge Report ORNL-TM-196 (1962)

30 F. Atchison Jül-Conf-34, paper II, 17 (1980)

31 W.A. Coleman and T.W. Armstrong Oak Ridge Report ORNL-4606 (1970)

32 K.C. Chandler and T. W. Armstrong Oak Ridge Report ORNL-4744 (1972)

33 R.R. Fullwood et al. Los-Alamos Report LA-4789 (1972)

34 Barkas and von Friesen Nuovo Cimento 29, 14 (1961)

35 J.W. Wachter, W.R. Burrus and W.A. Gibson Phys. Rev. 161, 971 (1973)

36 J. W. Wachter, W.A. Gibson and W.R. Burrus Phys. Rev. C6, 1496 (1972)

37 R. Madey and F.M. Waterman Phys. Rev. C8, 2412 (1973)

38 S.D. Howe Thesis, Kansas State University (1975)

39 D. Filges et al. KFA Report JüL-1960 (1984)

40 M.M. Meir et al. Nucl. Sci & Eng. 104, 339 (1990)

41 D. Filges Private Communication (1992)

42 G. Perring et al. Rutherford Lab. Report RAL-85-029 (1985)

43 A.D. Taylor Rutherford Lab. Report RAL-84-120 (1984)

44 F. Atchison Rutherford Lab. Report RAL-81-006 (1981)

45 T.A. Broome Private communication (1989)

46 G. Russel et al. Proc. ICANS-X (1988)

47 M. Pepin Proc. ICANS-VII (1983)

48 W.E. Fischer, L. Moritz, H. Spitzer and I.M. Thorson Nucl. Sci & Eng. 93, 273, (1986)

49 L.R. Veeser, R.R. Fullwood, A.A. Robba and E.R. Shunk Nucl. Inst & Meth. 117,509,(1974)

50 T.W. Armstrong et al. KFA Report JüL-1859 (1983)

51 J.S. Gilmore, G.J. Russell, H. Robinson and R.E. Prael Nucl. Sci & Eng. 99, 41 (1988)

52 D. Aylmer et al. KFA Report JüL-2130 (1987)

53 L.R. Veeser et al. NBS SP-425, 476 (1975)

54 W.B. Amian et al. ICANS IX (1986)

55 R.G. Alsmiller, T.W. Armstrong, W.A. Coleman Nucl. Sci & Eng. 42, 367 (1970)

56 B. Sigg ETH-IRT 10.8.82 (1982)

57 D.G. Doran Nucl. Sci. & Eng. 49, 130 (1972)

58 T.A. Gabriel, J.D. Amurgey, N.M. Greene Oak Ridge Report ORNL/TM-5160 (1976)

59 J. Lindhard et al. Mat-Fys Medd. 33, No. 10 (1963)

60 Y. Uwamino SINQ Project Internal Report SINQ/816/UY38-801 (1988)

61 V. Herrnberger, P. Stiller ICANS VII (1983)

62 R.G. Alsmiller & J. Barish Particle Accelerators 5, 155 (1973)

63 R.G. Alsmiller, R.T. Santoro & J. Barish Particle Accelerators '7, 1 (1975)

64 J. Duvoisin SIN Technical Memorandum TM-16-03 (1980)

65 D.I. Garber, R.R. Kinsey BNL-325 (3^{rd} Ed.) (1976)

66 Schmidt KfK-120 Data from 05 R/NMTC Master Cross-section Library

67 R.G. Alsmiller and J. Barish Oak Ridge Report ORNL-TM 7818

68 W.W. Engle Jr. Oak-Ridge report K-1693 (1967)

69 W.A. Rhoades et al. Oak Ridge Report ORNL/TM-6529 (1978)

70 F. Atchison and G. Heidenreich Proceeding of ICANS-XI (1991)

71 M.B. Emmett Oak Ridge Report ORNL-4972 (1975)

72 "Engineering Compendium on Radiation Shielding" Springer-Verlag Berlin (1968)

73 J.S. Fraser Paper 3, AECL-2177 (1965)

74 W.A. Coleman and R.G. Alsmiller, Jr. Nucl. Sci & Eng. 34, 104 (1968)

75 K. Chen et al. Phys. Rev. 166, 949 (1968)

76 K. Chen et al. Phys. Rev. 176, 1208 (1968)

77 K. Chen et al. Phys. Rev. C4, 2234 (1971)

78 W.S. Barashenkov et al. Nucl. Phys A187, 53 (1972)

79 D.W. Lang Nucl. Phys. 77, 545 (1966)

80 J. Gilat Phys. Rev. Cl, 1432 (1970)

81 J.R. Grover Phys. Rev. 157, 832 (1967)

82 J.R. Grover and J. Gilat Phys. Rev. 157, 802 (1967)

83 J.R. Grover and J. Gilat Phys. Rev. 157, 814 (1967)

84 J.R. Grover and J. Gilat Phys. Rev. 157, 823 (1967)

85 J.R. Grover and J. Gilat Phys. Rev. C3, 738 (1971)

86 See reference 5 in [14]

87 T.D. Thomas Phys. Rev. 116, 703 (1959)

88 G.M. Raisbeck and J.W. Cobble Phys. Rev. 153, 1270 (1967)

89 J.R. Huizenga et al. Phys. Rev. 126, 1270 (1967)

90 D.S. Burnett et al. Phys. Rev. 134, B952 (1964)

91 T. Sikkeland Phys. Rev. 135, B669 (1964)

92 T. Sikkeland et al. Phys. Rev. C3, 329 (1971)

93 L.J. Colby et al. Phys. Rev. 121, 1415 (1961)

94 R. Vandenbosch et al. Phys. Rev. 111, 1358 (1958)

95 J. Wing et al. Phys. Rev. 114, 163 (1959)

96 B.M. Foreman et al. Phys. Rev. 116, 382 (1959)

97 R.A. Glass et al. Phys. Rev. 104, 434 (1956)

98 G. Igo Phys. Rev. 115, 1665 (1959)

99 K-H Schmidt and W. Morawek Rep. Prog Phys 54, 949 (1991)

100 R. Vandenbosch and J.R. Huizenger Proc. of 2"* Int. Conf. on Peaceful Uses of Atomic Energy, Geneva, paper P/688, Vol 15, page 284 (1958)

101 M. Dahlinger et al. Nucl. Phys. A376, 94 (1982)

102 R. Vandenbosch and G.T. Seaborg Phys. Rev. 110, 507 (1958)

103 A. Chetham-Strode et al. Phys. Rev. 102, 747 (1956)

104 P.C. Stevenson et al. Phys. Rev. 111, 886 (1958)

105 M. Lindner and R.N. Osborne Phys. Rev. 103, 378 (1956)

106 H.M. Steiner and J.A. Jungerman Phys. Rev. 101, 807 (1956)

107 V.A. Kon'shin, E.S. Matusevich and V.I. Regushevskii Sov. J. Nucl. Phys. 2, 489 (1966)

108 L.G. Jodra and N. Sugarman Phys. Rev. 99, 1470 (1955)

109 P. Kruger and N. Sugarman Phys. Rev. 99, 1459 (1955)

110 (a) Y. Takeda and W.E. Fischer
(b) B. Sigg et al.
(c) M. Dubs and J. Ulrich
(d) G. Heidenreich
AU in Proceedings of ICANS-XI, KEK (1991)

111 G. Heidenreich SINQ Project Internal Report SINQ/821/HG11-901 (1991)

112 G.S. Bauer et al. Report 10 in Teil II, Annex A, Band 2 of reference 10 (1981)

113 P. Ageron et al. ILL Internal report DTe-80/237-PA/ngd (1980)

114 M.A. Lone et al. Atomic Data and Nuclear Data Tables, 26, 511 (1981)

115 S. Pearlstein Nucl. Sci and Eng 95, 116 (1987)

116 S. Cierjacks et al. ICANS-V (1981)

117 D. Filges et al. JüL-1960, (1984)

118 F. Atchison SINQ Project Internal Report SINQ/816/AFN-701 (1987)

119 I.A. Thorson and Moritz ICANS-IV, (1979)

120 T.A. Broome Paper VI in JüL-Conf-34, 95 (1980)

121 S. Ban and H. Hirayama ICANS-IV (1981)

122 F. Atchison SIN Technical Memorandum TM-37-19 (1982)

123 W. Schimmerling et al. Phys. Lett. 37B, 177 (1971)

124 T.A. Broome SNS project internal report SNS/TS/N1/81 (1981)

125 Y. Uwamino, T. Nakamura, K. Shin Nucl. Sci & Eng, 80, 360 (1982)

126 B. Boardman (Editor) Rutherford Lab. Report RL-82-006 (1982)

127 R.G. Fluharty et al IAEA-SM-170/45 (1973)

128 L.R. Veeser et al NBS SP-425, 476 (1975)

129 G. Russel et al. ICANS-IX (1986)

130 G.R. Stevenson and R.H. Thomas Health Physics 46, 115 (1984)

131 M. Barbier Induced Activation, North Holland (1969)

132 A. Janett SINQ Project Internal Report SINQ/814/JAD-803 (1988)

133 K.H. Beckurts and K. Wirtz "Neutron Physics" Springer-Verlag (1964)

134 Commission of the EEC Radiation Protection Report No. 43 (1988)

135 Handbook of Chemistry and Physics (63^{rd} Edition) CRC Press (1982)

136 R. E. Shamu & J. G. Jenkins Phys Rev B135, 99 (1964)

137 J. A. Gonzales-Vidal & W. H. Wade Phys Rev 120, 1354 (1960)

138 L. A. Currie, W. F. Libby & R. L. Wolfgang Phys Rev 101, 1557 (1956)

139 D. E. L. Fireman & F. S. Rowland Phys Rev 97, 780 (1955)

140 P. Schwaller et al. CERN 72-13 (1972)

141 S. F. Mughabghab & D. I. Garber BNL-325 (1973)